

EUROPEAN ORGANISATION FOR NUCLEAR RESEARCH (CERN)



Submitted to: JHEP



CERN-EP-2016-010
5th July 2016

Identification of high transverse momentum top quarks in pp collisions at $\sqrt{s} = 8$ TeV with the ATLAS detector

The ATLAS Collaboration

Abstract

This paper presents studies of the performance of several jet-substructure techniques, which are used to identify hadronically decaying top quarks with high transverse momentum contained in large-radius jets. The efficiency of identifying top quarks is measured using a sample of top-quark pairs and the rate of wrongly identifying jets from other quarks or gluons as top quarks is measured using multijet events collected with the ATLAS experiment in 20.3 fb^{-1} of 8 TeV proton–proton collisions at the Large Hadron Collider. Predictions from Monte Carlo simulations are found to provide an accurate description of the performance. The techniques are compared in terms of signal efficiency and background rejection using simulations, covering a larger range in jet transverse momenta than accessible in the dataset. Additionally, a novel technique is developed that is optimized to reconstruct top quarks in events with many jets.

© 2016 CERN for the benefit of the ATLAS Collaboration.

Reproduction of this article or parts of it is allowed as specified in the CC-BY-4.0 license.

arXiv:1603.03127v2 [hep-ex] 4 Jul 2016

Contents

1	Introduction	3
2	The ATLAS detector	4
3	Monte-Carlo simulation	4
4	Object reconstruction and event selection	6
4.1	Object reconstruction	6
4.2	Event selection	7
4.2.1	Signal sample	7
4.2.2	Background sample	10
5	Top-tagging techniques	11
5.1	Substructure-variable taggers	12
5.2	Shower Deconstruction	15
5.3	HEPTopTagger	24
6	Systematic uncertainties	27
6.1	Experimental uncertainties	27
6.2	In situ determination of the subjet energy scale for the HEPTopTagger	29
6.3	Uncertainties in the modelling of physics processes	30
7	Study of top-tagging performance using Monte-Carlo simulation	32
7.1	Comparison of top-tagging performance	32
7.2	HEPTopTagger04 performance	36
8	Measurement of the top-tagging efficiency and mistag rate	39
8.1	Top-tagging efficiency	39
8.1.1	Efficiency of the substructure-variable taggers	40
8.1.2	Efficiency of Shower Deconstruction	43
8.1.3	Efficiency of the HEPTopTagger	44
8.2	Mistag rate	47
8.2.1	Mistag rate for the substructure-variable taggers	48
8.2.2	Mistag rate for Shower Deconstruction	48
8.2.3	Mistag rate for the HEPTopTagger	48
9	Summary and conclusions	51
	Appendix	54
A	Additional distributions for the signal-sample selection	54

1. Introduction

Conventional top-quark identification methods reconstruct the products of a hadronic top-quark decay ($t \rightarrow bW \rightarrow bq'\bar{q}$) as jets with a small radius parameter R (typically $R = 0.4$ or 0.5).¹ There are usually several of these small- R jets in a high-energy, hard proton–proton (pp) collision event at the Large Hadron Collider (LHC). Hadronic top-quark decays are reconstructed by taking those jets which, when combined, best fit the kinematic properties of the top-quark decay, such as the top-quark mass and the W -boson mass. These kinematic constraints may also be fulfilled for a collection of jets which do not all originate from the same top-quark decay chain.

In analyses of LHC pp collisions, conventional top-quark identification methods are inefficient at high top-quark energies because the top-quark decay products are collimated and the probability of resolving separate small- R jets is reduced. Top quarks with high transverse momentum ($p_T \gtrsim 200$ GeV) may instead be reconstructed as a jet with large radius parameter, $R \geq 0.8$ (large- R jet) [1–13]. An analysis of the internal jet structure is then performed to identify and reconstruct hadronically decaying top quarks (top tagging).

Since a single jet that contains all of the decay products of a massive particle has different properties from a jet of the same transverse momentum originating from a light quark or gluon, it is possible to use the substructure of large- R jets to distinguish top quarks with high p_T from jets from other sources, for example from multijet production. These differences in the jet substructure can be better resolved after contributions from soft gluon radiation or from additional pp interactions in the same or adjacent bunch crossings (pile-up) are removed from the jets. Such methods are referred to as *jet grooming* and consist of either an adaptive modification of the jet algorithm or a selective removal of soft radiation during the process of iterative recombination in jet reconstruction [14–16].

The jet-substructure approach aims to reduce combinatorial background from assigning small- R jets to top-quark candidates in order to achieve a more precise reconstruction of the top-quark four-momentum and a higher background rejection. In searches for top–anti-top quark ($t\bar{t}$) resonances, the improved kinematic reconstruction leads to a better mass resolution for large resonance masses (≥ 1 TeV) compared to the conventional approach, resulting in an increased sensitivity to physics beyond the Standard Model (SM) [17].

ATLAS has published performance studies of jet-substructure methods for top tagging at a pp centre-of-mass energy of $\sqrt{s} = 7$ TeV [18]. In the paper presented here, the performance of several approaches to top tagging at $\sqrt{s} = 8$ TeV is documented. Top tagging based on the combination of jet-substructure variables, Shower Deconstruction [19, 20], and the HEPTopTagger [21, 22] is studied, as described in Section 5. A new method, HEPTopTagger04, is introduced. Optimised for top tagging in events with many jets, it uses a preselection of small- R jets as input to the HEPTopTagger algorithm.

Monte-Carlo (MC) simulation is used to compare the efficiencies and misidentification rates of all approaches over a large kinematic range. The performance of the different methods is studied in data using

¹ The ATLAS experiment uses a right-handed coordinate system with its origin at the nominal interaction point (IP) in the centre of the detector and the z -axis along the beam line. The x -axis points from the IP to the centre of the LHC ring, and the y -axis points upwards. Cylindrical coordinates (r, ϕ) are used in the transverse plane, ϕ being the azimuthal angle around the beam line. Observables labelled “transverse” are projected into the x – y plane. The pseudorapidity is defined in terms of the polar angle θ as $\eta = -\ln \tan \theta/2$. The transverse momentum is defined as $p_T = p \sin \theta = p/\cosh \eta$, and the transverse energy E_T has an analogous definition. The distance in η – ϕ space is referred to as $\Delta R = \sqrt{(\Delta\eta)^2 + (\Delta\phi)^2}$. The rapidity of a particle is defined as $y = \frac{1}{2} \ln \frac{E+p_z}{E-p_z}$, in which E and p_z are the energy and momentum z -component of the particle. The jet radius parameter R sets the range in y – ϕ space over which clustering to form jets occurs.

two different event samples: a signal sample enriched with top quarks and a background sample dominated by multijet production. The signal sample is used to measure top-tagging efficiencies from data, which are compared to the predictions obtained from MC simulations. Quantifying the degree to which MC simulations correctly model the top-tagging efficiency observed in data is crucial for any physics analysis in which top-tagging methods are used because MC simulations are commonly used to model signal and background processes. The signal sample is also used to determine the energy scale of subjects in situ from the reconstructed top-quark mass distribution. Top-tagging misidentification rates are measured in the background sample and are also compared to the prediction of MC simulations.

2. The ATLAS detector

The ATLAS detector consists of an inner tracking detector system (ID), which is surrounded by electromagnetic (EM) and hadronic calorimeters and a muon spectrometer (MS). The ID consists of silicon pixel and strip detectors and a transition-radiation tracker covering $|\eta| < 2.5$, and it is immersed in a 2 T axial magnetic field. The EM calorimeters use lead/liquid argon (LAr) technology to provide calorimetry for $|\eta| < 3.2$, with copper/LAr used in the forward region $3.1 < |\eta| < 4.9$. In the region $|\eta| < 1.7$, hadron calorimetry is provided by steel/scintillator calorimeters. In the forward region, copper/LAr and tungsten/LAr calorimeters are used for $1.5 < |\eta| < 3.2$ and $3.1 < |\eta| < 4.9$, respectively. The MS surrounds the calorimeter system and consists of multiple layers of trigger and tracking chambers within a toroidal magnetic field generated by air-core superconducting magnets, which allows for the measurement of muon momenta for $|\eta| < 2.7$. ATLAS uses a three-level trigger system [23] with a hardware-based first-level trigger, which is followed by two software-based trigger levels with an increasingly fine-grained selection of events at lower rates. A detailed description of the ATLAS detector is given in Ref. [24].

3. Monte-Carlo simulation

MC simulations are used to model different SM contributions to the signal and background samples. They are also used to study and compare the performance of top-tagging algorithms over a larger kinematic range than accessible in the data samples.

Top-quark pair production is simulated with POWHEG-BOX r2330.3 [25–28] interfaced with PYTHIA v6.426 [29] with the set of tuned parameters (tune) Perugia 2011C [30] and the CT10 [31] set of parton distribution functions (PDFs). The h_{damp} parameter, which effectively regulates the high- p_T gluon radiation in POWHEG, is left at the default value of $h_{\text{damp}} = \infty$. This MC sample is referred to as the POWHEG+PYTHIA $t\bar{t}$ sample. Alternative $t\bar{t}$ samples are used to evaluate systematic uncertainties. A sample generated with MC@NLO v4.01 [32, 33] interfaced to Herwig v6.520 [34] and JIMMY v4.31 [35] with the AUET2 tune [36], again simulated using the CT10 PDF set, is used to estimate the uncertainty related to the choice of generator. To evaluate the impact of variations in the parton shower and hadronization models, a sample is generated with POWHEG-BOX interfaced to Herwig and JIMMY. The effects of variations in the QCD (quantum chromodynamics) initial- and final-state radiation (ISR and FSR) modelling are estimated with samples generated with ACERMC v3.8 [37] interfaced to PYTHIA v6.426 with the AUET2B tune and the CTEQ6L1 PDF set [38], where the parton-shower parameters are varied in the range allowed by data [39]. For the study of systematic uncertainties on kinematic distributions

resulting from PDF uncertainties, a sample is generated using POWHEG-BOX interfaced with PYTHIA v.6.427 and using the HERAPDF set [40]. For all $t\bar{t}$ samples, a top-quark mass of 172.5 GeV is used.

The $t\bar{t}$ cross section for pp collisions at a centre-of-mass energy of $\sqrt{s} = 8$ TeV is $\sigma_{t\bar{t}} = 253^{+13}_{-15}$ pb for a top-quark mass of 172.5 GeV. It has been calculated at next-to-next-to-leading order (NNLO) in QCD including resummation of next-to-next-to-leading logarithmic (NNLL) soft gluon terms with $\text{top}++2.0$ [41–47]. The PDF and α_s uncertainties were calculated using the PDF4LHC prescription [48] with the MSTW2008 68% CL NNLO [49, 50], CT10 NNLO [31, 51] and NNPDF2.3 5f FFN [52] PDF sets, and their effect is added in quadrature to the effect of factorization- and renormalization-scale uncertainties. The NNLO+NNLL value is about 3% larger than the exact NNLO prediction, as implemented in Hather 1.5 [53].

In measurements of the differential $t\bar{t}$ production cross section as a function of the top-quark p_T , a discrepancy between data and MC predictions was observed in 7 TeV data [54]. Based on this measurement, a method of sequential reweighting of the top-quark- p_T and $t\bar{t}$ -system- p_T distributions was developed [55], which gives better agreement between the MC predictions and 8 TeV data. In this paper, this reweighting technique is applied to the POWHEG+PYTHIA $t\bar{t}$ sample, for which the technique was developed. The predicted total $t\bar{t}$ cross section at NNLO+NNLL is not changed by the reweighting procedure.

Single-top-quark production in the s - and Wt -channel is modelled with POWHEG-BOX and the CT10 PDF set interfaced to PYTHIA v6.426 using Perugia 2011C. Single-top-quark production in the t -channel is generated with POWHEG-BOX in the four-flavour scheme (in which b -quarks are generated in the hard scatter and the PDF does not contain b -quarks) using the four-flavour CT10 PDF set interfaced to PYTHIA v6.427. The overlap between Wt production and $t\bar{t}$ production is removed with the diagram-removal scheme [56] and the different single-top-production processes are normalized to the approximate NNLO cross-section predictions [57–59].

Events with a W or a Z boson produced in association with jets (W +jets or Z +jets) are generated with ALPGEN [60] interfaced to PYTHIA v6.426 using the CTEQ6L1 PDF set and Perugia 2011C. Up to five additional partons are included in the calculation of the matrix element, as well as additional c -quarks, $c\bar{c}$ -quark pairs, and $b\bar{b}$ -quark pairs, taking into account the masses of these heavy quarks. The W +jets contribution is normalized using the charge asymmetry in W -boson production in data [61, 62] by selecting μ +jets events and comparing to the prediction from MC simulations. The Z +jets contribution is normalized to the calculation of the inclusive cross section at NNLO in QCD obtained with FEWZ [63].

For the comparison of the different top-tagging techniques using MC simulation only, multijet samples are generated with PYTHIA v8.160 with the CT10 PDF set and AU2. As a source of high-transverse-momentum top quarks, samples of events with a hypothetical massive Z' resonance decaying to top-quark pairs, $Z' \rightarrow t\bar{t}$, are generated with resonance masses ranging from 400 GeV to 3000 GeV and a resonance width of 1.2% of the resonance mass [64] using PYTHIA v8.175 with the MSTW2008 68% CL LO PDF set [49, 50] and AU2.

For a study of top-quark reconstruction in a final state with many jets, the process² $pp \rightarrow H^+ \bar{t}(b) \rightarrow t\bar{b}\bar{t}(b)$ is generated in a type-II 2HDM model [65] with a mass of 1400 GeV of the charged Higgs boson using POWHEG-BOX interfaced to PYTHIA v8.165 with AU2 and the CT10 PDF set. The width of the charged Higgs boson is set to zero and the five-flavour scheme is used. The additional b -quark (in parentheses above) can be present or not, depending on whether the underlying process is $gg \rightarrow H^+ \bar{t}b$ or $g\bar{b} \rightarrow H^+ \bar{t}$.

² The process $pp \rightarrow H^- t(\bar{b}) \rightarrow \bar{t}b t(\bar{b})$ is also simulated. For simplicity only the positively charged Higgs boson is indicated explicitly in this paper, but it should be understood to denote both signs of the electric charge.

All MC samples are passed through a full simulation of the ATLAS detector [66] based on GEANT4 [67], except for the $t\bar{t}$ samples used to estimate systematic uncertainties due to the choice of MC generator, parton shower, and amount of ISR/FSR, which are passed through a faster detector simulation with reduced complexity in the description of the calorimeters [68]. All MC samples are reconstructed using the same algorithms as used for data and have minimum-bias events simulated with PYTHIA v8.1 [69] overlaid to match the pile-up conditions of the collision data sample.

4. Object reconstruction and event selection

4.1. Object reconstruction

Electron candidates are reconstructed [70, 71] from clusters in the EM calorimeter and are required to have a track in the ID, associated with the main primary vertex [72], which is defined as the one with the largest $\sum p_{T,\text{track}}^2$. They must have $E_T > 25$ GeV and $|\eta_{\text{cluster}}| < 2.47$ excluding the barrel/end-cap-calorimeter transition region $1.37 < |\eta_{\text{cluster}}| < 1.52$, where η_{cluster} is the pseudorapidity of the cluster in the EM calorimeter. The shape of the cluster in the calorimeter must be consistent with the typical energy deposition of an electron and the electron candidate must satisfy the *mini-isolation* [17, 73] requirement to reduce background contributions from non-prompt electrons and hadronic showers: the scalar sum of track transverse momenta within a cone of size $\Delta R = 10 \text{ GeV}/E_T^{\text{el}}$ around the electron track must be less than 5% of the electron transverse energy E_T^{el} (only tracks with $p_T > 1$ GeV are considered in the sum, excluding the track matched to the electron cluster).

Muons are reconstructed [74] using both the ID and the MS and must be associated with the main primary vertex of the event. Muons are required to have $p_T > 25$ GeV and $|\eta| < 2.5$ and are required to be isolated with requirements similar to those used for electron candidates: the scalar sum of the track transverse momenta within a cone of size $\Delta R = 10 \text{ GeV}/p_T^\mu$ around the muon track must be less than 5% of p_T^μ , where p_T^μ is the transverse momentum of the muon.

Jets are built [75] from topological clusters of calorimeter cells, which are calibrated to the hadronic energy scale [76] using a local cell-weighting scheme [77]. The clusters are treated as massless and are combined by adding their four-momenta, leading to massive jets. The reconstructed jet energy is calibrated using energy- and η -dependent corrections obtained from MC simulations. These corrections are obtained by comparing reconstructed jets with geometrically matched jets built from stable particles (particle level). The corrections are validated using in situ measurements of small- R jets [78].

Jets reconstructed with the anti- k_t [79] algorithm using a radius parameter $R = 0.4$ must satisfy $p_T > 25$ GeV and $|\eta| < 2.5$. The jet vertex fraction (JVF) uses the tracks matched to a jet and is defined as the ratio of the scalar sum of the transverse momenta of tracks from the main primary vertex to that of all matched tracks. A jet without any matched track is assigned a JVF value of -1 . For anti- k_t $R = 0.4$ jets with $p_T < 50$ GeV and $|\eta| < 2.4$, the JVF must be larger than 0.5 [80] to suppress jets from pile-up.

Large- R jets are reconstructed with the anti- k_t algorithm using $R = 1.0$ and with the Cambridge/Aachen algorithm [81] (C/A) using $R = 1.5$. Anti- k_t $R = 1.0$ jets are groomed using a trimming procedure [16]: the constituents of the anti- k_t $R = 1.0$ jet are reclustered using the k_t algorithm [82] with $R = 0.3$. Subjects with a p_T of less than 5% of the large- R jet p_T are removed [18]. The properties of the trimmed jet are recalculated from the constituents of the remaining subjects. The trimmed jet mass, p_T , and pseudorapidity

are corrected to be, on average, equal to the particle-level jet mass, p_T , and pseudorapidity using MC simulations [18, 83]. An illustration of trimming is given in Figure 4 of Ref. [18].

The C/A $R = 1.5$ jets are required to satisfy $p_T > 200$ GeV. These jets are used as input to the HEPTopTagger, which employs an internal pile-up suppression, and are therefore left ungroomed. For trimmed anti- k_r $R = 1.0$ jets, the minimum p_T is raised to 350 GeV to reduce the fraction of jets not containing all top-quark decay products due to the smaller jet radius parameter. All large- R jets must satisfy $|\eta| < 2.0$.

The missing transverse momentum is calculated from the vector sum of the transverse energy of clusters in the calorimeters, and it is corrected for identified electrons, muons and anti- k_r $R = 0.4$ jets, for which specific object-identification criteria are applied [84]. The magnitude of the missing transverse momentum is denoted by E_T^{miss} .

4.2. Event selection

The data used in this paper were taken in 2012 at a centre-of-mass-energy $\sqrt{s} = 8$ TeV and correspond to an integrated luminosity of 20.3 fb^{-1} [85]. Data are used only if all subsystems of the detector as well as the trigger system were fully functional. Baseline quality criteria are imposed to reject contamination from detector noise, non-collision beam backgrounds, and other spurious effects. Events are required to have at least one reconstructed primary vertex with at least five associated ID tracks, each with a p_T larger than 400 MeV. This vertex must be consistent with the LHC beam spot [72]. In addition, all anti- k_r $R = 0.4$ jets in the event which have $p_T > 20$ GeV are required to satisfy the “looser” quality criteria discussed in detail in Ref. [78], otherwise the event is rejected.

Two different event samples are used to study the performance of top-tagging algorithms in data: a signal sample enriched in hadronically decaying top quarks and a background sample consisting mainly of multijet events.

4.2.1. Signal sample

For the signal sample, a selection of $t\bar{t}$ events in the lepton+jets channel is used, in which one of the W bosons from $t\bar{t} \rightarrow W^+ b W^- \bar{b}$ decays hadronically and the other W boson decays leptonically. The selection is performed in the muon channel and the electron channel.

The selection criteria for the muon and electron channels differ only in the requirements imposed on the reconstructed leptons. For the muon channel, the events are required to pass at least one of two muon triggers, where one is optimized to select isolated muons with a transverse momentum of at least 24 GeV and the other selects muons with at least 36 GeV without the isolation requirement. Exactly one muon with $p_T > 25$ GeV is required as defined in Section 4.1. Muons are rejected if they are close to an anti- k_r $R = 0.4$ jet that has $p_T > 25$ GeV. The rejection occurs if $\Delta R(\mu, \text{jet}) < (0.04 + 10 \text{ GeV}/p_T^\mu)$. Events in the muon channel are rejected if they contain an additional electron candidate.

For the electron channel, events are required to pass at least one of two triggers. The first is designed for isolated electrons with $p_T > 24$ GeV and the second trigger requires electrons with $p_T > 60$ GeV without the isolation requirement. Exactly one electron is required with $E_T > 25$ GeV as defined in Section 4.1. An electron-jet overlap removal is applied based on the observation that the electron p_T contributes a significant fraction of the p_T of close-by anti- k_r $R = 0.4$ jets. Therefore, the electron momentum is

subtracted from the jet momentum before kinematic requirements are applied to the jet, so that jets close to an electron often fall below the jet p_T threshold. If the electron-subtracted jet still fulfils the kinematic requirements for anti- k_t $R = 0.4$ jets and the electron is still close, the electron is considered not isolated. In this case, the electron is removed from the event and the original non-subtracted jet is kept. Events in the electron channel are rejected if they also contain a muon candidate.

To select events with a leptonically decaying W boson, the following requirements are imposed. The events are required to have missing transverse momentum $E_T^{\text{miss}} > 20$ GeV. Additionally, the scalar sum of E_T^{miss} and the transverse mass of the leptonic W -boson candidate must satisfy $E_T^{\text{miss}} + m_T^W > 60$ GeV, where $m_T^W = \sqrt{2p_T^\ell E_T^{\text{miss}}(1 - \cos \Delta\phi)}$ is calculated from the transverse momentum of the lepton, p_T^ℓ , and E_T^{miss} in the event. The variable $\Delta\phi$ is the azimuthal angle between the lepton momentum and the E_T^{miss} direction.

To reduce contamination from W +jets events, each event must contain at least two b -tagged anti- k_t $R = 0.4$ jets with $p_T > 25$ GeV and $|\eta| < 2.5$. A neural-network-based b -tagging algorithm [86] is employed, which uses information on the impact parameters of the tracks associated with the jet, the secondary vertex, and the decay topology as its input. The operating point chosen for this analysis corresponds to a b -tagging identification efficiency of 70% in simulated $t\bar{t}$ events. In $t\bar{t}$ events with high-momentum top quarks, the direction of the b -quark from the leptonic decay of a top quark is often close to the lepton direction. Hence, at least one b -tagged jet is required to be within $\Delta R = 1.5$ of the lepton direction. A second b -tag away from the lepton is required that fulfils $\Delta R(\text{lepton}, b\text{-tag}) > 1.5$. This b -tagged jet is expected to originate from the b -quark from the hadronic top-quark decay, and is expected to be well separated from the decay products of the leptonically decaying top quark.

Each event is required to contain at least one large- R jet that fulfils the requirement $\Delta R(\text{lepton}, \text{large-}R \text{ jet}) > 1.5$. This criterion increases the probability that the large- R jet originates from a hadronically decaying top quark. The large- R jet has to fulfil $|\eta| < 2$ and exceed a p_T threshold. The jet algorithm, the radius parameter, and the p_T threshold depend on the top tagger under study. An overview is given in Table 1. The top taggers are introduced in Section 5 where also the choice of particular large- R jet types is motivated. If several large- R jets in an event satisfy the mentioned criteria, only the jet with the highest p_T is considered. This choice does not bias the measurements presented in this paper, because the top-tagging efficiencies and misidentification rates are measured as a function of the large- R jet kinematics.

In simulated events containing top quarks, large- R jets are classified as *matched* or *not matched* to a hadronically decaying top quark. The classification is based on the distance ΔR between the axis of the large- R jet and the flight direction of a generated hadronically decaying top quark. The top-quark flight direction at the top-quark decay vertex is chosen, so as to take into account radiation from the top quark changing its direction. Matched jets are those with ΔR smaller than a predefined value R_{match} , while not-matched jets are those with $\Delta R > R_{\text{match}}$. The radius R_{match} is 0.75 for the anti- k_t $R = 1.0$ jets and 1.0 for

Tagger	Jet algorithm	Grooming	Radius parameter	p_T range	$ \eta $ range
Tagger I–V W' top tagger Shower Deconstruction	anti- k_t	trimming ($R_{\text{sub}} = 0.3$, $f_{\text{cut}} = 0.05$)	$R = 1.0$	> 350 GeV	< 2
HEPTopTagger	C/A	none	$R = 1.5$	> 200 GeV	< 2

Table 1: Definitions of large- R jets and their p_T thresholds used as input to the different top taggers.

the $C/A R = 1.5$ jets. Changing R_{match} to 1.0 for the anti- $k_t R = 1.0$ jets has a negligible impact on the size of the not-matched $t\bar{t}$ contribution (less than 1%). Alternative matching schemes were tested but did not show improved matching properties, such as a higher matching efficiency.

Distributions for the signal selection with at least one trimmed anti- $k_t R = 1.0$ jet with $p_T > 350$ GeV are shown in Figure 1. The top-quark purity in this sample is 97%, with a small background contribution from W +jets production (3%). Single-top production accounts for 4% of the event yield and the $t\bar{t}$ prediction accounts for 93% (62% from matched and 31% from not-matched events). Not-matched $t\bar{t}$ events are an intrinsic feature of the signal selection. With different selection criteria the fraction of not-matched $t\bar{t}$ events varies, as does the total number of selected events. The chosen signal selection in the lepton+jets channel was found to be a good compromise between a reduced fraction of not-matched $t\bar{t}$ events and a sizeable number of selected events.

The mass and the transverse momentum of the highest- p_T trimmed anti- $k_t R = 1.0$ jet are shown in Figures 1(a) and 1(b), respectively. The systematic uncertainties shown in these plots are described in detail in Section 6. The mass distribution shows three peaks: one at the top-quark mass, a second at the W -boson mass and a third around 35 GeV. According to simulation, which describes the measured distribution within uncertainties, the top-quark purity in the region near the top-quark mass is very high, with the largest contribution being matched $t\bar{t}$. The peak at the position of the W -boson mass originates from hadronically decaying top quarks where the b -jet from the decay is not contained in the large- R jet. Even smaller masses are obtained if one of the decay products of the hadronically decaying W boson is not contained in the large- R jet or if only one top-quark-decay product is captured in the large- R jet. In these cases, a small mass is obtained due to the kinematic requirements imposed during trimming. The fraction of not-matched $t\bar{t}$ increases for decreasing large- R jet mass indicating a decreasing fraction of jets with a close-by hadronically decaying top quark. Only a small fraction of the peak at small mass is due to matched $t\bar{t}$. The large- R jet p_T exhibits a falling spectrum, and the application of the sequential p_T reweighting to the simulation (cf. Section 3) yields a good description of the data.

The dominant systematic uncertainties in Figure 1 result from uncertainties in the large- R jet energy scale (JES), the PDF, and the $t\bar{t}$ generator. The contributions from these sources are approximately equal in size, except for large- R jets with $p_T > 500$ GeV where the choice of $t\bar{t}$ generator dominates. These uncertainties affect mostly the normalization of the distributions. For the PDF and $t\bar{t}$ generator uncertainties, this normalization uncertainty comes about as follows: while the total $t\bar{t}$ cross section is fixed when the different MC event samples are compared, the p_T dependence of the cross section varies from sample to sample, leading to a change in normalization for the phase space considered here ($p_T > 350$ GeV).

Distributions for events fulfilling the signal selection with at least one $C/A R = 1.5$ jet with $p_T > 200$ GeV, to be used in the HEPTopTagger studies, are shown in Figure 2. According to the simulation, the top quark purity in this sample is 97%. The only non-negligible background process is W +jets production (3%). The $t\bar{t}$ prediction is split into a matched part (59%) and a not-matched part (29%). Single-top production contributes 9% to the total event yield. The mass of the highest- p_T $C/A R = 1.5$ jet with $p_T > 200$ GeV is shown in Figure 2(a) and it exhibits a broad peak around 190 GeV. The large- R -jet mass distributions from not-matched $t\bar{t}$, single-top production, and W +jets production have their maxima at smaller values than the distribution from matched $t\bar{t}$. No distinct W -boson peak is visible, because the $C/A R = 1.5$ jets are ungroomed. The p_T spectrum of the highest- p_T $C/A R = 1.5$ jet is smoothly falling and well described by simulation after the sequential p_T reweighting is applied (Figure 2(b)).

The $C/A R = 1.5$ jet distributions are described by the simulation within the uncertainties. The systematic uncertainties are slightly smaller than those in the distributions shown in Figure 1 for anti- $k_t R = 1.0$ jets

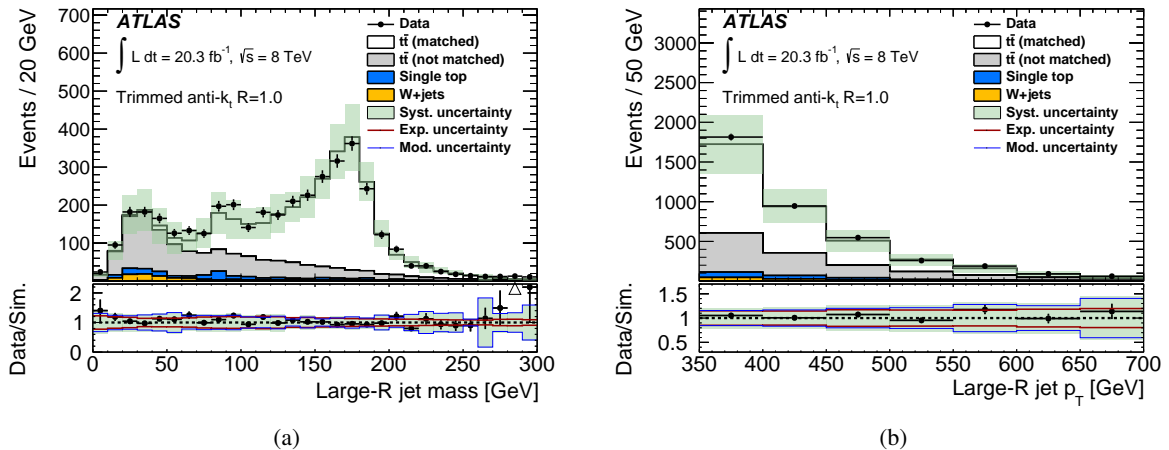


Figure 1: Detector-level distributions of variables reconstructed in events passing the signal-sample selection ($t\bar{t}$) with at least one trimmed anti- k_t $R = 1.0$ jet with $p_T > 350$ GeV. Shown in (a) is the mass and in (b) the transverse momentum of the highest- p_T anti- k_t $R = 1.0$ jet. The vertical error bar indicates the statistical uncertainty of the measurement. Also shown are distributions for simulated SM contributions with systematic uncertainties (described in Section 6) indicated as a band. The $t\bar{t}$ prediction is split into a *matched* part for which the large- R jet axis is within $\Delta R = 0.75$ of the flight direction of a hadronically decaying top quark and a *not matched* part for which this criterion does not hold. The ratio of measurement to prediction is shown at the bottom of each subfigure and the error bar and band give the statistical and systematic uncertainties of the ratio, respectively. The impacts of experimental and $t\bar{t}$ modelling uncertainties are shown separately for the ratio.

with $p_T > 350$ GeV because the $t\bar{t}$ modelling uncertainties increase with large- R jet p_T . The uncertainties in the large- R JES, the b -tagging efficiency, the prediction of the $t\bar{t}$ cross section, and $t\bar{t}$ modelling uncertainties from the choice of generator, parton shower, and PDF set all contribute to the systematic uncertainty in the large- R -jet mass distribution. The uncertainty from the choice of generator increases in the high-mass tail, which is particularly sensitive to additional radiation close to the hadronically decaying top quark. The modelling uncertainties for the large- R -jet p_T distribution increase with p_T due to increasing uncertainties from the large- R JES, the b -tagging efficiency, and the $t\bar{t}$ modelling uncertainties. The increase of the $t\bar{t}$ modelling uncertainty with large- R -jet p_T is an observation consistent with Figure 1(b).

Distributions of other kinematic variables are also well described by the simulation and are shown in Appendix A.

4.2.2. Background sample

Due to the high threshold of the unprescaled jet triggers, such triggers do not provide an unbiased background sample of large- R jets from multijet production. Therefore, the misidentification rate is measured in a multijet sample collected with single-electron triggers, where the event is triggered by an object which in the detailed offline analysis fails the electron-identification requirements.

For the electron candidate used at the trigger level, the requirements on the pseudorapidity of the cluster of calorimeter cells are the same as for reconstructed electrons (cf. Section 4.1). Events with an offline reconstructed electron satisfying loose identification requirements [71] (these loose identification

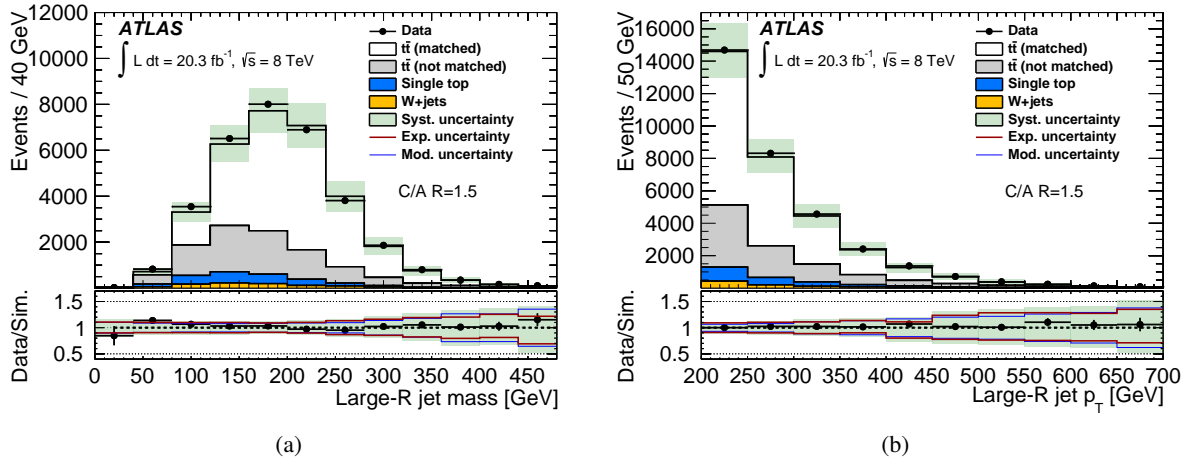


Figure 2: Detector-level distributions of (a) the mass and (b) the transverse momentum of the highest- p_T $C/A R = 1.5$ jet in events passing the signal-sample selection ($t\bar{t}$) with at least one $C/A R = 1.5$ jet with $p_T > 200$ GeV. The vertical error bar indicates the statistical uncertainty of the measurement. Also shown are distributions for simulated SM contributions with systematic uncertainties (described in Section 6) indicated as a band. The $t\bar{t}$ prediction is split into a *matched* part for which the large- R jet axis is within $\Delta R = 1.0$ of the flight direction of a hadronically decaying top quark and a *not matched* part for which this criterion does not hold. The ratio of measurement to prediction is shown at the bottom of each subfigure and the error bar and band give the statistical and systematic uncertainties of the ratio, respectively. The impacts of experimental and $t\bar{t}$ modelling uncertainties are shown separately for the ratio.

requirements do not include isolation criteria) are rejected to reduce contributions from electroweak processes. Only large- R jets well separated from the electron-trigger candidate are studied. This selection provides a sample that is largely dominated by multijet production, for which the electron-trigger candidate is a jet misidentified as an electron. Events are required to be selected by the trigger for electrons with $p_T > 60$ GeV and not by the trigger for isolated electrons with a threshold of 24 GeV (described in Section 4.2.1). Not using the isolated electron trigger reduces top-quark contamination in the selected jet sample. The fraction of $t\bar{t}$ events before requiring a tagged top candidate is negligible. After requiring a tagged top candidate, the $t\bar{t}$ events are subtracted for the top taggers for which they present a non-negligible part of the sample, as detailed in Section 8.2.

At least one large- R jet is required with a jet axis separated from the electron-trigger object by $\Delta R > 1.5$. The algorithm, radius parameter, and p_T threshold of the jet depend on the particular top-tagging algorithm under study (see Table 1). If several large- R jets satisfying these criteria are found, only the jet with the highest p_T is considered for the study of the misidentification rate. This choice does not bias the measurements, because the misidentification rate is measured as a function of the large- R -jet p_T .

5. Top-tagging techniques

Top tagging classifies a given large- R jet as a top jet if its substructure satisfies certain criteria. This paper examines several top-tagging methods, which differ in their substructure analysis and which are described in the following subsections.

Due to the different substructure criteria applied, the methods have different efficiencies for tagging signal jets and different misidentification rates for background jets. High efficiency is obtained for loose criteria and implies a high misidentification rate. The performance of the taggers in terms of efficiencies and misidentification rates is provided in Section 7.1.

5.1. Substructure-variable taggers

The choice of trimmed anti- k_t $R = 1.0$ jets (as defined in Section 4.1) for substructure-based analyses has been previously studied in detail [18], including comparisons of different grooming techniques and parameters. The following jet-substructure variables are used for top tagging in this analysis:

- *trimmed mass* - The mass, m , of the trimmed anti- k_t $R = 1.0$ jets is less susceptible to energy depositions from pile-up and the underlying event than the mass of the untrimmed jet. On average, large- R jets containing top-quark decay products have a larger mass than background jets.
- *k_t splitting scales* - The k_t splitting scales [87] are a measure of the scale of the last recombination steps in the k_t algorithm, which clusters high-momentum and large-angle proto-jets last. Hence, the k_t splitting scales are sensitive to whether the last recombination steps correspond to the merging of the decay products of massive particles. They are determined by reclustering the constituents of the trimmed large- R jet with the k_t algorithm and are defined as

$$\sqrt{d_{ij}} = \min(p_{Ti}, p_{Tj}) \times \Delta R_{ij} \quad , \quad (1)$$

in which ΔR_{ij} is the distance between two subjets i and j in η - ϕ space, and p_{Ti} and p_{Tj} are the corresponding subjet transverse momenta. Subjets merged in the last k_t clustering step provide the $\sqrt{d_{12}}$ observable, and $\sqrt{d_{23}}$ is the splitting scale of the second-to-last merging. The expected value of the first splitting scale $\sqrt{d_{12}}$ for hadronic top-quark decays captured fully in a large- R jet is approximately $m_t/2$, where m_t is the top quark mass. The second splitting scale $\sqrt{d_{23}}$ targets the hadronic decay of the W boson with an expected value of approximately $m_W/2$. The use of the splitting scale for W -boson tagging in 8 TeV ATLAS data is explored in Ref. [88]. Background jets initiated by hard gluons or light quarks tend to have smaller values of the splitting scales and exhibit a steeply falling spectrum.

- *N -subjettiness* - The N -subjettiness variables τ_N [89, 90] quantify how well jets can be described as containing N or fewer subjets. The N subjets found by an exclusive k_t clustering of the constituents of the trimmed large- R jet define axes within the jet. The quantity τ_N is given by the p_T -weighted sum of the distances of the constituents from the subjet axes:

$$\tau_N = \frac{1}{d_0} \sum_k p_{Tk} \times \Delta R_k^{\min} \quad \text{with} \quad d_0 \equiv \sum_k p_{Tk} \times R \quad , \quad (2)$$

in which p_{Tk} is the transverse momentum of constituent k , ΔR_k^{\min} is the distance between constituent k and the axis of the closest subjet, and R is the radius parameter of the large- R jet. The ratio τ_3/τ_2 (denoted τ_{32}) provides discrimination between large- R jets formed from hadronically decaying top quarks with high transverse momentum (top jets) which have a 3-prong subjet structure (small values of τ_{32}) and non-top jets with two or fewer subjets (large values of τ_{32}). Similarly, the ratio $\tau_2/\tau_1 \equiv \tau_{21}$ is used to separate large- R jets with a 2-prong structure (hadronic decays of Z or W bosons) from jets with only one hard subjet, such as those produced from light quarks or gluons.

The variable τ_{21} is studied in the context of W -boson tagging with the ATLAS and CMS detectors in Ref. [88] and Ref. [91], respectively. A method that distinguishes hadronically decaying high- p_T Z bosons from W bosons is studied in Ref. [92].

Distributions of the k_t splitting scales and N -subjettiness variables for large- R jets in a top-quark-enriched event sample (cf. Section 4.2.1) are shown in Figure 3. The $\sqrt{d_{12}}$ distribution shows a broad shoulder at values above 40 GeV and the matched $t\bar{t}$ contribution exhibits a peak near $m_t/2$ as expected. For the not-matched $t\bar{t}$ contribution and the W +jets process, $\sqrt{d_{12}}$ takes on smaller values and the requirement of a minimum value of $\sqrt{d_{12}}$ can be used to increase the ratio of top-quark signal to background (S/B). For the second splitting scale $\sqrt{d_{23}}$, signal and background are less well separated than for $\sqrt{d_{12}}$, but $\sqrt{d_{23}}$ also provides signal-background discrimination. The distribution of τ_{32} shows the expected behaviour, with the matched $t\bar{t}$ contribution having small values, because the hadronic top-quark decay is better described by a three-subjet structure than by two subjects. For not-matched $t\bar{t}$ and W +jets production, the distribution peaks at ≈ 0.75 . Requiring a maximum value of τ_{32} increases the signal-to-background ratio. For τ_{21} , the separation of signal and background is less pronounced, but values above 0.8 are obtained primarily for background. Thus, τ_{21} also provides signal-background discrimination.

The distributions are well described by the simulation of SM processes within systematic uncertainties, which are described in Section 6. For all distributions shown, the large- R JES, $t\bar{t}$ generator, and parton-shower uncertainties give sizeable contributions, as do the uncertainties of the modelling of the respective substructure variables shown. The uncertainties for $\sqrt{d_{12}}$ and $\sqrt{d_{23}}$ are dominated by the $t\bar{t}$ generator and ISR/FSR uncertainties, respectively, for low values of the substructure variable. Low values of these variables are mainly present for not-matched $t\bar{t}$, for which the modelling is particularly sensitive to the amount of high- p_T radiation in addition to $t\bar{t}$, because these large- R jets do not primarily originate from hadronically decaying top quarks. The modelling of additional radiation in $t\bar{t}$ events is also an important uncertainty for the number of events at low values of τ_{32} and τ_{21} , for which the $t\bar{t}$ ISR/FSR uncertainties dominate the total uncertainty. The modelling of the substructure variables themselves dominates for high values of $\sqrt{d_{12}}$, $\sqrt{d_{23}}$, τ_{32} , and τ_{21} .

Different top taggers, based on these substructure variables, are defined (Table 2). A large- R jet is tagged as a top jet by the corresponding tagger if the top-tagging criteria are fulfilled. Substructure tagger III was optimized for a search for $t\bar{t}$ resonances in the single-lepton channel [17]. Compared to other taggers, it has a rather high efficiency and misidentification rate because the analysis required only little background rejection, as the background was already much reduced by a lepton requirement. Removing the mass requirement or the requirement on $\sqrt{d_{12}}$ further increases the efficiency (taggers I and II). The W' top tagger was optimized for a search for tb resonances (W') in the fully-hadronic decay mode [2], where a high background suppression is required. The efficiency of this tagger is therefore lower than that of taggers I to III. Taggers IV and V are introduced to study the effect of a requirement on $\sqrt{d_{23}}$ in addition to the requirements of tagger III.

Distributions of the p_T and mass of trimmed anti- k_t $R = 1.0$ jets after applying the six different taggers based on substructure variables are shown in Figures 4 and 5, respectively, for events passing the full signal selection of Section 4.2.1. While the p_T spectra look similar after tagging by the different taggers, the mass spectra differ significantly due to the different substructure-variable requirements imposed by the taggers. Taggers II to V require the mass to be greater than 100 GeV, and this cut-off is visible in the distributions. The mass distribution after the $\sqrt{d_{12}} > 40$ GeV requirement of Tagger I (Figure 5(a)) differs from that of the pre-tag distribution (Figure 1(a)), because $\sqrt{d_{12}}$ is strongly correlated with the trimmed mass. The impact of the $\sqrt{d_{12}} > 40$ GeV requirement plus the N -subjettiness requirements of

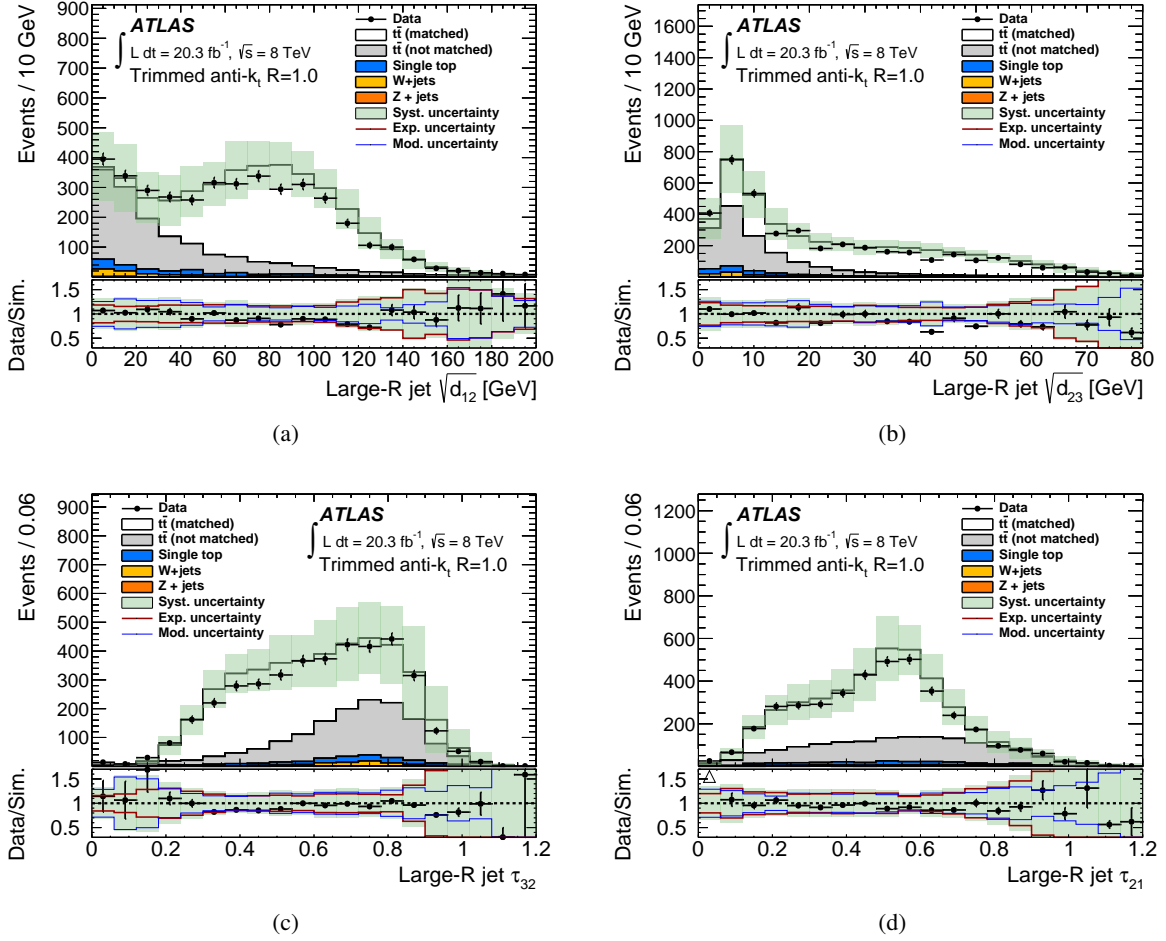


Figure 3: Detector-level distribution of substructure variables of the highest- p_T trimmed anti- k_t $R = 1.0$ jet with $p_T > 350$ GeV in events passing the signal selection. The splitting scales (a) $\sqrt{d_{12}}$ and (b) $\sqrt{d_{23}}$ and the N -subjettiness ratios (c) τ_{32} and (d) τ_{21} are shown. The vertical error bar indicates the statistical uncertainty of the measurement. Also shown are distributions for simulated SM contributions with systematic uncertainties (described in Section 6) indicated as a band. The $t\bar{t}$ prediction is split into a *matched* part for which the large- R jet axis is within $\Delta R = 0.75$ of the flight direction of a hadronically decaying top quark and a *not matched* part for which this criterion does not hold. The ratio of measurement to prediction is shown at the bottom of each subfigure and the error bar and band give the statistical and systematic uncertainties of the ratio, respectively. The impacts of experimental and $t\bar{t}$ modelling uncertainties are shown separately for the ratio.

Tagger	Top-tagging criterion
Substructure tagger I	$\sqrt{d_{12}} > 40$ GeV
Substructure tagger II	$m > 100$ GeV
Substructure tagger III	$m > 100$ GeV and $\sqrt{d_{12}} > 40$ GeV
Substructure tagger IV	$m > 100$ GeV and $\sqrt{d_{12}} > 40$ GeV and $\sqrt{d_{23}} > 10$ GeV
Substructure tagger V	$m > 100$ GeV and $\sqrt{d_{12}} > 40$ GeV and $\sqrt{d_{23}} > 20$ GeV
W' top tagger	$\sqrt{d_{12}} > 40$ GeV and $0.4 < \tau_{21} < 0.9$ and $\tau_{32} < 0.65$

Table 2: Top taggers based on substructure variables of trimmed anti- k_t $R = 1.0$ jets.

the W' top tagger on the mass spectrum is visible by comparing Figure 5(f) with the pre-tag distribution (Figure 1(a)). The prominent peak around the top-quark mass shows that the sample after tagging is pure in jets which contain all three decay products of the hadronic top-quark decay.

All distributions are described by the MC simulation within uncertainties, indicating that the kinematics and the substructure of tagged large- R jets are well modelled by simulation. The uncertainty in the large- R jet p_T requiring a top tag is dominated by the large- R JES and the parton-shower and $t\bar{t}$ generator uncertainties. Hence, the same uncertainties dominate in the different regions of the p_T spectrum as before requiring a top tag (Section 4.2.1). The uncertainty on the large- R -jet mass distributions is dominated by the jet-mass scale uncertainty for all substructure taggers. The large- R JES as well as $t\bar{t}$ modelling uncertainties also contribute, but have a smaller impact. For all substructure taggers, the uncertainties in the substructure variables used in the respective taggers have a non-negligible impact, in particular for low large- R jet masses, i.e. in the regime which is sensitive to the modelling of not-matched $t\bar{t}$ and extra radiation.

5.2. Shower Deconstruction

In *Shower Deconstruction* (SD) [19, 20], likelihoods are separately calculated for the scenario that a given large- R jet originates from a hadronic top-quark decay and for the scenario that it originates from a background process. The likelihoods are calculated from theoretical hypotheses, which for the application in this paper correspond to the SM. The signal process is the hadronic decay of a top quark and for the background process, the splitting of hard gluons into $q\bar{q}$ is considered. For signal and background, the effect of the parton shower is included in the calculation of the likelihood. Subjects of the large- R jet are used as proxies for partons in the underlying model and a weight is calculated for each possible shower that leads to the observed subjet configuration. This weight is proportional to the probability that the assumed initial particle generates the final configuration, taking into account the SM amplitude for the underlying hard process and the Sudakov form factors for the parton shower. A discriminating variable χ is calculated as the ratio of the sum of the signal-hypothesis weights to the sum of the background-hypothesis weights. For a set $\{p_i^k\}$ of N observed subjet four-momenta p_i^k , in which $i \in [1, N]$, the value of χ is given by

$$\chi(\{p_i^k\}) = \frac{\sum_{\text{perm.}} \text{P}(\{p_i^k\}|\text{signal})}{\sum_{\text{perm.}} \text{P}(\{p_i^k\}|\text{background})} \quad , \quad (3)$$

with $\text{P}(\{p_i^k\}|\text{signal})$ being the weight for the hypothesis that a signal process leads to the observed configuration $\{p_i^k\}$ and the sum in the numerator is over all showers, in which signal processes lead to this configuration. Similarly, the denominator sums the weights for the background processes. If χ is larger than a certain cut value, the large- R jet is tagged as a top jet. By adjusting the threshold value for χ , the tagging efficiency can be changed continuously.

The inputs to SD are the four-momenta of the subjets in the large- R jet. SD has an internal mechanism to suppress pile-up, which is based on the fact that the weights of the likelihood ratio contain the probability that a subset of the subjets did not originate from the hard interaction but are the result of pile-up. Details can be found in Refs. [19, 20]. In this paper, trimmed anti- k_t $R = 1.0$ jets are used as input to SD, but the subjets of the untrimmed jet are fed to the SD algorithm, and the kinematic properties (p_T , η) of the trimmed jet are only used to preselect the signal sample. This procedure avoids interference of the trimming with the SD-internal pile-up suppression.

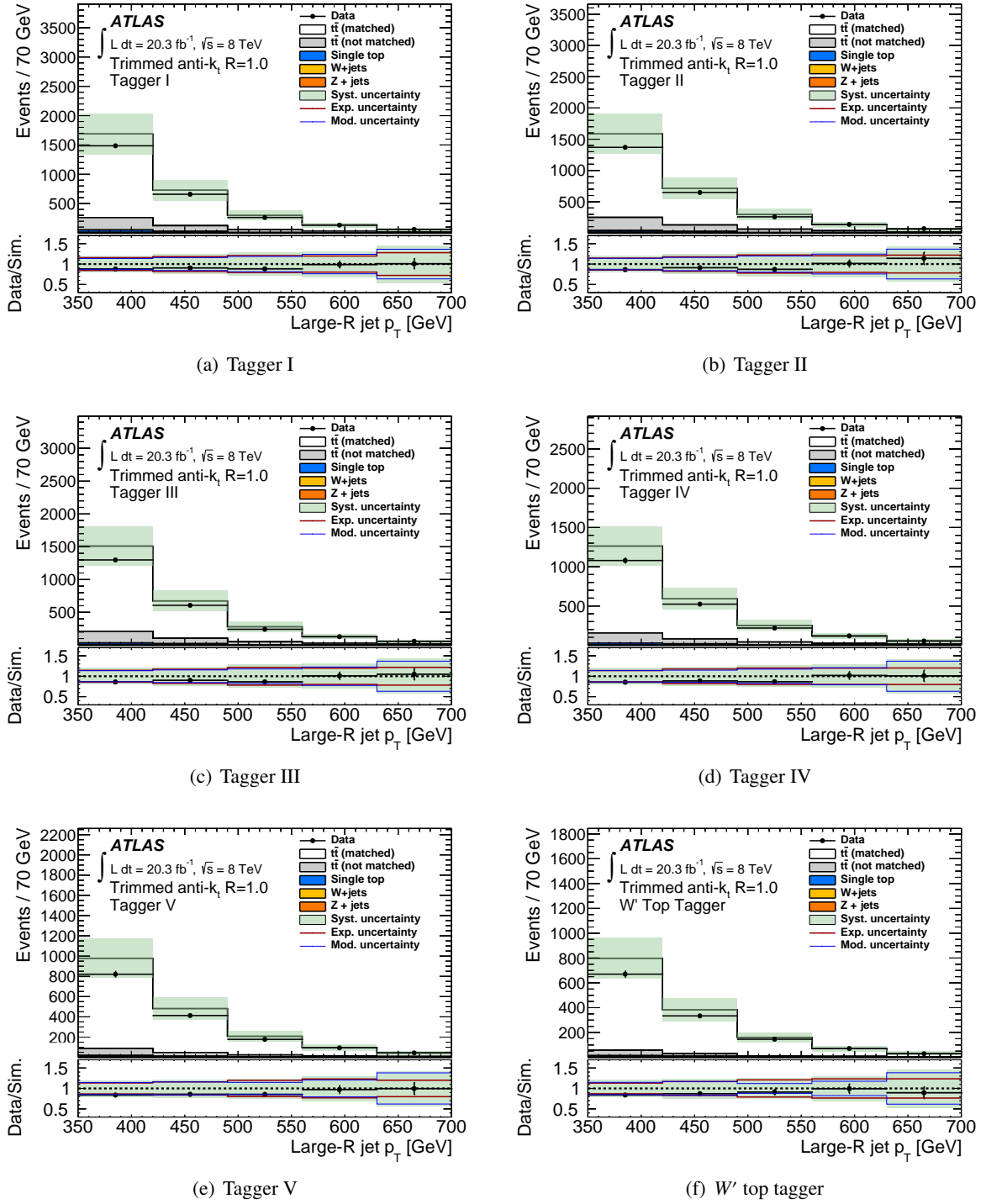


Figure 4: Detector-level distributions of the p_T of the highest- p_T trimmed anti- k_r $R = 1.0$ jet after tagging with different top taggers based on substructure variables in events passing the signal selection. The vertical error bar indicates the statistical uncertainty of the measurement. Also shown are distributions for simulated SM contributions with systematic uncertainties (described in Section 6) indicated as a band. The $t\bar{t}$ prediction is split into a *matched* part for which the large- R jet axis is within $\Delta R = 0.75$ of the flight direction of a hadronically decaying top quark and a *not matched* part for which this criterion does not hold. The ratio of measurement to prediction is shown at the bottom of each subfigure and the error bar and band give the statistical and systematic uncertainties of the ratio, respectively. The impacts of experimental and $t\bar{t}$ modelling uncertainties are shown separately for the ratio.

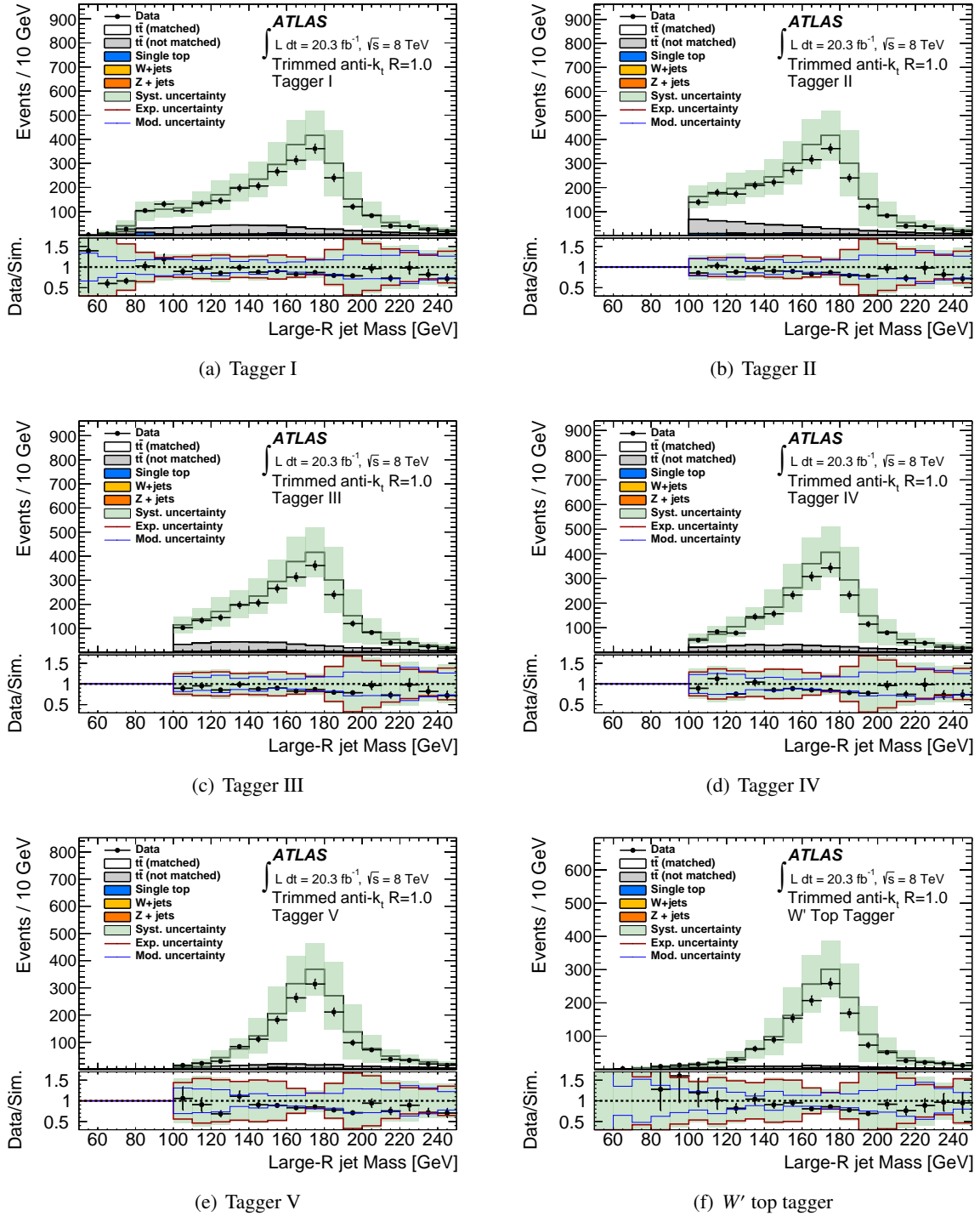


Figure 5: Distribution of the mass of the highest- p_T trimmed anti- k_t , $R = 1.0$ jet after tagging with different top taggers based on substructure variables in events passing the signal selection. The vertical error bar indicates the statistical uncertainty of the measurement. Also shown are distributions for simulated SM contributions with systematic uncertainties (described in Section 6) indicated as a band. The $t\bar{t}$ prediction is split into a *matched* part for which the large- R jet axis is within $\Delta R = 0.75$ of the flight direction of a hadronically decaying top quark and a *not matched* part for which this criterion does not hold. The ratio of measurement to prediction is shown at the bottom of each subfigure and the error bar and band give the statistical and systematic uncertainties of the ratio, respectively. The impacts of experimental and $t\bar{t}$ modelling uncertainties are shown separately for the ratio.

To obtain the best SD performance, the smallest structures in the flow of particles should be resolved by the subjets used as input to SD. Therefore, $C/A R = 0.2$ subjets are used, as they are the jets with the smallest radius parameter for which ATLAS calibrations and calibration uncertainties have been derived [18, 76]. Only the nine hardest subjets of the large- R jet are used in the present study to reduce the processing time per event, which grows with the number of subjets considered in the calculation. The signal weight is zero for large- R jets with fewer than three subjets because a finite signal weight requires the existence of at least three subjets which are identified with the three partons from the top-quark decay. To speed up the computation of the signal weights, the signal weight is set to zero if no combination of at least three subjets can be found that has an invariant mass within a certain range around the top-quark mass. The rationale for this mass requirement is that subjet combinations outside of this mass range would receive only a very small (but finite) weight due to the Breit–Wigner distribution assumed for the signal hypothesis. Similarly, a subset of the subjets which have a combined invariant mass close to the top-quark mass must give an invariant mass within a given range around the W -boson mass. Due to detector effects, the values of these ranges around the top-quark mass and the W -boson mass must be tuned to optimize the performance and cannot be extracted directly from the model. The values used in this study are a range of 40 GeV around a top-quark mass of 172 GeV and a range of 20 GeV around a W -boson mass of 80.4 GeV. For the background hypothesis, no constraint on the subjet multiplicity is present and also no mass-range requirements are imposed.

Distributions of the multiplicity and p_T of $C/A R = 0.2$ subjets found in the untrimmed anti- k_r , $R = 1.0$ jets from the signal selection are shown in Figure 6. These subjets are used as input to SD and must satisfy the kinematic constraints $p_T > 20$ GeV and $|\eta| < 2.1$. The subjet multiplicity of the large- R jet is shown in Figure 6(a). Most of the large- R jets have two or three subjets and only a small fraction have more than four subjets. Of the large- R jets, 41% have fewer than three subjets and are hence assigned a SD signal weight of zero. The simulation describes the data within statistical and systematic uncertainties indicating that the input to the SD algorithm, the subjet multiplicity and kinematics, are well described. For two and three subjets, the uncertainty is dominated by uncertainties in the large- R JES and the PDF. For one subjet and for four or more subjets, as well, the uncertainty is dominated by the subjet energy-resolution uncertainty. The source of most events with only one subjet is not-matched $t\bar{t}$, for which the modelling of additional low- p_T radiation exceeding the minimum subjet p_T depends on the precision of the subjet energy scale and resolution. The same effect is present for four or more subjets, because hadronically decaying top quarks are expected to give rise to a distinct three-subjet structure and additional subjets may be due to additional low- p_T radiation close to the top quark.

The p_T distributions of the three hardest subjets are shown in Figures 6(b)–6(d). The p_T of the highest- p_T subjet is larger than ≈ 100 GeV and has a broad peak from 200 to 400 GeV. The shoulder at 370 GeV is caused by large- R jets from not-matched $t\bar{t}$ and W +jets background, as many of these jets have only one subjet, as shown in Figure 6(a), and in that case the single subjet carries most of the momentum of the large- R jet, i.e. most of the momentum is concentrated in the core of the jet. Therefore, the shoulder at 370 GeV is due to the requirement $p_T > 350$ GeV for the large- R jet. The systematic uncertainty in the region mainly populated by jets with one dominant subjet ($p_T > 350$ GeV) or by jets with many subjets ($100 < p_T < 150$ GeV) in Figure 6(a) has sizeable contributions from the modelling of the subjet properties, here the subjet energy scale. While the large- R JES also contributes for $100 < p_T < 150$ GeV, it is dominant for jets mainly showing the expected distinct two-subjet or three-subjet structure ($150 < p_T < 350$ GeV). For $p_T > 500$ GeV, the largest uncertainty results from the difference between the $t\bar{t}$ generators, as this is the main source of uncertainties for the modelling of $t\bar{t}$ events in the upper range of the p_T spectrum studied.

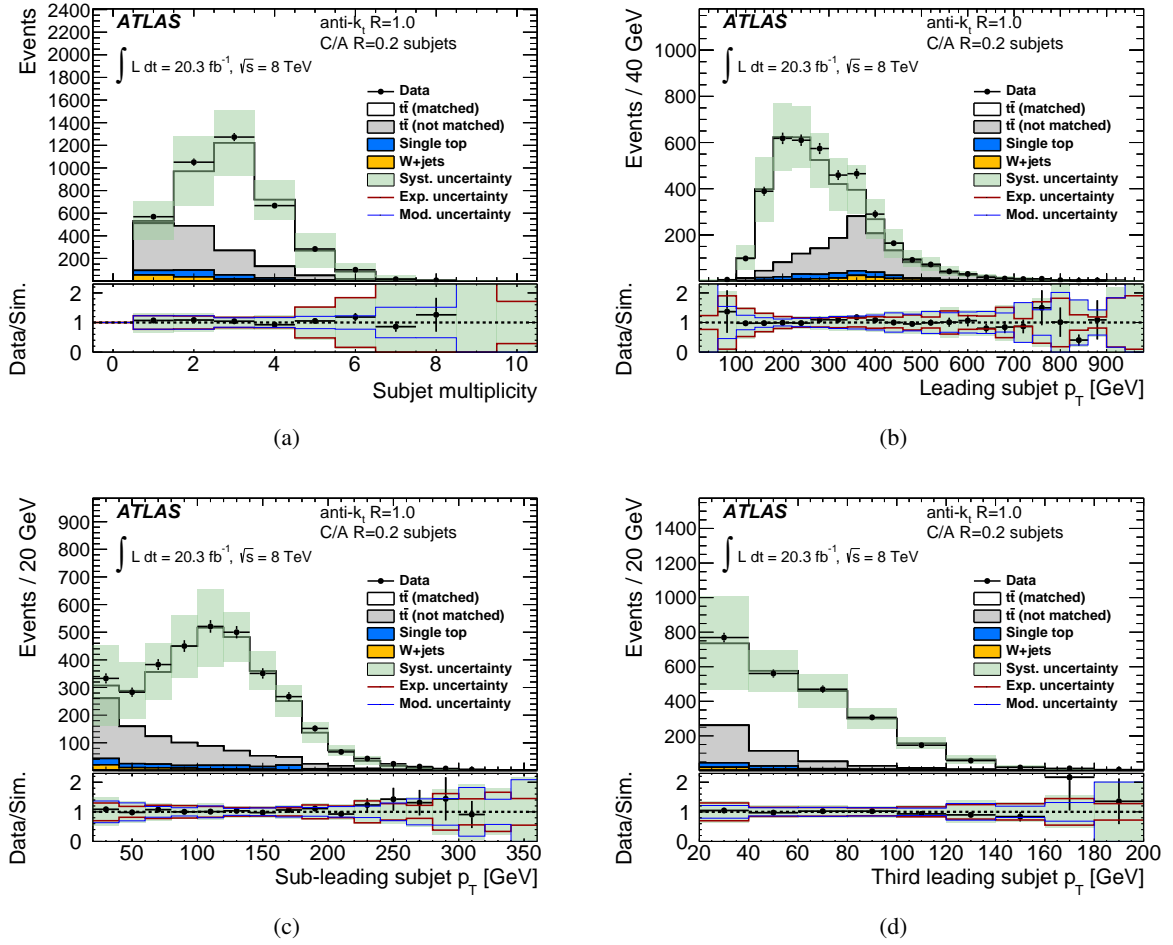


Figure 6: Detector-level distributions of $C/A R = 0.2$ subjects found in the untrimmed anti- $k_t R = 1.0$ jet corresponding to the highest- p_T trimmed anti- $k_t R = 1.0$ jet with $p_T > 350$ GeV in the signal selection: (a) the subject multiplicity, and (b) the p_T of the highest- p_T subject, (c) the second-highest- p_T subject, and (d) the third-highest- p_T subject. The vertical error bar indicates the statistical uncertainty of the measurement. Also shown are distributions for simulated SM contributions with systematic uncertainties (described in Section 6) indicated as a band. The $t\bar{t}$ prediction is split into a *matched* part for which the large- R jet axis is within $\Delta R = 0.75$ of the flight direction of a hadronically decaying top quark and a *not matched* part for which this criterion does not hold. The ratio of measurement to prediction is shown at the bottom of each subfigure and the error bar and band give the statistical and systematic uncertainties of the ratio, respectively. The impacts of experimental and $t\bar{t}$ modelling uncertainties are shown separately for the ratio.

For the second-highest subject p_T , the background distribution peaks near the 20 GeV threshold. These are subjects in large- R jets with only two subjects where the highest- p_T subject carries most of the large- R jet momentum. These asymmetric configurations, where the highest- p_T subject carries a much larger p_T than the second-highest- p_T subject, are seen mainly for the not-matched $t\bar{t}$ and W +jets processes. The acceptance limit at 20 GeV cuts into the p_T distributions of all but the highest- p_T subject, as also seen for the distribution of the third-highest- p_T subject. The uncertainties in the distributions of the second-highest- p_T and third-highest- p_T subject are again dominated by the uncertainty of the subject modelling, i.e. the subject energy-resolution and energy-scale modelling, for low values of p_T (mostly populated by

not-matched $t\bar{t}$ events) and for high values of p_T . For intermediate values (60–150 GeV for the second-highest- p_T subjet and 40–100 GeV for the third-highest- p_T subjet), where jets with a distinct top-like subjet structure dominate the distributions, the large- R JES uncertainty dominates. If $40 < p_T < 60$ GeV for the second-highest subjet, the large- R JES uncertainty contributes significantly, but does not dominate due to significant contributions from the PDF and generator uncertainties.

The following invariant masses of combinations of the $C/A R = 0.2$ subjets are shown in Figure 7 for events fulfilling the signal selection: the mass of the two highest- p_T subjets, m_{12} , the mass of the second-highest- p_T and third-highest- p_T subjet, m_{23} , and the mass of the three hardest subjets, m_{123} . These distributions illustrate some of the masses built from subjet combinations which are used by SD to reject subjet combinations that lead to masses outside the top-quark and W -boson mass ranges. Also these distributions are described by the simulation within statistical and systematic uncertainties and give further confidence in the description of the inputs to the SD algorithm. The uncertainty for large values of m_{12} , m_{23} and m_{123} , i.e. for values larger than 140 GeV, 120 GeV and 165 GeV, respectively, is dominated by the subjet energy-scale uncertainty, consistent with this uncertainty also being dominant for large values of the subjet transverse momenta (Figure 6). The parts of the distributions which are populated with jets showing primarily a distinct top-like substructure again show large contributions from the large- R JES uncertainty ($60 < m_{12} < 140$ GeV, $80 < m_{23} < 120$ GeV, $135 < m_{123} < 165$ GeV), where the ISR/FSR and the subjet JES uncertainties also contribute for m_{23} . For lower values, the three different invariant masses are all sensitive to radiation effects in a region populated by not-matched $t\bar{t}$ events, i.e. jets which do not originate from a hadronically decaying top quark. ISR/FSR uncertainties contribute to $20 < m_{12} < 30$ GeV, the subjet energy resolution contributes significantly to $m_{23} < 60$ GeV and $m_{123} < 135$ GeV, and also the PDF uncertainty has an increasing effect with increasing m_{23} for $10 < m_{23} < 60$ GeV with the uncertainty from the subjet energy resolution decreasing with increasing m_{23} . For $20 < m_{12} < 30$ GeV, the large- R JES uncertainty dominates the total uncertainty together with the ISR/FSR uncertainty. For $m_{23} < 10$ GeV, the uncertainty is dominated by the uncertainty on the subjet energy resolution and the differences between the $t\bar{t}$ generators. For $30 < m_{12} < 60$ GeV, the choice of $t\bar{t}$ generator and the large- R JES dominate the total uncertainty.

The distributions of the SD weights and the ratio of the weights, i.e. the final discriminant χ (Eq. (3)), are shown in Figure 8 for events fulfilling the signal-selection criteria. For $\approx 60\%$ of the large- R jets, the signal weight is zero because there are fewer than three subjets or the top-quark or W -boson mass-window requirements are not met. These cases are not shown in Figure 8. The natural logarithm of the sum $\sum_{\text{perm.}} \text{P}(\{p_i^k\}|\text{signal})$ of all weights obtained with the assumption that the subjet configuration in the large- R jet is the result of a hadronic top-quark decay is shown in Figure 8(a). The logarithm of the sum of all weights for the background hypothesis is shown in Figure 8(b). For the signal hypothesis the distribution peaks between -23 and -21 , while for the background hypothesis the peak is at lower values, between -26 and -25 . The logarithm of the ratio of the sums of the weights χ , is shown in Figure 8(c). The $\ln \chi$ distribution is also shown in Figure 8(d) for large- R jet $p_T > 550$ GeV, which defines a different kinematic regime for which the probability to contain all top-quark decay products in the large- R jet is higher than for the lower threshold of 350 GeV. All distributions of SD output variables are described by simulation within the statistical and systematic uncertainties. The subjet energy-resolution uncertainty dominates for low values of the logarithm of the SD signal weight (region < -26), the logarithm of the SD background weight (region < -30) and $\ln \chi$ (region < 1 in Figure 8(c)). Hence, this uncertainty dominates, consistent with the observations in previous figures, in the phase space not primarily populated by jets from hadronically decaying top quarks. The large- R JES contributes significantly for the central parts of the signal-weight distribution, i.e. from -26 to -23 in Figure 8(a), and $\ln \chi$, i.e. from 1 to 5 in Figure 8(c). In the region, $1 < \ln \chi < 5$, there are equally large contributions to the total uncertainty from

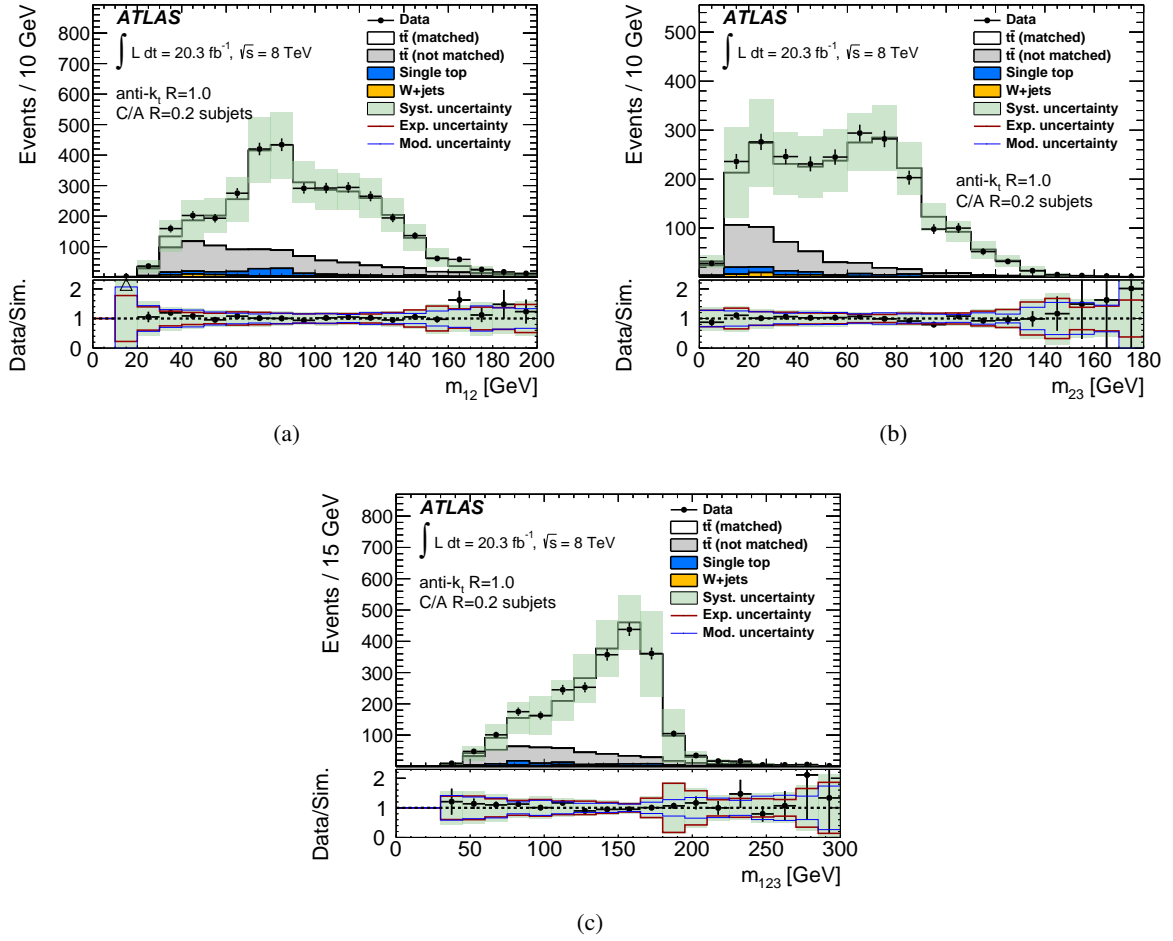


Figure 7: Distributions of invariant masses of combinations of C/A $R = 0.2$ subjects found in the untrimmed anti- k_t $R = 1.0$ jet corresponding to the highest- p_T anti- k_t $R = 1.0$ trimmed jet with $p_T > 350$ GeV in the signal selection: (a) the invariant mass of the highest- p_T subject and the second-highest- p_T subject, (b) the mass of the second- and third-highest- p_T subjects, (c) the mass of the three highest- p_T subjects. The vertical error bar indicates the statistical uncertainty of the measurement. Also shown are distributions for simulated SM contributions with systematic uncertainties (described in Section 6) indicated as a band. The $t\bar{t}$ prediction is split into a *matched* part for which the large- R jet axis is within $\Delta R = 0.75$ of the flight direction of a hadronically decaying top quark and a *not matched* part for which this criterion does not hold. The ratio of measurement to prediction is shown at the bottom of each subfigure and the error bar and band give the statistical and systematic uncertainties of the ratio, respectively. The impacts of experimental and $t\bar{t}$ modelling uncertainties are shown separately for the ratio.

the subjet energy resolution, ISR/FSR, and the parton-shower modelling uncertainties. For larger values of the signal weight, from -23 to -21 in Figure 8(a), there are sizeable contributions from the subjet energy-resolution uncertainty. The uncertainty from the large- R JES dominates in the highest bins of the distribution (> -20). ISR/FSR uncertainties and the uncertainty in the subjet energy scale dominate for $\ln \chi > 5$ in Figure 8(c). The uncertainties in the bulk of the background-weight distribution (Figure 8(b)) are dominated by the subjet energy-scale and energy-resolution uncertainties (from -30 to -28), the PDF and parton-shower uncertainties (from -28 to -25) and for larger values (> -25) by the uncertainties from the large- R JES and the subjet energy scale.

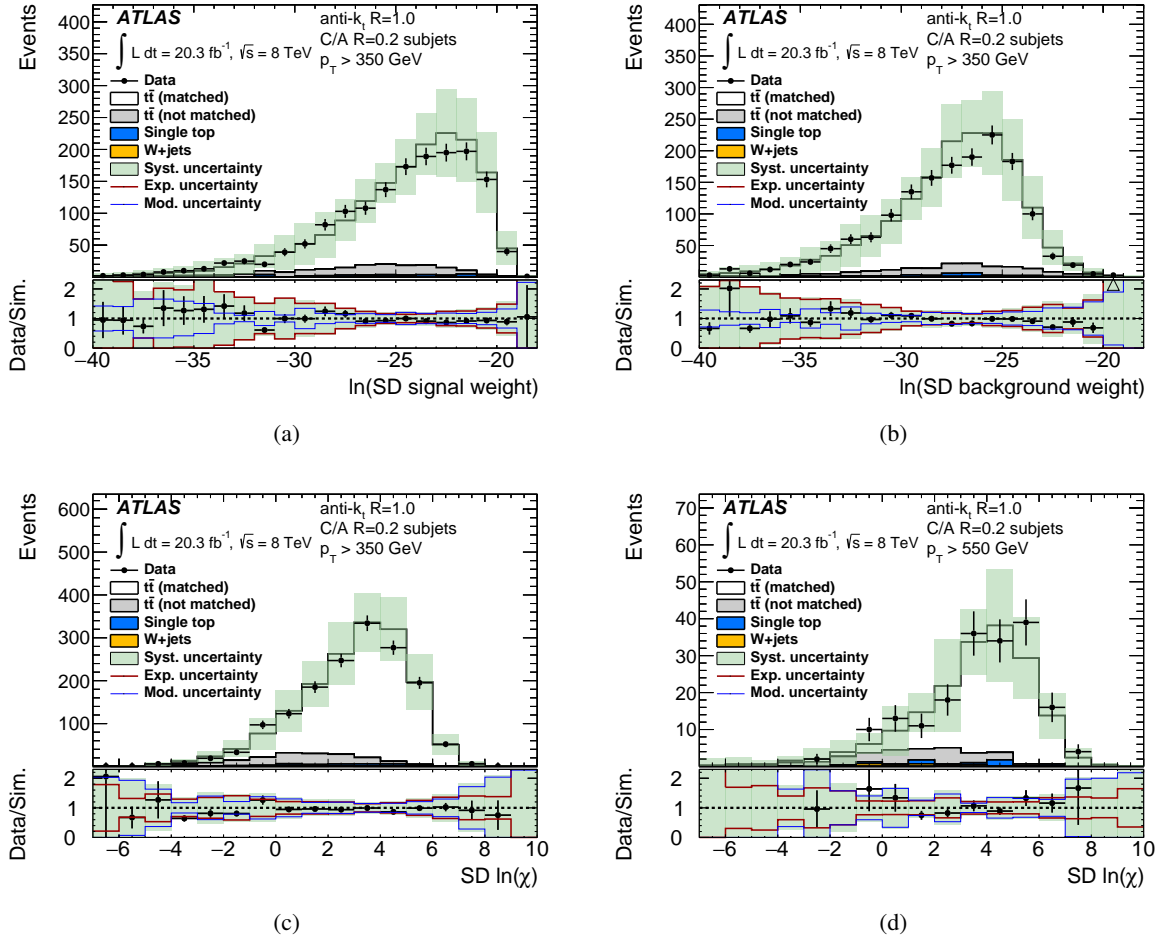
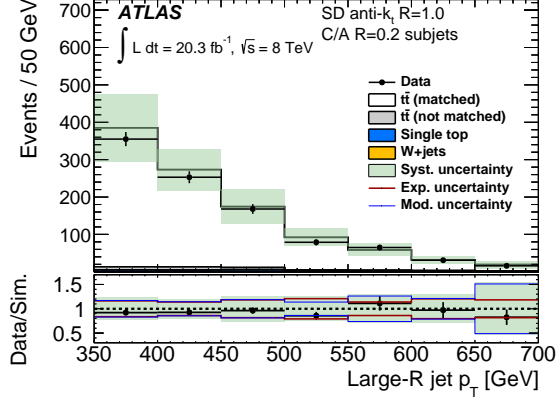
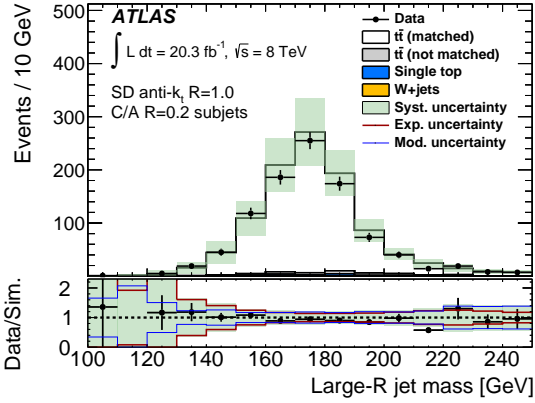


Figure 8: Distributions of Shower Deconstruction weights and the likelihood ratio χ in the signal selection: untrimmed anti- k_t $R = 1.0$ jets corresponding to the highest- p_T trimmed anti- k_t $R = 1.0$ jet with $p_T > 350$ GeV. Cases in which the signal weight is zero because there are fewer than three subjets or the top-quark- or W -boson mass-window requirements are not met (cf. Section 5.2) are not shown. (a) Natural logarithm of the sum of all weights obtained under the assumption that the subject configuration in the large- R jet is the result of hadronic top-quark decay. (b) Natural logarithm of the sum of all weights obtained for the background hypothesis. (c) Distribution of the natural logarithm of the Shower Deconstruction likelihood ratio χ . (d) The same distribution as in (c) but for the requirement that the trimmed large- R jet p_T be larger than 550 GeV. The vertical error bar indicates the statistical uncertainty of the measurement. Also shown are distributions for simulated SM contributions with systematic uncertainties (described in Section 6) indicated as a band. The $t\bar{t}$ prediction is split into a *matched* part for which the large- R jet axis is within $\Delta R = 0.75$ of the flight direction of a hadronically decaying top quark and a *not matched* part for which this criterion does not hold. The ratio of measurement to prediction is shown at the bottom of each subfigure and the error bar and band give the statistical and systematic uncertainties of the ratio, respectively. The impacts of experimental and $t\bar{t}$ modelling uncertainties are shown separately for the ratio.

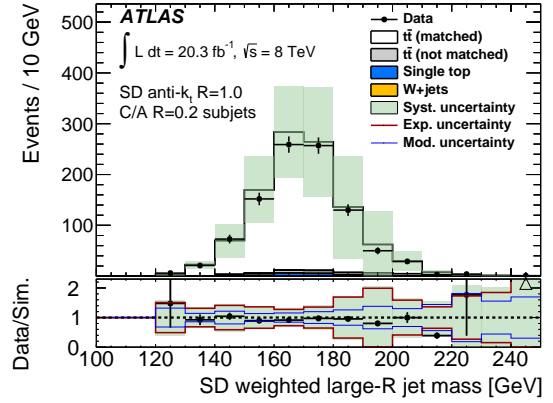
Distributions of the p_T and the mass of anti- k_t $R = 1.0$ jets tagged as top jets by SD using the requirement $\ln(\chi) > 2.5$ are shown in Figure 9 for events passing the signal selection. The p_T (Figure 9(a)) and the mass (Figure 9(b)) are shown for the trimmed version of the anti- k_t $R = 1.0$ jet. The p_T spectrum is smoothly falling and the mass spectrum is peaked at m_t . Both distributions are described by the simulation within the uncertainties. The uncertainty of the simulation for $p_T < 400$ GeV is dominated by the



(a)



(b)



(c)

Figure 9: Distributions for large- R jets which are top tagged by Shower Deconstruction using the requirement $\ln(\chi) > 2.5$ in events passing the signal selection. (a) The transverse momentum and (b) the mass of trimmed anti- k_t , $R = 1.0$ jets for which the corresponding untrimmed anti- k_t , $R = 1.0$ jet is tagged. (c) The mass of the top-quark candidate, where the four-momentum is calculated by taking the weighted average of each signal-hypothesis four-momentum. The vertical error bar indicates the statistical uncertainty of the measurement. Also shown are distributions for simulated SM contributions with systematic uncertainties (described in Section 6) indicated as a band. The $t\bar{t}$ prediction is split into a *matched* part for which the large- R jet axis is within $\Delta R = 0.75$ of the flight direction of a hadronically decaying top quark and a *not matched* part for which this criterion does not hold. The ratio of measurement to prediction is shown at the bottom of each subfigure and the error bar and band give the statistical and systematic uncertainties of the ratio, respectively. The impacts of experimental and $t\bar{t}$ modelling uncertainties are shown separately for the ratio.

uncertainties in the subjet energy scale and on the PDF. From 400 to 500 GeV, important contributions come from the PDF, ISR/FSR, the large- R JES, and the parton shower. Between 500 and 550 GeV, the large- R JES gives the largest contribution. For $p_T > 550$ GeV, the dominant uncertainties are the ones on the PDF and the large- R JES. For masses below 160 GeV, the uncertainty is dominated by the uncertainties in the subjet energy scale and resolution. For masses greater than 210 GeV, the differences between the generators and the PDF uncertainty dominate, consistent with previous figures, where the large- R jet mass distribution receives significant contributions from the generator uncertainty for high mass values. In the mass region 160–210 GeV, multiple sources contribute significantly to the uncertainty.

A top-quark mass distribution can be constructed differently, making use of the SD weights. The signal weights are related to the likelihood of a set of subjets to originate from a top-quark decay. For each set of subjets, a combined four-momentum is built by adding the four-momenta of all subjets in the set. A top-quark four-momentum is then reconstructed as a weighted average of the four-momenta of all possible subjet combinations:

$$p_{\text{SD}}^\kappa = \frac{\sum_{\text{all possible sets of subjets } S} \text{P}(\{p^\kappa(i), i \in S\} | \text{signal large-}R \text{ jet}) \times \sum_i p^\kappa(i)}{\sum_{\text{all possible sets of subjets } S} \text{P}(\{p^\kappa(i), i \in S\} | \text{signal large-}R \text{ jet})}, \quad (4)$$

where $p^\kappa(i)$ is the four-momentum of the i -th subjet. The mass $\sqrt{p_{\text{SD}}^2}$ is shown in Figure 9(c). For the background, this mass takes on values closer to the top-quark mass than in Figure 9(b) because of the use of the signal weights in Eq. (4). Although not directly used in the SD tagging decision, this mass offers a glimpse into the inner workings of SD. The distribution is similar to the distribution of the trimmed jet mass. While the width in the central peak region from 140 to 200 GeV is similar, outliers in the weighted mass are significantly reduced. The distribution is well described by the simulation within statistical and systematic uncertainties. The systematic uncertainties are dominated by the uncertainties in the subjet energy scale and resolution.

5.3. HEPTopTagger

C/A $R = 1.5$ jets are analysed with the *HEPTopTagger* algorithm [21, 22], which identifies the hard jet substructure and tests it for compatibility with the 3-prong pattern of hadronic top-quark decays. This tagger was developed to find top quarks with $p_T > 200$ GeV and to achieve a high rejection of background, which is largest for low- p_T large- R jets. The HEPTopTagger studied in this paper is the original algorithm which does not employ multivariate techniques. An extended version, HEPTopTagger2, has been developed in Ref. [93]. The algorithm makes use of the fact that in C/A jets, large-angle proto-jets are clustered last. The HEPTopTagger has internal parameters that can be changed to optimize the performance, and the settings used in this paper are given in Table 3 and are introduced in the following brief summary of the algorithm.

In the first step, the large- R jet is iteratively broken down into hard substructure objects using a mass-drop criterion [14]. The procedure stops when all substructure objects have a mass below the value m_{cut} . In the second phase, all combinations of three substructure objects are tested for kinematic compatibility with a hadronic top-quark decay. Energy contributions from underlying event and pile-up are removed using a filtering procedure: small distance parameter C/A jets are built from the constituents of the substructure objects using a radius parameter that depends on the distance between these objects but has at most the value $R_{\text{filt}}^{\text{max}}$. The constituents of the N_{filt} highest- p_T jets found in this way (filter jets) are then clustered into three top-quark subjets using the exclusive C/A algorithm. In the final step, kinematic requirements are applied to differentiate hadronic top-quark decays from background. One of the criteria is that one pair of subjets must have an invariant mass in the range $80.4 \text{ GeV} \times (1 \pm f_W)$ around the W -boson mass, with f_W being a parameter of the algorithm. If all criteria are met, the top-quark candidate is built by adding the four-momenta of the N_{filt} highest- p_T filter jets. The large- R jet is considered to be tagged if the top-quark-candidate mass is between 140 and 210 GeV and the top-quark-candidate p_T is larger than 200 GeV. An illustration of the HEPTopTagger algorithm is given in Figure 6 of Ref. [18].

Distributions of the HEPTopTagger substructure variables after requiring a top tag are shown in Figure 10, together with the p_T and mass distributions of the top-quark candidate for events passing the

signal selection. The purity of processes with top quarks ($t\bar{t}$ and single-top production) in this sample is more than 99%. The variable m_{12} (m_{23}) is the invariant mass of the highest- p_T (second-highest- p_T) and the second-highest- p_T (third-highest- p_T) subjet found in the final, i.e. exclusive, subjet clustering step. The variable m_{13} is defined analogously, and the variable m_{123} is the mass of the three exclusive subjets. The ratio m_{23}/m_{123} is used internally in the HEPTopTagger algorithm and is displayed in Figure 10(a). It shows a peak at m_W/m_t , which indicates that in most of the cases, the highest- p_T subjet corresponds to the b -quark. The inverse tangent of the ratio m_{13}/m_{12} is also used internally in the HEPTopTagger algorithm and its distribution is shown in Figure 10(b). The HEPTopTagger top-quark-candidate p_T (Figure 10(c)) is peaked at ≈ 250 GeV and falls smoothly at higher p_T . At around 200 GeV, the tagging efficiency increases strongly with p_T (cf. Section 8.1) and therefore there are fewer entries in the lowest p_T interval from 200 to 250 GeV than would be expected from a falling p_T distribution. The HEPTopTagger top-quark-candidate mass (Figure 10(d)) is peaked near the top-quark mass with tails to lower and higher values. To be considered as HEPTopTagger-tagged, the top-quark candidate must have a mass between 140 and 210 GeV.

The distributions of m_{23}/m_{123} and $\arctan(m_{13}/m_{12})$, as well as the top-quark-candidate p_T and mass are well described by the simulation within statistical and systematic uncertainties. For the two ratios of subjet invariant masses, important sources of systematic uncertainty are the subjet JES, the b -tagging efficiency and the $t\bar{t}$ modelling uncertainties from the choice of the PDF set and the ISR/FSR settings. The choice of PDF set dominates the uncertainty for m_{23}/m_{123} for very low and very high values of the ratio. These uncertainties also contribute to the modelling of the top-quark-candidate p_T and η . The uncertainty in the top-quark-candidate p_T increases with p_T due to increasing uncertainties from the subjet JES, the b -tagging efficiency and the choice of PDF set, as well as from additional $t\bar{t}$ modelling uncertainties due to the choice of generator and parton shower.

A variant of the HEPTopTagger has been developed that uses a collection of small- R jets as input, instead of large- R jets. This variant is referred to as *HEPTopTagger04*, because it is based on small- R jets with $R = 0.4$. This approach can be useful when aiming for a full event reconstruction in final states with many jets in events in which the top quarks have only a moderately high transverse momentum ($p_T > 180$ GeV). The advantages of the method are explained using the performance in MC simulation in Section 7.2.

The HEPTopTagger04 technique proceeds as follows. All sets of up to three anti- k_t $R = 0.4$ jets (small- R jets in the following) are considered, and an early top-quark candidate (not to be confused with the HEPTopTagger candidate) is built by adding the four-momenta of these jets. Only sets with $m_{\text{candidate}} > m_{\text{min}}$ and $p_{T,\text{candidate}} > p_{T,\text{min}}$ are kept and all small- R jets in the set must satisfy $\Delta R_{i,\text{candidate}} < \Delta R_{\text{max}}$. The values of these parameters are given in Table 4. The constituents of the selected small- R jets are then passed to the HEPTopTagger algorithm to be tested with being compatible with a hadronically decaying top quark. The same parameters as given in Table 3 are used. If a top-quark candidate is found with

Parameter	Value
m_{cut}	50 GeV
$R_{\text{filt}}^{\text{max}}$	0.25
N_{filt}	5
f_W	15%

Table 3: The HEPTopTagger parameter settings used in this study.

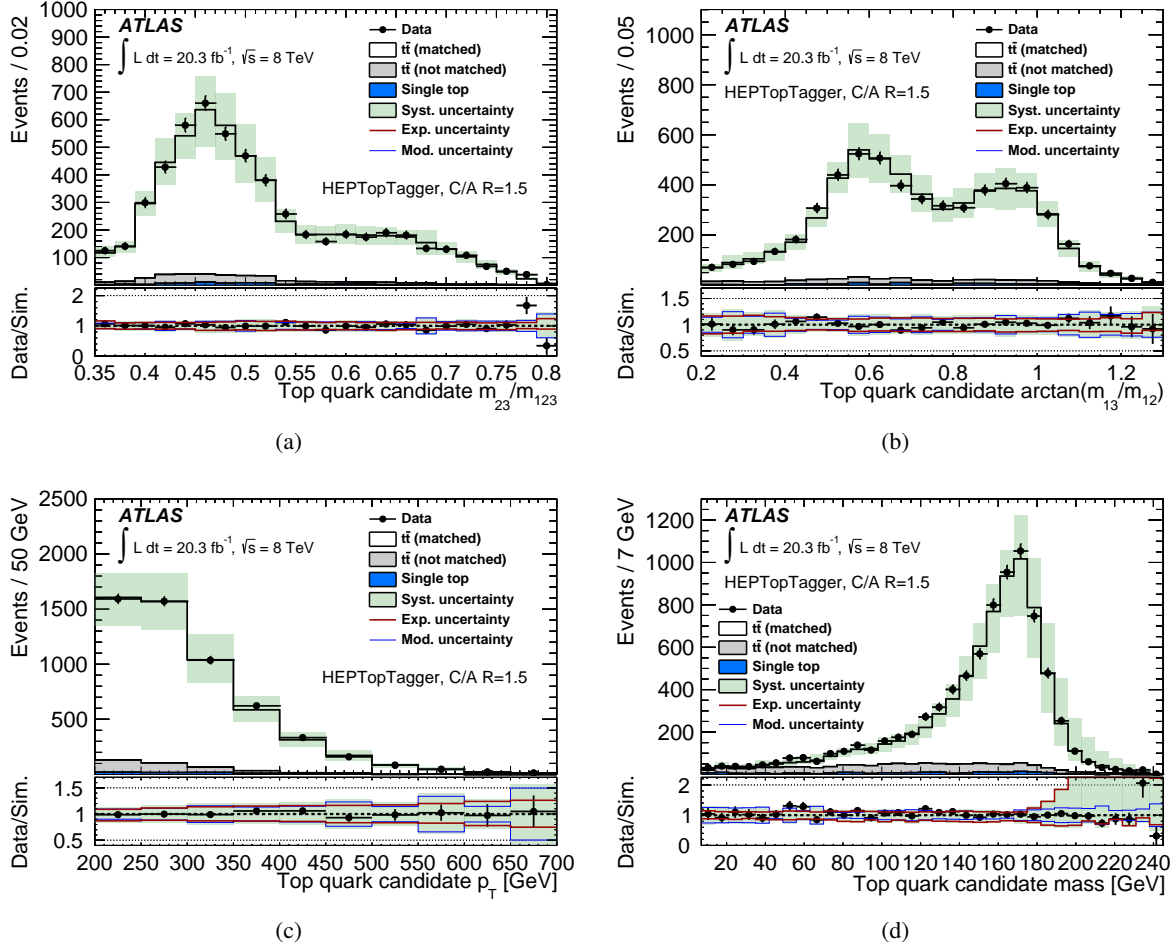


Figure 10: Distributions of HEPTopTagger substructure variables ((a) and (b)) for HEPTopTagger-tagged highest- p_T C/A $R = 1.5$ jets in events passing the signal selection: Shown in (c) and (d) are the p_T and mass of the top-quark candidate, respectively. The vertical error bar indicates the statistical uncertainty of the measurement. Also shown are distributions for simulated SM contributions with systematic uncertainties (described in Section 6) indicated as a band. The $t\bar{t}$ prediction is split into a *matched* part for which the large- R jet axis is within $\Delta R = 1.0$ of the flight direction of a hadronically decaying top quark and a *not matched* part for which this criterion does not hold. The ratio of measurement to prediction is shown at the bottom of each subfigure and the error bar and band give the statistical and systematic uncertainties of the ratio, respectively. The impacts of experimental and $t\bar{t}$ modelling uncertainties are shown separately for the ratio.

the HEPTopTagger algorithm based on the small- R jets' constituents, it is called a HEPTopTagger04 top-quark candidate. If more than one HEPTopTagger04 top-quark candidate is found in an event, they are all kept if they do not share a common input jet. In the case that top-quark candidates share small- R input jets, the largest possible set of top-quark candidates which do not share input jets is chosen. If multiple such sets exist, the set for which the average top-quark-candidate mass is closest to the top-quark mass is selected.

Post-tag distributions from the HEPTopTagger04 approach for events passing the signal selection (but omitting all requirements related to a large- R jet) are shown in Figure 11 and show features similar to the ones described for the HEPTopTagger. Events are classified as matched or not-matched based on

the angular distance between hadronically decaying top quarks and the top-quark candidate, and not the large- R jet as in the other tagging techniques, because for the HEPTopTagger04 no large- R jet exists. The distributions are well described by the simulation within statistical and systematic uncertainties. The systematic uncertainty of the predicted event yield after tagging is approximately 16%, with the largest contributions from the subjet energy scale (8.1%), the uncertainty in initial-state and final-state radiation (8.9%), the $t\bar{t}$ cross-section normalization (6.2%), the PDF uncertainty (5.2%), and the uncertainty in the b -tagging efficiency (5.1%). The uncertainties related to the anti- k_t $R = 0.4$ jets used as input to the HEPTopTagger04 method have a negligible impact ($< 1\%$), as the anti- k_t $R = 0.4$ jet energies are only used to select the early top-quark candidate in the HEPTopTagger04 procedure and the HEPTopTagger04 algorithm is run on the constituents of these anti- k_t $R = 0.4$ jets.

6. Systematic uncertainties

The measurements presented in this paper are performed at the detector level, i.e. differential in reconstructed kinematic quantities and not corrected for detector effects such as limited efficiency and resolution. The measured distributions are compared with SM predictions obtained from MC-generated events which have been passed through a simulation of the detector and are reconstructed in the same way as the data. Systematic uncertainties of the predictions can be grouped into different categories: uncertainties related to the simulation of the detector response and the luminosity measurement, and uncertainties related to the modelling of the physics processes (production cross sections, parton shower, hadronization, etc.).

Systematic uncertainties in the results presented in this paper are obtained by varying parameters of the simulation (one parameter at a time) and repeating the analysis with this varied simulation to determine its impact. The change from the nominal prediction is taken as the 1σ uncertainty related to the uncertainty in the varied parameter. The systematic uncertainties are considered uncorrelated unless otherwise specified.

6.1. Experimental uncertainties

The uncertainty in the integrated luminosity is 2.8%. It is derived from a calibration of the luminosity scale derived from beam-separation scans, following the methodology detailed in Ref. [85].

The b -tagging efficiency is measured using fits to the observed b -tag multiplicity in $t\bar{t}$ events [86, 94] and from jets containing muons [86]. The rate at which jets from charm and light quarks are classified as b -jets (mistag rate) is determined from the distributions of the signed impact parameter and the signed decay

Parameter	Value
m_{\min}	100 GeV
$p_{T,\min}$	140 GeV
ΔR_{\max}	1.1

Table 4: The parameters used in the HEPTopTagger04 technique to build an early top-quark candidate from up to three anti- k_t $R = 0.4$ jets.

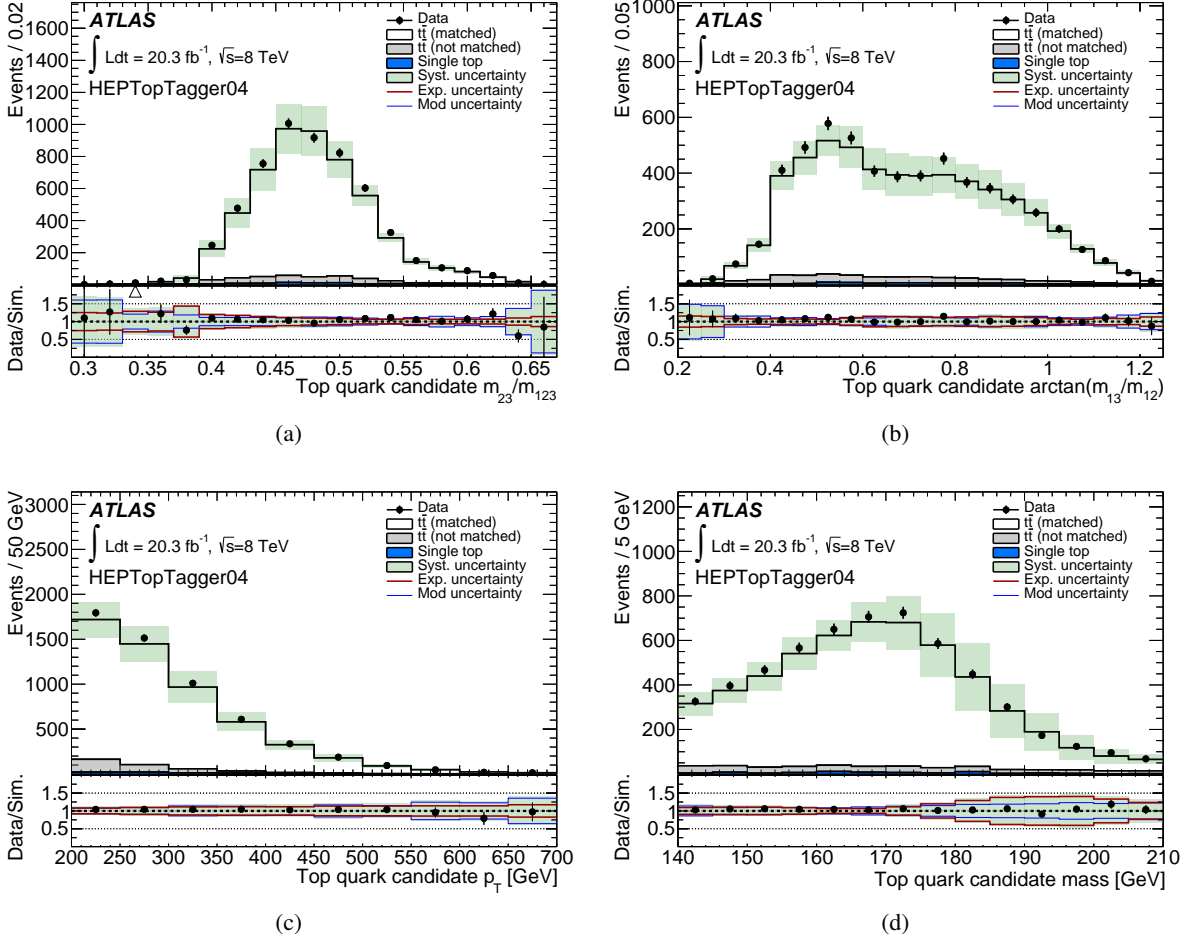


Figure 11: Distributions from the HEPTopTagger04 approach for top tags in events passing the signal selection. (a) and (b) show the HEPTopTagger substructure variables; (c) and (d) show the p_T and mass of the top-quark candidate, respectively. The vertical error bar indicates the statistical uncertainty of the measurement. Also shown are distributions for simulated SM contributions with systematic uncertainties (described in Section 6) indicated as a band. The $t\bar{t}$ prediction is split into a *matched* part for which the top-quark candidate axis is within $\Delta R = 1.0$ of the flight direction of a hadronically decaying top quark and a *not matched* part for which this criterion does not hold. The ratio of measurement to prediction is shown at the bottom of each subfigure and the error bar corresponds to the statistical uncertainty from the measurement and the bands give the statistical and systematic uncertainties of the prediction. The impacts of experimental and $t\bar{t}$ modelling uncertainties are shown separately for the ratio.

length in multijet events [86, 95]. Uncertainties in the b -tagging efficiency and mistag rate in simulation are obtained by comparing the predictions with the measurements. The uncertainty in the mistag rate has a negligible impact on the results presented here.

The uncertainties in the lepton trigger, reconstruction and identification efficiencies are determined from $Z \rightarrow ee$ [70, 71] and $Z \rightarrow \mu\mu$ [74] events. Also considered, but found to have negligible impact in the present analysis, are uncertainties in the scale and resolution of the lepton energy and in the E_T^{miss} reconstruction.

Systematic uncertainties related to jet reconstruction are considered as follows. The uncertainty in the

energy scale of anti- k_t $R = 0.4$ jets is determined using a combination of in situ techniques exploiting the transverse-momentum balance between a jet and a reference object such as a photon or a Z boson [78]. The uncertainty in the energy resolution of anti- k_t $R = 0.4$ jets is found to have negligible impact for the results presented here.

The large- R jets and subjets used in this analysis are reconstructed from calorimeter information. Systematic uncertainties related to the modelling of the calorimeter response in simulation are estimated by comparing these jets to tracks which are matched to the jets [18]. Uncertainties in the following quantities are estimated in this way: the energy scale of the large- R jets; the k_t splitting scales, the N -subjettiness ratios, and the mass of trimmed anti- k_t $R = 1.0$ jets; the subjet energy scale for SD. For $p_T < 900$ GeV of trimmed anti- k_t $R = 1.0$ jets, the uncertainty is not derived from the track-jet method, but using γ +jet events and an additional uncertainty based on the difference between the calorimeter's response to QCD jets and jets from $t\bar{t}$ decays. The uncertainties in the k_t splitting scales, the N -subjettiness ratios and the trimmed mass are 4–7% for p_T between 350 and 700 GeV, depending on the jet p_T , η and the ratio m/p_T . For values of $m/p_T < 0.1$, the uncertainties are larger and reach values of up to 10%. The subjet energy-scale uncertainty for the HEPTopTagger is determined in situ from the reconstructed top-quark mass peak as described in Section 6.2. The correlations between the uncertainties in the substructure variables used by taggers I–V and the W' top tagger have not been determined; the largest observed variations are used based on testing different combinations of zero and full (anti-)correlation of the systematic uncertainties of the different substructure variables.

The energy-resolution uncertainties for C/A $R = 1.5$ jets and for subjets used by SD and the HEPTopTagger are determined using the p_T balance in dijet events [18]. To determine the impact of the energy-resolution uncertainty for trimmed anti- k_t jets with $R = 1.0$, the energy resolution in simulation is scaled by 1.2. The impact of the mass-resolution uncertainty for trimmed anti- k_t $R = 1.0$ jets is estimated analogously.

6.2. In situ determination of the subjet energy scale for the HEPTopTagger

The top-quark candidates identified with the HEPTopTagger in the μ +jets channel of the signal selection are used to determine the subjet energy scale for the HEPTopTagger. For this study, the signal selection with only the b -tag close to the lepton is used and the second b -tag requirement with $\Delta R > 1.5$ from the lepton direction is omitted. With this change, the μ +jets channel alone provides sufficient events to perform this study. The four-momentum of the top-quark candidate is obtained in the HEPTopTagger by combining the calibrated subjet four-momenta. A change in the subjet p_T is therefore reflected in a change of the top-quark-candidate momentum. The top-quark peak in the distribution of the top-quark-candidate mass can be used to constrain the energy-scale uncertainty of the subjets as suggested in Ref. [96]. The method consists of varying the energy scale of the calibrated subjets in simulation and comparing the resulting top-quark mass distribution to the one from data. A higher (lower) subjet energy scale shifts the predicted distribution to larger (smaller) masses. This shift is constrained by the necessity to describe the measured mass peak within uncertainties.

The subjet energy-scale uncertainty is determined by calculating a χ^2 value for different variations of the energy scale. The χ^2 is calculated in the mass window from 133 to 210 GeV, in 11 bins of width 7 GeV. The statistical uncertainties of the measured and predicted number of top-quark candidates in each bin are taken into account, as well as all systematic uncertainties other than that of the subjet energy scale

itself. The systematic uncertainties due to the imperfect modelling of the physics processes (Section 6.3) are considered, including a systematic uncertainty in the top-quark mass of ± 1 GeV.

Variations of the subjet energy scale are considered by raising or lowering all subjet transverse momenta in a correlated way:

$$p_T \rightarrow p_T \times (1 \pm f), \quad (5)$$

in which f is a function which specifies the relative variation. Three different scenarios for the dependence of f on the subjet p_T are considered (the parameters k_i are constants):

- $f = k_1 \sqrt{p_T}$ (larger variation for high-energy subjets),
- $f = k_2/p_T$ (larger variation for low-energy subjets),
- $f = k_3$ (no p_T dependence, variation by a constant factor).

Separate χ^2 values are determined for all three functional forms and for different values of the parameters k_i . The HEPTopTagger top-quark-candidate mass distribution is shown in Figure 12(a). The simulation is shown for the nominal energy scale and, as an example, for the case of the variation with $f = k_2/p_T$ with $k_2 = 1$ GeV. For subjets with $p_T = 100$ GeV, this corresponds to a relative change of the transverse momentum of $\pm 1\%$. The description of the measured distribution is improved by the $+1\%$ variation. The level of agreement between the measured and predicted distributions is quantified in terms of the χ^2 value shown in Figure 12(b) for different values of k_2 . The variation is expressed as the relative p_T change for subjets with $p_T = 100$ GeV (JES shift). A parabola is fitted to the χ^2 values as a function of the JES shift. The best agreement is obtained for a JES shift of $+1\%$, which leads to the smallest χ^2 , χ^2_{\min} . This result can be used to correct the subjet p_T scale in the simulation. This is left to future studies. Here, an uncertainty in the p_T scale is determined as follows. From the two JES-shift values that correspond to $\chi^2 = \chi^2_{\min} + 1$, the larger absolute value is used as the 1σ systematic uncertainty of the p_T scale. In Figure 12(b) this uncertainty is 2.2% .

The subjet energy-scale uncertainty is determined in two bins of large- R -jet p_T (< 320 GeV, > 320 GeV) and two bins of large- R jet pseudorapidity ($|\eta| < 0.7$, $0.7 < |\eta| < 2.0$). The results are shown in Figure 13. The largest relative uncertainty is 10% at a subjet p_T of 20 GeV, dropping with $1/p_T$ to 2.5% at 90 GeV and then rising proportionally to $\sqrt{p_T}$, reaching $3.5\text{--}4.0\%$ at 200 GeV. The uncertainty depends weakly on the large- R jet p_T and η .

In the HEPTopTagger analysis, the impact on each studied quantity (the number of tagged large- R jets, the tagging efficiency, and the mistag rate) is determined for all three functional forms. The largest of the three changes in the quantity is then used as the uncertainty related to the imperfectly known subjet energy scale.

6.3. Uncertainties in the modelling of physics processes

Uncertainties related to the $t\bar{t}$ simulation are taken into account as follows. If the uncertainties are estimated from samples not generated with the nominal $t\bar{t}$ generator POWHEG+PYTHIA, then the sequential p_T reweighting mentioned in Section 3 is not applied, because the reweighting used only applies to POWHEG+PYTHIA: the nominal POWHEG+PYTHIA prediction without reweighting is compared to the prediction from the alternative simulation without reweighting.

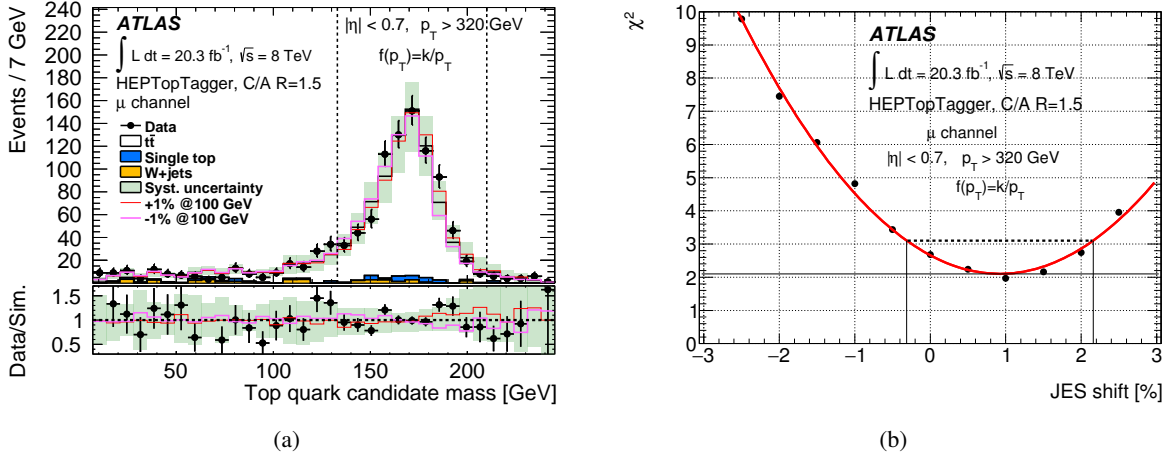


Figure 12: (a) The HEPTopTagger top-quark candidate mass distribution reconstructed in the μ +jets signal selection from $C/A R = 1.5$ jets with $p_T > 320$ GeV and $|\eta| < 0.7$. Only one b -tag within $\Delta R < 1.5$ of the lepton is required and the second b -tag requirement is omitted. Also shown are predictions for $t\bar{t}$, single top, and W +jets production with the nominal subjet energy scale and with the subjet p_T multiplied by $1 + f$ (label ‘+1% @100 GeV’) and $1 - f$ (‘-1% @100 GeV’) with $f = 1 \text{ GeV}/p_T$, corresponding to shifts of $\pm 1\%$ for subjets with $p_T = 100$ GeV. (b) The χ^2 calculated from the measured top-quark candidate mass distribution in the mass window from 133 to 210 GeV as a function of different variations of the simulated subjet energy scale of the form $f = k_2/p_T$. The variation is expressed as the relative p_T change for subjets with $p_T = 100$ GeV (JES shift). The nominal energy scale coincides with no JES shift. The ‘1% @100 GeV’ variation in (a) corresponds to a JES shift of +1% and leads to the smallest χ^2 , χ_{\min}^2 . The distribution is fitted with a parabola and the positive and negative JES-shift values at $\chi_{\min}^2 + 1$ are indicated.

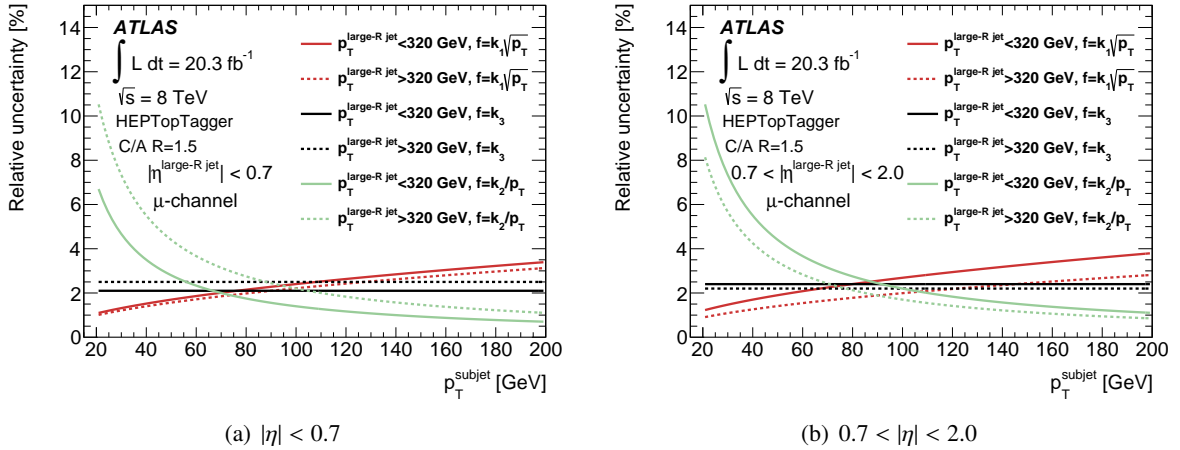


Figure 13: Relative subjet energy-scale uncertainty as a function of the HEPTopTagger subjet p_T for three functional forms of the relative p_T variation. The uncertainty is shown for two pseudorapidity intervals of the $C/A R = 1.5$ jets in which the subjets are found: (a) $|\eta| < 0.7$ and (b) $0.7 < |\eta| < 2.0$. The uncertainty is shown in two bins of the $C/A R = 1.5$ jet p_T .

The $t\bar{t}$ cross-section uncertainty of $^{+13}_{-15}$ pb quoted in Section 3 is used and an additional normalization uncertainty of $^{+7.6}_{-7.3}$ pb from a variation of the top-quark mass by ± 1.0 GeV is added in quadrature, leading

to a total relative normalization uncertainty of $^{+5.9\%}_{-6.6\%}$. For the evaluation of the other $t\bar{t}$ modelling uncertainties mentioned below, the total $t\bar{t}$ cross section of the generated event samples is set to the value given in Section 3, so that no double-counting of normalization uncertainties occurs.

To account for uncertainties in the parton shower, the prediction from POWHEG+Herwig is compared to the prediction from POWHEG+PYTHIA. Uncertainties in the choice of $t\bar{t}$ generator are estimated by comparing the prediction from MC@NLO+Herwig with the prediction from POWHEG+Herwig. The uncertainty in the amount of ISR and FSR is estimated using two ACERMC+PYTHIA $t\bar{t}$ samples with increased and decreased radiation.

PDF uncertainties affect the normalization of the total $t\bar{t}$ cross section and this is taken into account as described in Section 3. They additionally affect the $t\bar{t}$ cross section in the phase space examined by this analysis and the distributions of kinematic variables. These effects are determined by comparing the prediction based on CT10 to the prediction based on HERAPDF1.5. The cross-section difference obtained when comparing these two PDF sets was found to match the difference due to the CT10 PDF uncertainty [54] for this region of phase space.

The factorization and renormalization scales are varied by factors two and one half and the impact on the total $t\bar{t}$ cross section is included in the cross-section uncertainty. The impact in the phase space examined by this analysis and on the distributions of kinematic variables is evaluated by comparing dedicated $t\bar{t}$ samples in which the two scales are varied independently. The variation of the renormalization scale has a significant impact, while the analysis is not sensitive to variations of the factorization scale beyond the change of the total $t\bar{t}$ cross section.

The impact of variations on the top-quark-candidate mass peak of varying the top-quark mass in the generator by ± 1.0 GeV is taken into account for the in situ determination of the subjet energy scale in Section 6.2. For the efficiency and misidentification-rate measurements this uncertainty is negligible compared to other sources of systematic uncertainty.

The uncertainties on the normalization of the single top, W +jets, and Z +jets background contributions were found to have a negligible impact.

7. Study of top-tagging performance using Monte-Carlo simulation

7.1. Comparison of top-tagging performance

The performance of the different top-tagging approaches is compared using MC simulations to relate the different large- R jets used by the taggers and to extend the comparison in large- R jet p_T beyond the kinematic reach of the 8 TeV data samples.

The performance is studied in terms of the efficiency for tagging signal large- R jets and the background rejection, defined as the reciprocal of the tagging rate for background large- R jets. Signal jets are obtained from $Z' \rightarrow t\bar{t}$ events and background jets are obtained from multijet events. Multijets typically pose the largest background in $t\bar{t}$ analyses in the fully hadronic channel. The W +jets background, where the W boson decays hadronically, is less important because of the smaller cross section. Also, in the kinematic region considered in the comparison presented here, it was shown for the HEPTopTagger that the mistag rate is similar for multijet background and background from $W \rightarrow q'\bar{q}$ [18]. In the lepton+jets channel, W +jets tends to be the most important background if the W boson decays leptonically, and then the

background from the additional jets is very similar to the multijets case. The conclusions drawn in this section can therefore be extended to the context of this W +jets background.

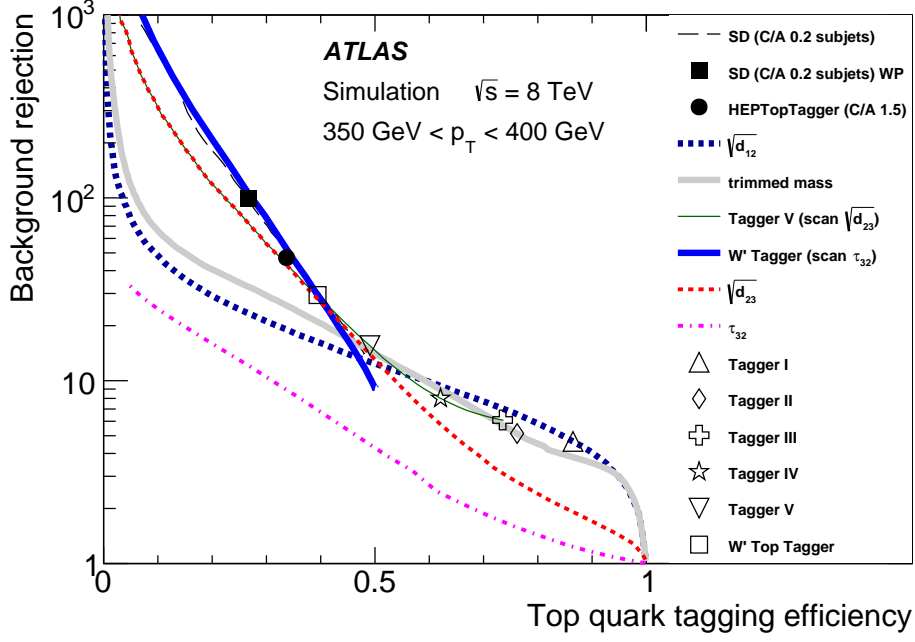
Stable-particle jets are built in all MC events using the anti- k_r algorithm and a radius parameter $R = 1.0$. These jets are trimmed with the same parameters as described in Section 4.1 for the detector-level jets. These particle-level jets are used to relate the different jet types used at reconstruction level. The different types of large- R jets used by the tagging algorithms are listed in Table 1. Each reconstructed large- R jet must be geometrically matched to a particle-level jet within $\Delta R = 0.75$ for the trimmed anti- k_r $R = 1.0$ jets, and within $\Delta R = 1.0$ for the C/A $R = 1.5$ jets. The fraction of reconstructed large- R jets with no matching particle-level jet is negligible. In addition, particle-level jets in the signal sample must be geometrically matched to a hadronically decaying top quark within $\Delta R = 0.75$. The top-quark flight direction at the top-quark decay vertex is chosen, consistent with the matching procedure discussed in Section 4.2.1. The particle-level jet p_T spectrum of the signal sample is reweighted to the p_T spectrum of the background sample to remove the dependence on a specific signal model. However, since the results in this section are given for different ranges of p_T , the conclusions are believed to hold, approximately independently of the choice of specific underlying p_T spectrum.

The comparison is performed in bins of the p_T of the particle-level jet, p_T^{true} , in the range $350 < p_T^{\text{true}} < 1500$ GeV in which all taggers are studied. For the performance comparison, the statistical uncertainties of the simulated efficiencies and rejections are taken into account, while no systematic uncertainties are considered.

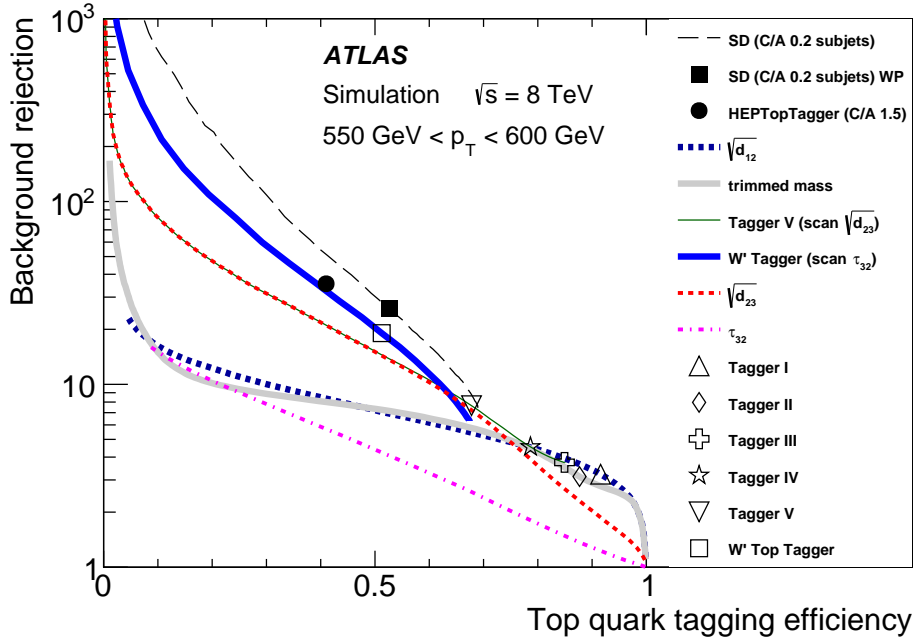
The background rejection is shown as a function of the tagging efficiency in Figures 14 and 15 in four bins of p_T^{true} : 350–400 GeV, 550–600 GeV, 700–1000 GeV, and 1000–1500 GeV. Curves in the efficiency–rejection plane are obtained by varying the values of cuts in the tagger definitions. For the taggers based on substructure variables, scans over the cut values of the trimmed mass, $\sqrt{d_{12}}$, $\sqrt{d_{23}}$, and τ_{32} are shown, and in addition scans over the cut values of $\sqrt{d_{23}}$ in substructure tagger V and of τ_{32} in the W' top tagger, for which the cuts on the other variables are kept at their nominal values. The cuts on the trimmed mass and splitting scales are single-sided lower bounds, and the cut on τ_{32} is a single-sided upper bound.

When using only a single substructure-variable cut, the best performing variables in all studied p_T^{true} intervals are the splitting scale $\sqrt{d_{12}}$ at high efficiency and $\sqrt{d_{23}}$ at lower efficiency. At an efficiency of 80%, a cut on $\sqrt{d_{12}}$ achieves a background rejection of ≈ 3 –6 over the full range in p_T^{true} . At an efficiency of 40%, a cut on $\sqrt{d_{23}}$ achieves a rejection of ≈ 25 for lower values of p_T^{true} , decreasing to a rejection of 15 for $700 < p_T^{\text{true}} < 1000$ GeV and 11 for $1000 < p_T^{\text{true}} < 1500$ GeV, respectively. The efficiency at which the rejection of a cut on $\sqrt{d_{23}}$ is higher than the rejection for the trimmed-mass cut depends on p_T^{true} : it is $\approx 45\%$ for $350 < p_T^{\text{true}} < 400$ GeV and increases to 90% for $1000 < p_T^{\text{true}} < 1500$ GeV. A cut on the trimmed mass performs similarly to the $\sqrt{d_{12}}$ cut. A cut on τ_{32} performs significantly worse. For high efficiencies and the ranges of lower p_T^{true} (e.g. ≈ 60 –90% for $350 < p_T^{\text{true}} < 400$ GeV), the cut on the trimmed mass shows only a small increase in the rejection with decreasing signal efficiency. For lower efficiencies, the rejection increases more strongly with decreasing signal efficiency. This is due to the two distinct W -boson and top-quark mass peaks in signal, as exemplified in Figure 1(a). Adding the cuts on the mass and $\sqrt{d_{12}}$ to the cut on $\sqrt{d_{23}}$ (Tagger V (scan $\sqrt{d_{23}}$)) does not significantly improve the performance over a cut on $\sqrt{d_{23}}$ alone, since for high enough cuts on $\sqrt{d_{23}}$, the other cuts are automatically satisfied because of the relation $m > \sqrt{d_{12}} > \sqrt{d_{23}}$.

A combination of N -subjettiness and splitting-scale information, as used in the W' top tagger, gives the best performance of all studied substructure-variable-based approaches for efficiencies below a certain threshold efficiency. This threshold efficiency is $\approx 40\%$ for $350 < p_T^{\text{true}} < 400$ GeV and it increases to

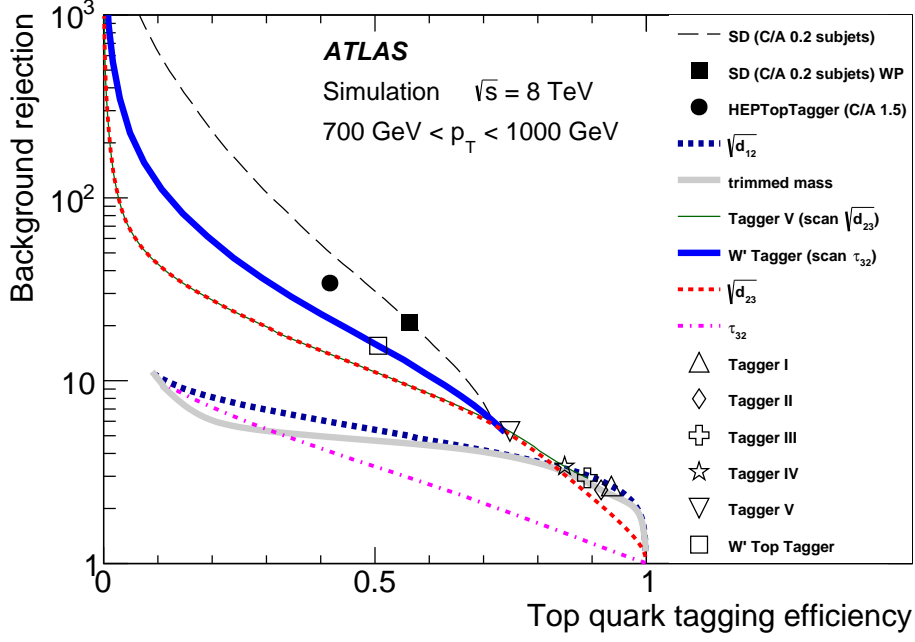


(a)

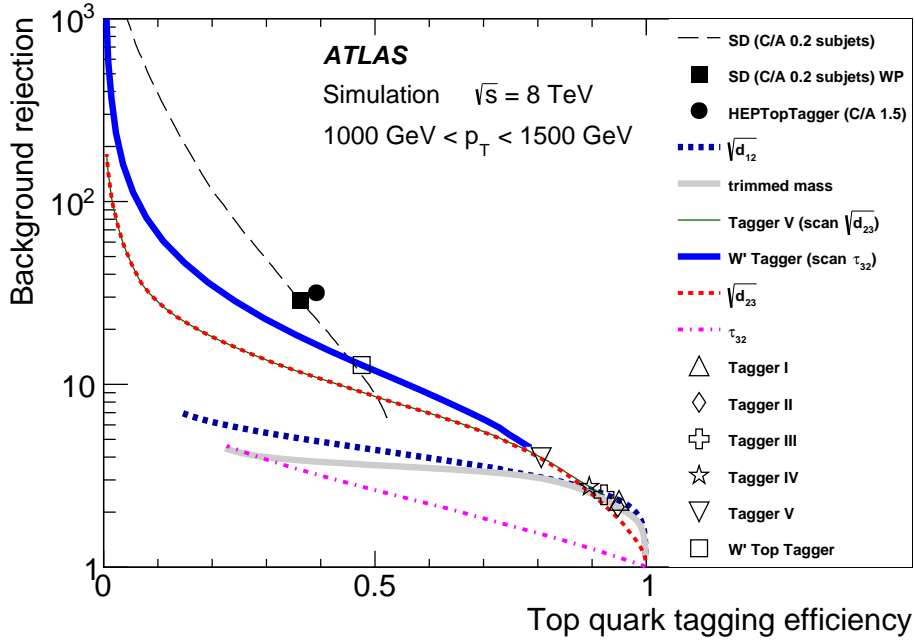


(b)

Figure 14: The background rejection as a function of the tagging efficiency of large- R jets, as obtained from MC simulations for $350 \text{ GeV} < p_T < 400 \text{ GeV}$ and $550 \text{ GeV} < p_T < 600 \text{ GeV}$ for trimmed anti- k_t $R = 1.0$ particle-level jets to which the large- R jets are geometrically matched. The HEPTopTagger uses C/A $R = 1.5$ jets; the other taggers use trimmed anti- k_t $R = 1.0$ jets. For SD, the cut value of the discriminant $\ln\chi$ is scanned over. Substructure-variable-based taggers are also shown including single scans over the trimmed mass, $\sqrt{d_{12}}$, $\sqrt{d_{23}}$, τ_{32} and scans over cuts on $\sqrt{d_{23}}$ and τ_{32} for substructure tagger V and the W' top tagger, respectively. The curves are not shown if the background efficiency is higher than the signal efficiency, which for some substructure-variable scans occurs for very low signal efficiencies, i.e. for scans in the tails of the distributions. The statistical uncertainty from the simulation is smaller than the symbols for the different working points and it is no larger than the width of the lines shown.



(a)



(b)

Figure 15: The background rejection as a function of the tagging efficiency of large- R jets, as obtained from MC simulations for $700 \text{ GeV} < p_T < 1000 \text{ GeV}$ and $1000 \text{ GeV} < p_T < 1500 \text{ GeV}$ for trimmed anti- k_r $R = 1.0$ particle-level jets to which the large- R jets are geometrically matched. The HEPTopTagger uses C/A $R = 1.5$ jets; the other taggers use trimmed anti- k_r $R = 1.0$ jets. For SD, the cut value of the discriminant $\ln \chi$ is scanned over. Substructure-variable-based taggers are also shown including single scans over the trimmed mass, $\sqrt{d_{12}}$, $\sqrt{d_{23}}$, τ_{32} and scans over cuts on $\sqrt{d_{23}}$ and τ_{32} for substructure tagger V and the W' top tagger, respectively. The curves are not shown if the background efficiency is higher than the signal efficiency, which for some substructure-variable scans occurs for very low signal efficiencies, i.e. for scans in the tails of the distributions. The statistical uncertainty from the simulation is smaller than the symbols for the different working points and it is no larger than the width of the lines shown.

$\approx 80\%$ for $1000 < p_T^{\text{true}} < 1500$ GeV. By varying the τ_{32} requirement in the W' top tagger, rejections close to the ones of SD and the HEPTopTagger can be achieved at the same efficiency.

For SD, the cut value of the discriminant $\ln\chi$ is varied. The maximum efficiency is $\approx 50\%$ in the lowest p_T bin studied ($350 < p_T^{\text{true}} < 400$ GeV). For higher p_T , the efficiency rises up to 70% . The maximum efficiency is determined by the requirement of having at least three subjects which combine to an invariant mass near the top-quark mass and a subset of these subjects to give a mass near the W -boson mass. The increase of the maximum efficiency from approximately 50% at $350\text{--}400$ GeV to approximately 70% at $550\text{--}1000$ GeV is a result of the larger average containment of the top-quark decay products in the large- R jet at higher p_T . At the highest p_T values ($1000\text{--}1500$ GeV), the use of $R = 0.2$ subjects limits the efficiency as the top-quark decay products cannot be fully resolved for an increasing fraction of large- R jets, resulting in a maximum efficiency of $\approx 50\%$.

For $350 < p_T^{\text{true}} < 400$ GeV, the HEPTopTagger has an efficiency of 34% at a rejection of 47 . For $p_T^{\text{true}} > 550$ GeV, the efficiency is $\approx 40\%$ and the rejection is ≈ 35 , approximately independent of p_T^{true} . The HEPTopTagger performance was also investigated for $200 < p_T^{\text{true}} < 350$ GeV (not shown): efficiency and rejection are 18% and 300 , respectively, for $200 < p_T^{\text{true}} < 250$ GeV, 22% and 130 for $250 < p_T^{\text{true}} < 300$ GeV, and 28% and 65 for $300 < p_T^{\text{true}} < 350$ GeV.

For $350 < p_T^{\text{true}} < 450$ GeV, the performance of SD, the HEPTopTagger, and the W' top tagger are comparable. For $450 < p_T^{\text{true}} < 1000$ GeV, SD offers the best rejection in simulation, up to its maximum efficiency. Top tagging efficiencies above 70% can be achieved with cuts on substructure variables, where, depending on p_T^{true} , optimal or close-to-optimal performance can be achieved with a requirement on $\sqrt{d_{12}}$ alone. For $1000 < p_T^{\text{true}} < 1500$ GeV, of all the top-tagging methods studied, the HEPTopTagger offers the best rejection (≈ 30) at an efficiency of $\approx 40\%$, making it a viable option for high- p_T searches despite not having been optimized for this p_T regime. The only tagger studied for $200 < p_T^{\text{true}} < 350$ GeV is the HEPTopTagger.

7.2. HEPTopTagger04 performance

The efficiencies for hadronically decaying top quarks to be reconstructed as top-quark candidates with the HEPTopTagger04 and HEPTopTagger methods are shown in Figure 16 as a function of the true p_T of the top quark in simulated $t\bar{t}$ events. The events are selected according to the criteria described in Section 4.2.1, except that all requirements related to large- R jets are not applied in the case of HEPTopTagger04. For these efficiencies, a top quark is considered tagged if a top-quark candidate is reconstructed with a momentum direction within $\Delta R = 1.0$ of the top-quark momentum direction. The definition of the efficiency is therefore different from the large- R -jet-based one used in Section 7.1, where also a different event selection and different matching criteria are applied. The efficiency of the HEPTopTagger04 method increases with the p_T of the top quark and reaches values of $\approx 50\%$ for $p_T > 500$ GeV. The efficiency of the HEPTopTagger04 method is lower than the efficiency of the HEPTopTagger, but follows the trend of the HEPTopTagger efficiency closely. The HEPTopTagger efficiency reaches higher values than in Section 7.1 primarily because the event selection here requires two b -tagged jets.

This efficiency, however, does not take into account the specific needs of event reconstruction in final states with top quarks and many additional jets, for which the HEPTopTagger04 was designed. An example of such a topology in an extension of the SM is the associated production of a top quark and a charged Higgs boson, H^+ , decaying to $t\bar{b}$, i.e. $pp \rightarrow H^+ \bar{t}(b) \rightarrow t\bar{b}\bar{t}(b)$. After the decay of the top quarks,

the final state contains three or four b -quarks. Up to two b -jets not associated with a top-quark decay can in principle be reconstructed, and they should not be part of the reconstructed top-quark candidates.

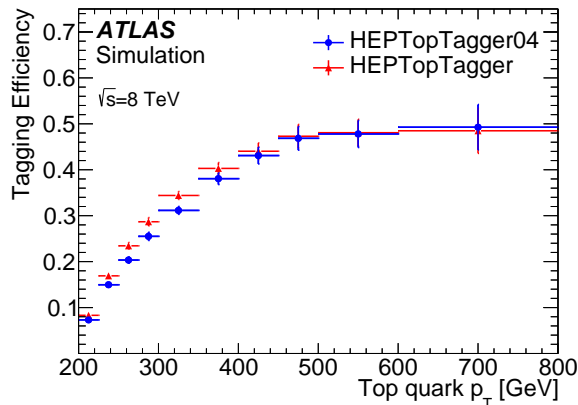


Figure 16: Efficiency to reconstruct and identify a hadronically decaying top quark with the HEPTopTagger04 (blue circles) and the HEPTopTagger (red triangles) as a function of the p_T of the top quark for events passing the signal selection described in Section 4.2.1. A top quark is considered tagged if a top-quark candidate is reconstructed with a momentum direction within $\Delta R = 1.0$ of the top-quark momentum direction.

In ATLAS, b -jets are usually reconstructed using the anti- k_t algorithm with $R = 0.4$. For large H^+ masses, for which the top quarks from its decay may have large p_T , ensuring no overlap between the top-quark candidates and the unassociated b -jets may not be trivial. In this case, hadronically decaying top quarks may be reconstructed with large- R jet substructure analysis. The reconstruction of anti- k_t $R = 0.4$ and large- R jets, however, proceeds independently, so that the same clusters may be present in anti- k_t $R = 0.4$ and large- R jets. If the anti- k_t $R = 0.4$ jet and the large- R jet overlap, the b -tagged anti- k_t $R = 0.4$ jet might also originate from the hadronic top quark decay, which prevents an unambiguous reconstruction of the final state. Moreover, clusters included in both objects may lead to a double-counting of deposited energy, which is an issue if for example an invariant mass is formed from the tagged top and a close-by b -jet targeting the $H^+ \rightarrow t\bar{b}$ decay.

In the case of the HEPTopTagger, subjects of the large- R jet are explicitly reconstructed, and it would be an option to only consider anti- k_t $R = 0.4$ jets not matched to one of the three subjects which form the top-quark candidate as being not associated with a hadronically decaying top. This approach, however, is not straightforward because of the different jet algorithms and jet radii used for HEPTopTagger subjects and b -tagging. A simple approach is to require an angular separation ΔR between the top-quark candidate and the anti- k_t $R = 0.4$ jets in the event, denoted HEPTopTagger+ ΔR in the following. The HEPTopTagger04 is therefore compared to HEPTopTagger+ ΔR , using the latter as a benchmark.

In Figure 17(a), the energy shared by anti- k_t $R = 0.4$ jets and C/A $R = 1.5$ jets is shown for simulated $t\bar{t}$ events. The shared energy is calculated from the clusters of calorimeter cells included as constituents in the small- R and large- R jets. The C/A jets are required to fulfil $|\eta| < 2.1$ and $p_T > 180$ GeV, and the anti- k_t jets must fulfil $|\eta| < 2.5$ and $p_T > 25$ GeV. All combinations of large- R C/A jets and small- R anti- k_t jets in each event are shown. The shared energy is normalized to the total energy of the small- R jet and this shared energy fraction is shown as a function of the angular separation ΔR of the small- R and large- R jets. The region of small angular separation is populated by combinations where a large fraction of the energy of the small- R jet is included in the large- R jet, i.e. where the two jets originate from the

same object. However, for larger values of ΔR , a significant fraction of the energy of the small- R jet can still be shared with the large- R jet.

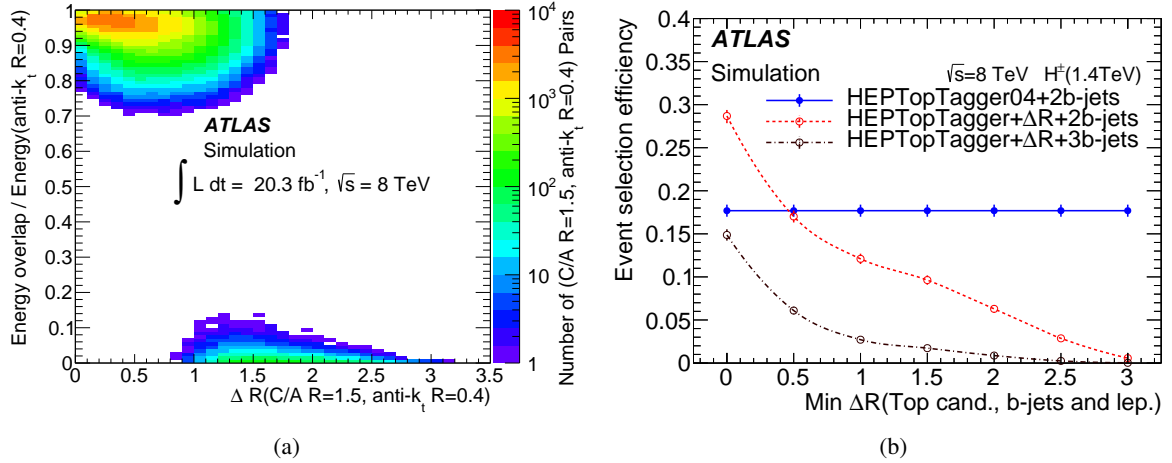


Figure 17: (a) Energy fraction of clusters included in anti- k_t jets with $R = 0.4$ also included in C/A jets with $R = 1.5$ in $t\bar{t}$ MC simulation as a function of the angular separation of the two jets. The C/A jets have to fulfil $|\eta| < 2.1$ and $p_T > 180$ GeV, and all combinations of large- R and small- R jets in each event are shown. (b) Efficiency for the H^+ selection for the HEPTopTagger04 method for a 1400 GeV H^+ signal (blue, full circles) and for HEPTopTagger for which an angular separation ΔR is required between the top-quark candidate and the closest anti- k_t $R = 0.4$ jet (or lepton) in the event (red open circles), HEPTopTagger+ ΔR . The efficiency of an alternative H^+ selection with three b -tagged anti- k_t $R = 0.4$ jets is shown in addition for HEPTopTagger+ ΔR . For HEPTopTagger+ ΔR , the efficiency is shown as a function of ΔR , while the HEPTopTagger04 algorithm is independent of ΔR .

The HEPTopTagger04 approach solves the issue of overlap between large- R and small- R jets by passing only the constituents of a set of small- R jets to the HEPTopTagger algorithm and by removing these small- R jets from the list of jets considered for the remaining event reconstruction, i.e. the identification of extra b -jets.

The charged-Higgs-boson process mentioned above is used to illustrate the advantage of the HEPTopTagger04 approach. A basic event selection for events with an H^+ boson is introduced in order to study the performance of the HEPTopTagger04 in this topology using simulated events only. It consists of the signal selection for $t\bar{t}$ events as detailed in Section 4.2.1 requiring at least one top-quark candidate reconstructed with the HEPTopTagger04 method and two b -tagged anti- k_t $R = 0.4$ jets not considered as part of the HEPTopTagger04 candidate (H^+ selection). The b -tagged anti- k_t $R = 0.4$ jets are allowed to be identical to the b -tagged jets required in the signal selection, if these jets are not part of the HEPTopTagger04 candidate.

The HEPTopTagger04 method is compared with HEPTopTagger+ ΔR in the H^+ selection. Only those b -tagged anti- k_t $R = 0.4$ jets that are more than ΔR away from the top-quark candidate are considered in the H^+ selection for HEPTopTagger+ ΔR . Moreover, the top-quark candidate is required to be separated from the reconstructed lepton by at least ΔR . Figure 17(b) shows the efficiency of the H^+ selection for a 1400 GeV H^+ signal MC sample for HEPTopTagger+ ΔR as a function of ΔR , and for the HEPTopTagger04 method, which is independent of ΔR . The HEPTopTagger04 leads to a higher efficiency than the simple HEPTopTagger+ ΔR benchmark for values of $\Delta R > 0.5$. In order to avoid energy sharing, larger values of ΔR would be appropriate (cf. Figure 17(a)). For small values of ΔR , HEPTopTagger+ ΔR shows a higher efficiency than the HEPTopTagger04 method, because at least one b -tagged jet largely overlaps

with the top-quark candidate and can be identified with the b -quark from the top-quark decay and not with one of the additional b -quarks from the $pp \rightarrow H^+ \bar{t}(b) \rightarrow t \bar{b} \bar{t}(b)$ process. An additional b -tagged anti- k_t $R = 0.4$ jet can be required in the event selection for HEPTopTagger+ ΔR to address this issue, which leads to a lower efficiency for HEPTopTagger+ ΔR than for the HEPTopTagger04 method for all values of ΔR .

In order to determine the optimal method for a particular application, mistag-rate comparisons of the two approaches are important to evaluate using the exact selection of that analysis due to the critical dependence on the dominant background composition and kinematic region.

8. Measurement of the top-tagging efficiency and mistag rate

In this section, the signal and background samples introduced in Sections 4.2.1 and 4.2.2 are used to study the top tagging efficiency and the mistag rate for the different top taggers introduced in Section 5.

8.1. Top-tagging efficiency

The large- R jets in the signal selection are identified with a high- p_T hadronically decaying top quark in lepton+jets $t\bar{t}$ events and are therefore used to measure the top-tagging efficiency in data as a function of the kinematic properties of the large- R jet (p_T , η). The tagging efficiency is given by the fraction of tagged large- R jets after background has been statistically subtracted using simulation. In each large- R jet p_T and η bin i , the efficiency is defined as

$$f_{\text{data},i} = \left(\frac{N_{\text{data}}^{\text{tag}} - N_{\bar{t}\bar{t} \text{ not matched}}^{\text{tag}} - N_{\text{non-}\bar{t}\bar{t}}^{\text{tag}}}{N_{\text{data}} - N_{\bar{t}\bar{t} \text{ not matched}} - N_{\text{non-}\bar{t}\bar{t}}}_i \right), \quad (6)$$

in which

- $N_{\text{data}}^{(\text{tag})}$ is the number of measured (tagged) large- R jets;
- $N_{\bar{t}\bar{t} \text{ not matched}}^{(\text{tag})}$ is the number of (tagged) not-matched large- R jets, i.e. jets not matched to a hadronically decaying top quark (cf. Section 4.2), according to the POWHEG+PYTHIA simulation;
- $N_{\text{non-}\bar{t}\bar{t}}^{(\text{tag})}$ is the number of (tagged) large- R jets predicted by simulation to arise from other background contributions, such as W +jets, Z +jets and single-top production.

Systematic uncertainties affecting the numerator and the denominator do not fully cancel in the ratio, because in particular the amount of not-matched $t\bar{t}$ production is much reduced after requiring a top-tagged jet, but before the top-tagging requirement the number of not-matched $t\bar{t}$ events is non-negligible.

The measurement is shown for p_T bins in which the relative statistical uncertainty of the efficiency is less than 30% and the relative systematic uncertainty is less than 65%. Two regions in large- R jet pseudorapidity are chosen, $|\eta| < 0.7$ and $0.7 < |\eta| < 2.0$, in which approximately equal numbers of events are expected.

The measured efficiency is compared to the efficiency in simulated $t\bar{t}$ events, which is defined as

$$f_{\text{MC},i} = \left(\frac{N_{\text{MC}}^{\text{tag}}}{N_{\text{MC}}}_i \right), \quad (7)$$

in which $N_{\text{MC}}^{(\text{tag})}$ is the number of (tagged) large- R jets in matched $t\bar{t}$ events which pass the signal selection.

8.1.1. Efficiency of the substructure-variable taggers

The measured and predicted top-tagging efficiencies for the top taggers I–V and the W' top tagger are studied as a function of the p_{T} of the trimmed anti- k_r $R = 1.0$ jet in the two pseudorapidity regions. In Figures 18 and 19, the efficiencies in the lower $|\eta|$ region are shown. The efficiencies of the different top taggers are similar in the two η regions, as seen in Figure 20, in which the efficiencies of tagger III and the W' top tagger in the higher $|\eta|$ region are shown.

When a large- R jet is considered matched according to the geometric matching of the jet axis to the direction of the top quark, this does not necessarily imply that all decay products of the top quark are contained inside the large- R jet. Even after subtracting the not-matched contribution in Eq. (6), a significant fraction of the large- R jets with lower p_{T} therefore do not contain all top-quark decay products. The tagging efficiency is high when all decay products are contained in the large- R jet. The efficiency is therefore low for large- R jets with small p_{T} and it rises with p_{T} because of the tighter collimation.

The efficiency decreases with increasing tagger number from tagger I to tagger V and the lowest efficiency of the tested taggers based on substructure variables is found for the W' top tagger. The efficiencies vary between 40% and 90%, depending on the tagger and the p_{T} of the large- R jet. The efficiencies are similar in the two η regions but the measurement is more precise for $|\eta| < 0.7$.

The measurement of the efficiency is limited by the systematic uncertainties resulting from the subtraction of background jets. The uncertainties in the measured efficiency include uncertainties related to the choice of generator used for $t\bar{t}$ production. In the lowest large- R jet p_{T} bin, the relative uncertainties of the efficiency for $|\eta| < 0.7$ are 10% to 14%, depending on the tagger, and for $0.7 < |\eta| < 2.0$ they vary between 11% and 17%. For $|\eta| < 0.7$, the systematic uncertainties in the interval 500 to 600 GeV vary between approximately 17% and 29%. For $0.7 < |\eta| < 2.0$ the uncertainties from 450 to 500 GeV are 18 to 26%. The systematic uncertainty is dominated by the different efficiencies from using POWHEG or MC@NLO for the generation of the $t\bar{t}$ contribution for $|\eta| < 0.7$. In the range $0.7 < |\eta| < 2.0$, the large- R JES, the PDF, the parton-shower and the ISR/FSR uncertainties also contribute significantly to the total systematic uncertainty.

Also shown in the figures is the prediction for f_{MC} obtained from the simulated POWHEG+PYTHIA $t\bar{t}$ events using the nominal simulation parameters and not considering systematic uncertainties. The prediction obtained in this way is consistent with the measured efficiency within the uncertainties of the measurement. In the simulation, for which the statistical uncertainty is much smaller than for the data, the efficiencies continue to rise with p_{T} , indicating that a plateau value is not reached in the p_{T} range studied here.

The ratio $f_{\text{data}}/f_{\text{MC}}$ is shown in the bottom panels of Figures 18–20. The nominal POWHEG+PYTHIA prediction is used for f_{MC} . For this ratio, the full systematic uncertainties of f_{MC} are considered, including the uncertainty from the choice of $t\bar{t}$ generator. The full correlation with the uncertainty of f_{data} is taken into account in the systematic uncertainty of the ratio. The ratio is consistent with unity within the uncertainty in all measured p_{T} and η ranges. For $|\eta| < 0.7$, the uncertainty of $f_{\text{data}}/f_{\text{MC}}$ is 8–16% (depending on the tagger) for large- R jet p_{T} from 350 to 400 GeV and 17–28% for 500–600 GeV. For $0.7 < |\eta| < 2.0$, the uncertainty is 10–19% for 350–400 GeV and 19–28% for 450–500 GeV.

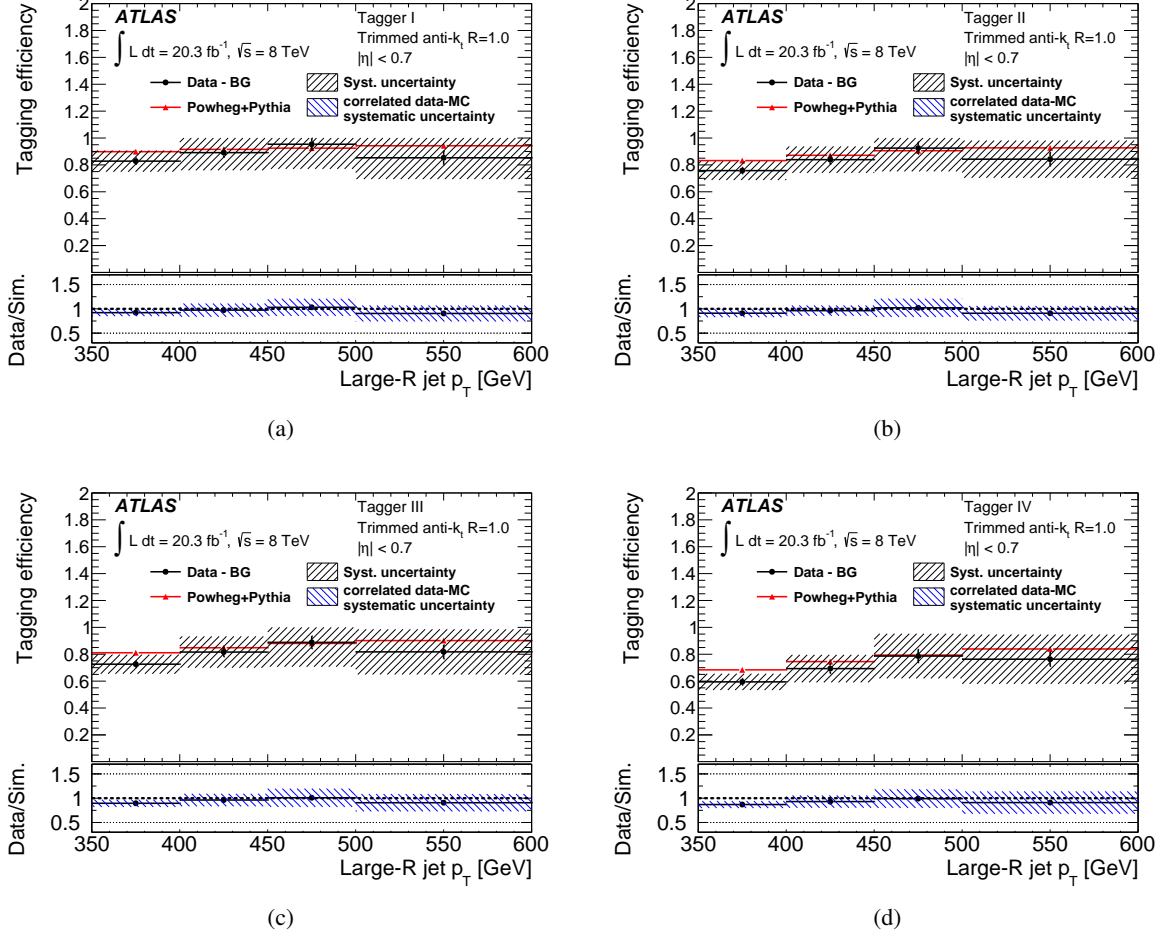


Figure 18: The efficiency f_{data} , as defined in Eq. (6), for tagging trimmed anti- k_t $R = 1.0$ jets with $|\eta| < 0.7$ with top taggers based on substructure variables (taggers I–IV) as a function of the large- R jet p_T . Background (BG) is statistically subtracted from the data using simulation. The vertical error bar indicates the statistical uncertainty of the efficiency measurement and the data uncertainty band shows the systematic uncertainties. Also shown is the predicted tagging efficiency f_{MC} , as defined in Eq. (7), from POWHEG+PYTHIA without systematic uncertainties. The ratio $f_{\text{data}}/f_{\text{MC}}$ of measured to predicted efficiency is shown at the bottom of each subfigure and the error bar gives the statistical uncertainty and the band the systematic uncertainty. The systematic uncertainty of the ratio is calculated taking into account the systematic uncertainties in the data and the prediction and their correlation.

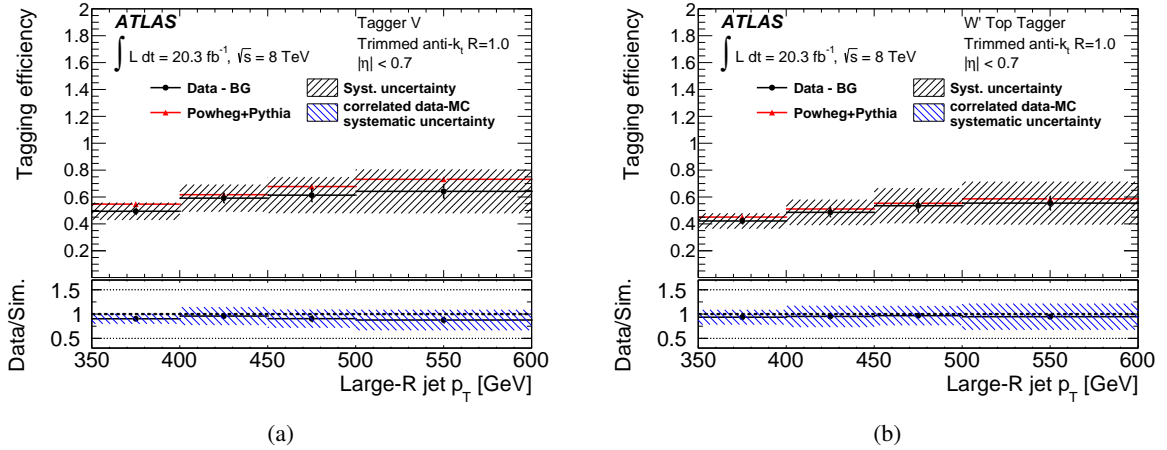


Figure 19: The efficiency f_{data} , as defined in Eq. (6), for tagging trimmed anti- k_t $R = 1.0$ jets with $|\eta| < 0.7$ with top taggers based on substructure variables (tagger V and W' top tagger) as a function of the large- R jet p_T . Background (BG) is statistically subtracted from the data using simulation. The vertical error bar indicates the statistical uncertainty of the efficiency measurement and the data uncertainty band shows the systematic uncertainties. Also shown is the predicted tagging efficiency f_{MC} , as defined in Eq. (7), from POWHEG+PYTHIA without systematic uncertainties. The ratio $f_{\text{data}}/f_{\text{MC}}$ of measured to predicted efficiency is shown at the bottom of each subfigure and the error bar gives the statistical uncertainty and the band the systematic uncertainty. The systematic uncertainty of the ratio is calculated taking into account the systematic uncertainties in the data and the prediction and their correlation.

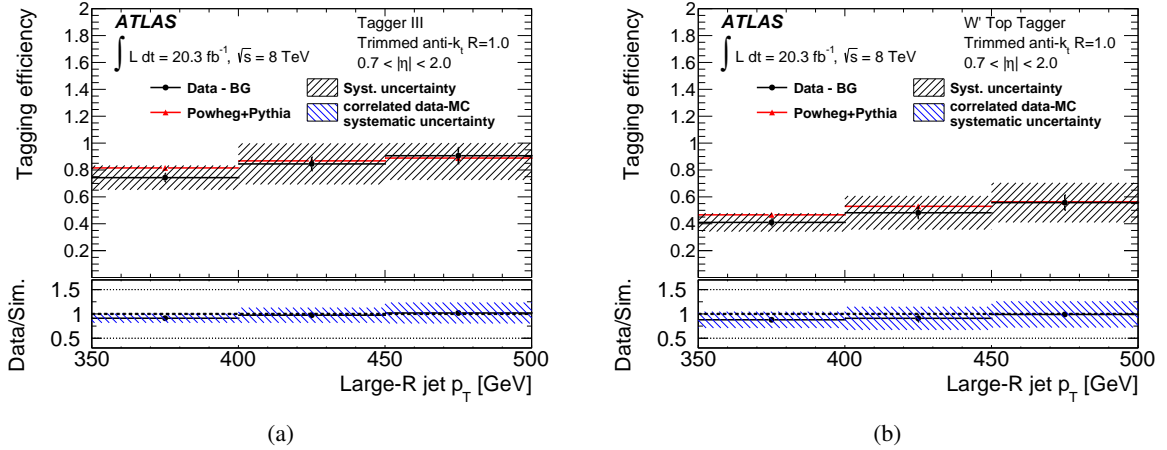


Figure 20: The efficiency f_{data} , as defined in Eq. (6), for tagging trimmed anti- k_t $R = 1.0$ jets with $0.7 < |\eta| < 2.0$ based on substructure variables (tagger III and W' top tagger) as a function of the large- R jet p_T . Background (BG) is statistically subtracted from the data using simulation. The vertical error bar indicates the statistical uncertainty of the efficiency measurement and the data uncertainty band shows the systematic uncertainties. Also shown is the predicted tagging efficiency f_{MC} , as defined in Eq. (7), from POWHEG+PYTHIA without systematic uncertainties. The ratio $f_{\text{data}}/f_{\text{MC}}$ of measured to predicted efficiency is shown at the bottom of each subfigure and the error bar gives the statistical uncertainty and the band the systematic uncertainty. The systematic uncertainty of the ratio is calculated taking into account the systematic uncertainties in the data and the prediction and their correlation.

8.1.2. Efficiency of Shower Deconstruction

The measurement of the efficiency for tagging anti- k_t $R = 1.0$ jets with SD, using the requirement $\ln(\chi) > 2.5$, is presented in Figure 21. The signal weights are calculated assuming that all top-quark decay products are included in the large- R jet. This containment assumption leads to a rising efficiency with top-quark p_T because of the tighter collimation at high p_T . The SD efficiency is approximately 30% in the region with the lowest p_T of the large- R jet (350–400 GeV), increases with p_T and reaches $\approx 45\%$ for 500–600 GeV in the lower $|\eta|$ range and for 450–500 GeV in the higher $|\eta|$ range. Within uncertainties, the measured efficiencies are compatible between the two η regions.

In the lowest measured p_T region, the relative uncertainty is $\approx 16\%$, with the largest contributions coming from the difference observed when changing the $t\bar{t}$ generator from POWHEG to MC@NLO (12%). The uncertainties in the subjet energy scale and resolution have a much smaller impact of 0.6% and 0.4%, respectively. For p_T between 500 and 600 GeV in the lower $|\eta|$ range, the relative uncertainty is $\approx 32\%$, with the largest contributions resulting from the generator choice (27%).

The efficiency from POWHEG+PYTHIA follows the trend of the measured efficiency and the predicted and measured efficiencies agree within uncertainties, but the predicted efficiency is systematically higher. The ratio $f_{\text{data}}/f_{\text{MC}}$ is approximately 80% throughout the considered p_T range. The relative uncertainty of the ratio is $\approx 25\%$ for $|\eta| < 0.7$. For $0.7 < |\eta| < 2.0$, the uncertainty varies between $\approx 25\%$ and $\approx 35\%$.

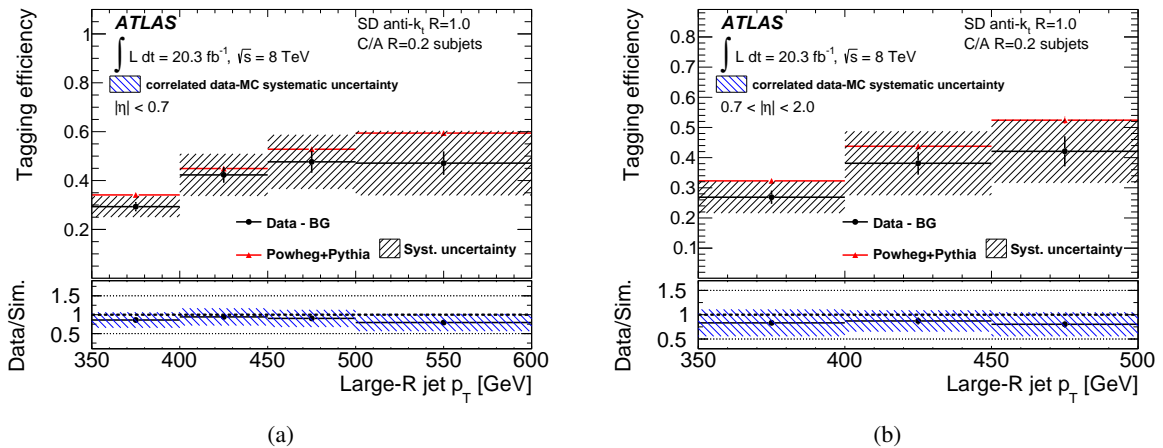


Figure 21: The efficiency f_{data} , as defined in Eq. (6), for tagging trimmed anti- k_t $R = 1.0$ jets with Shower Deconstruction, using the requirement $\ln(\chi) > 2.5$, as a function of the large- R jet p_T . The large- R jets are selected in the signal selection and have pseudorapidities (a) $|\eta| < 0.7$ and (b) $0.7 < |\eta| < 2.0$. Background (BG) is statistically subtracted from the data using simulation. The vertical error bar indicates the statistical uncertainty of the efficiency measurement and the data uncertainty band shows the systematic uncertainties. Also shown is the predicted tagging efficiency f_{MC} , as defined in Eq. (7), from POWHEG+PYTHIA without systematic uncertainties. The ratio $f_{\text{data}}/f_{\text{MC}}$ of measured to predicted efficiency is shown at the bottom of each subfigure and the error bar gives the statistical uncertainty and the band the systematic uncertainty. The systematic uncertainty of the ratio is calculated taking into account the systematic uncertainties in the data and the prediction and their correlation.

8.1.3. Efficiency of the HEPTopTagger

The efficiency for tagging C/A $R = 1.5$ jets with the HEPTopTagger is shown in Figure 22 as a function of the large- R jet p_T . In the lowest p_T interval from 200 to 250 GeV the efficiency is $\approx 10\%$. The efficiency increases with p_T because of the geometric collimation effect and reaches $\approx 40\%$ for p_T between 350 and 400 GeV and 45–50% for $p_T > 500$ GeV. The efficiencies in the two η regions are very similar. The measurement is systematically limited. In the lowest measured jet p_T interval from 200 to 250 GeV, the relative systematic uncertainty is 8.5% with similar contributions coming from several sources, the three largest ones being the difference between POWHEG and MC@NLO as the $t\bar{t}$ generator (3.9%), the large- R jet energy scale (3.3%), and the b -tagging efficiency (3.3%). The contributions from the imperfect knowledge of the subjet energy scale and resolution are 2.5% and 2.7%, respectively. For large- R jet p_T between 600 and 700 GeV, the relative uncertainty is 54%, and the largest contributions are from the generator choice (44%) and the large- R JES (22%), while the subjet energy scale (2.1%) and resolution (0.6%) have only a small impact.

When clustering objects (particles or clusters of calorimeter cells) with the C/A algorithm using $R = 1.5$ and comparing the resulting jet with the jet obtained by clustering the same particles with the anti- k_t algorithm using $R = 1.0$ and then trimming the anti- k_t jet, the p_T is larger for the C/A jet than for the trimmed anti- k_t jet. In this paper, the p_T interval 600–700 GeV for the C/A $R = 1.5$ jets corresponds approximately to the interval 500–600 GeV for the trimmed anti- k_t , $R = 1.0$ jets. Beyond this p_T , the statistical and systematic uncertainties become larger than 30% and 65%, respectively.

The efficiency predicted by the POWHEG+PYTHIA simulation agrees with the measurement within the uncertainties. The ratio $f_{\text{data}}/f_{\text{MC}}$ is consistent with unity, within uncertainties of $\approx 30\%$ in the lowest and highest measured p_T intervals and $\approx 15\%$ between 250 and 450 GeV.

The total systematic uncertainty of the efficiency measurements when integrating over the full p_T range and the range $0 < |\eta| < 2$ is given in Table 5. The total uncertainty is 12–20% for the substructure-variable-based taggers, 22% for SD, and 9.9% for the HEPTopTagger. The largest uncertainty results from the choice of $t\bar{t}$ generator for the subtraction of the not-matched $t\bar{t}$ contribution, which introduces a normalization uncertainty in the acceptance region of the measurement (high top-quark p_T), because the p_T -dependence of the cross section is different between POWHEG and MC@NLO. This difference is larger at high p_T , which translates to a larger uncertainty for the substructure-variable-based taggers and SD, which use trimmed anti- k_t $R = 1.0$ jets with $p_T > 350$ GeV, whereas the HEPTopTagger uses C/A $R = 1.5$ jets with $p_T > 200$ GeV. For the same reason, the uncertainties in the parton shower and the PDF have a larger impact for higher large- R jet p_T .

The large- R JES uncertainty affects the HEPTopTagger efficiency less strongly than the efficiencies of the other taggers (Table 5). This is due to the requirement placed on the top-quark-candidate transverse momentum ($p_T > 200$ GeV). The HEPTopTagger algorithm rejects some of the large- R jet constituents in the process of finding the hard substructure objects (mass-drop criterion) and when applying the filtering against underlying-event and pile-up contributions. The top-quark-candidate p_T is determined by the subjet four-momenta and is smaller than the large- R jet p_T , so that the requirement $p_{T(\text{top-quark candidate})} > 200$ GeV is stricter than the requirement $p_{T(\text{large-}R \text{ jet})} > 200$ GeV. This is also the reason why the subjet energy-scale uncertainty has a larger impact on the efficiency of the HEPTopTagger compared to SD, because for SD no p_T requirement on the top-quark candidate is included in the signal- and background-hypothesis weights.

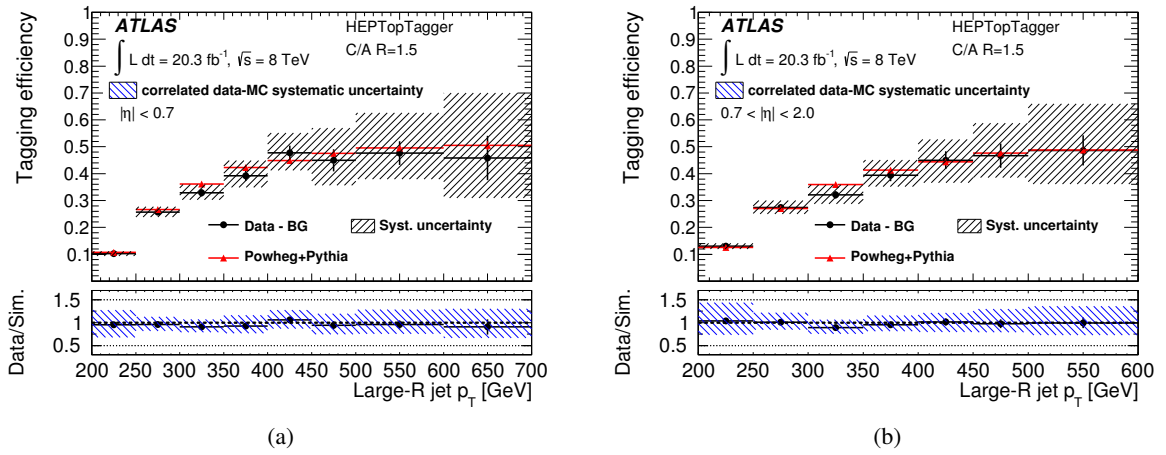


Figure 22: The efficiency f_{data} , as defined in Eq. (6), for tagging $C/A R = 1.5$ jets with the HEPTopTagger as a function of the large- R jet p_T . The large- R jets are selected in the signal selection and have pseudorapidities (a) $|\eta| < 0.7$ and (b) $0.7 < |\eta| < 2.0$. Background (BG) is statistically subtracted from the data using simulation. The vertical error bar indicates the statistical uncertainty of the efficiency measurement and the data uncertainty band shows the systematic uncertainties. Also shown is the predicted tagging efficiency f_{MC} , as defined in Eq. (7), from POWHEG+PYTHIA without systematic uncertainties. The ratio $f_{\text{data}}/f_{\text{MC}}$ of measured to predicted efficiency is shown at the bottom of each subfigure and the error bar gives the statistical uncertainty and the band the systematic uncertainty. The systematic uncertainty of the ratio is calculated taking into account the systematic uncertainties in the data and the prediction and their correlation.

Source	Relative uncertainty of top-tagging efficiency (%)							
	Tagger I	Tagger II	Tagger III	Tagger IV	Tagger V	W' Tagger	Shower Deconstruction	HEPTop-Tagger
Large- R jet energy scale	4.4	4.5	4.8	5.3	5.8	6.0	6.7	2.9
Large- R jet energy resolution	<0.1	0.1	0.1	0.2	0.2	0.3	0.8	1.5
Luminosity	1.0	1.0	1.1	1.2	1.3	1.4	1.5	1.3
b -tagging efficiency	2.7	2.6	2.9	3.1	3.5	3.7	3.9	3.5
Lepton reconstruction efficiency	0.5	0.5	0.5	0.6	0.7	0.8	0.8	2.0
$t\bar{t}$ cross section	1.9	1.8	1.9	2.1	2.4	2.6	2.6	2.0
$t\bar{t}$ ISR/FSR	1.4	1.3	1.4	0.5	1.6	1.6	2.2	3.2
$t\bar{t}$ generator	10	9.2	11	12	15	16	18	6.7
$t\bar{t}$ parton shower	4.8	4.1	4.6	4.8	4.6	5.1	5.1	1.7
$t\bar{t}$ PDF uncertainty	4.4	3.8	4.5	4.2	5.2	6.8	8.3	2.2
$t\bar{t}$ renormalization scale	0.8	0.8	0.8	0.9	1.0	1.1	1.0	0.6
Trimmed large- R jet mass scale	-	1.5	0.8	0.6	0.2	-	-	-
Trimmed large- R jet mass resolution	-	0.1	0.1	0.1	<0.1	-	-	-
$\sqrt{d_{12}}$	1.2	-	0.6	0.5	0.4	0.5	-	-
$\sqrt{d_{23}}$	-	-	-	0.7	1.1	-	-	-
τ_{21}	-	-	-	-	-	0.6	-	-
τ_{32}	-	-	-	-	-	1.4	-	-
Subjet energy scale	-	-	-	-	-	-	0.5	1.1
Subjet energy resolution	-	-	-	-	-	-	0.4	0.7
Total	13	12	14	15	18	20	22	9.9

Table 5: The relative uncertainty of the measured top-tagging efficiency (in percent) due to different sources of systematic uncertainty and the total systematic uncertainty obtained by adding the different contributions in quadrature.

8.2. Mistag rate

Large- R jets identified in the background selection are used to measure the top-tagging misidentification rate (mistag rate). In each large- R jet p_T bin i , the mistag rate is defined as

$$f_{\text{data},i}^{\text{mistag}} = \left(\frac{N_{\text{data}}^{\text{tag}}}{N_{\text{data}}} \right)_i, \quad (8)$$

with $N_{\text{data}}^{\text{(tag)}}$ the number of measured (tagged) large- R jets. The contamination from $t\bar{t}$ events is negligible before requiring a tagged top candidate. After requiring a HEPTopTagger-tagged top candidate, the average contamination is $\approx 3\%$ ($200 < p_T < 700$ GeV). It is smaller than 3% for $p_T < 350$ GeV. For larger values of p_T , however, the contamination from $t\bar{t}$ increases, as the large- R jet p_T spectrum falls more steeply for multijet production than for $t\bar{t}$ events, leading to a contamination of up to $\approx 5\%$ for $350 < p_T < 600$ GeV and $\approx 11\%$ for $600 < p_T < 700$ GeV.

For SD, the average contamination after requiring a tagged top candidate is $\approx 8\%$ ($350 < p_T < 700$ GeV). Although the HEPTopTagger gives higher background rejection than SD with $\ln(\chi) > 2.5$, the contamination for SD is larger on average, because the contamination increases with large- R jet p_T and the SD is only studied for trimmed anti- k_t $R = 1.0$ jets with $p_T > 350$ GeV. For the substructure-variable taggers, the average contamination is smaller than 1.6%. Hence only for the top taggers with high rejection, SD and the HEPTopTagger, the contribution from $t\bar{t}$ events is subtracted from the numerator of Eq. (8) before calculating the mistag rate. The systematic uncertainty of the $t\bar{t}$ contribution is estimated to be $\approx 50\%$ in each p_T interval. This uncertainty influences the measurement of the mistag rate by a negligible amount compared to the statistical uncertainty that results from the finite number of tagged large- R jets in data. Therefore, only the statistical uncertainty is reported.

The measured mistag rate is compared to the mistag rate observed in multijet events simulated with PYTHIA, which is defined as

$$f_{\text{MC},i}^{\text{mistag}} = \left(\frac{N_{\text{MC}}^{\text{tag}}}{N_{\text{MC}}} \right)_i, \quad (9)$$

in which $N_{\text{MC}}^{\text{(tag)}}$ is the number of (tagged) large- R jets which pass a looser background selection than required in data. The electron-trigger requirement, the minimum distance requirement between the electron-trigger object and the large- R jet, and the veto on reconstructed electrons are removed. Including these requirements for simulation reduces the event yield significantly, which leads to less predictive power for the mistag rate with the result that the simulation still describes the measured mistag rates, but with large statistical uncertainties.

Removing the requirements mentioned above from the background selection for the simulation is expected not to bias $f_{\text{MC},i}^{\text{mistag}}$. The low- p_T threshold of the electron trigger avoids biases towards dijet events with a well defined hard scattering axis, and a possible trigger bias is reduced by using only large- R jets away from the trigger object, i.e. jets with $\Delta R > 1.5$. The specific requirements applied only for data are therefore designed to allow for a measurement of the mistag rate in pure multijet events which avoids trigger biases and can hence be compared to the mistag rate observed in MC simulations.

The electron-trigger requirement is fulfilled preferentially for trigger objects with high p_T . The p_T of the electron-trigger object and that of the large- R jet under study for the mistag-rate determination are correlated through the common hard parton-parton scattering process. The large- R jet p_T spectrum is therefore different for events in which the electron-trigger combination is activated compared to those events in

which this trigger combination is inactive. As the trigger requirement is not applied in simulation, the average p_T of the large- R jets in simulation is observed to be lower than in data. The reconstructed MC p_T distribution of the large- R jets is therefore reweighted to the p_T distribution observed in data. This reweighting procedure has only a small impact on the mistag rate, which is measured in bins of large- R jet p_T .

8.2.1. Mistag rate for the substructure-variable taggers

The mistag rate $f_{\text{data}}^{\text{mistag}}$ is shown in Figures 23–24 for the different top taggers as a function of the large- R jet p_T . Anti- k_t $R = 1.0$ jets are used for SD. The mistag rates rise with the p_T of the large- R jet, because increased QCD radiation at higher p_T produces structures inside the jets that resemble the structures in top jets. For taggers with high efficiency a larger mistag rate is found than for those with lower efficiency, because these looser top-tagging criteria are met by a larger fraction of the background jets.

The mistag rate for trimmed anti- k_t $R = 1.0$ jets tagged using substructure-variable requirements are shown in Figure 23. In the lowest p_T interval from 350 to 400 GeV, the mistag rates for the taggers I–V and the W' top tagger are approximately 22%, 20%, 16%, 12%, 6%, and 4%, respectively. The measured mistag rate increases with p_T and reaches values between 24% and 36% for taggers I–IV in the p_T interval 600–700 GeV. In this highest p_T interval, the mistag rate is $\approx 16\%$ for tagger V and $\approx 6\%$ for the W' top tagger. The predicted mistag rate $f_{\text{MC}}^{\text{mistag}}$ from PYTHIA is also shown with an uncertainty band that includes systematic uncertainties due to the large- R JES and resolution uncertainties, and uncertainties of the modelling of the substructure variables. Within the uncertainties, the prediction from PYTHIA agrees with the measurement for all taggers. The uncertainties on the ratio $f_{\text{data}}/f_{\text{MC}}$ are 5–9% for taggers I–IV, and, depending on the large- R jet p_T , $\approx 10\%$ for tagger V and $\approx 20\%$ for the W' top tagger. The systematic uncertainties of tagger V and the W' top tagger are larger than for taggers I–IV because of the conservative treatment of the correlation between the variations of the different substructure variables as mentioned in Section 6.

8.2.2. Mistag rate for Shower Deconstruction

For SD, the mistag rate increases from 1% for p_T between 350 and 400 GeV to $\approx 4\%$ for 600–700 GeV. The prediction from PYTHIA shows the same trend as in data and agrees well with the measurement within relative systematic uncertainties between $\approx 40\%$ at low p_T and $\approx 13\%$ at high p_T , which result from the uncertainties in the energy scales and resolutions of the subjets and the large- R jets. Integrated over p_T , the subjet energy-scale and energy-resolution uncertainties lead to relative uncertainties of 15% and 13%, respectively, while the uncertainty in the large- R JES contributes 10%. The large- R jet energy-resolution uncertainty has a negligible impact ($< 1\%$).

8.2.3. Mistag rate for the HEPTopTagger

For the HEPTopTagger, the mistag rate increases from 0.5% for large- R jet p_T between 200 and 250 GeV to 3% for 450–500 GeV. Above 500 GeV, the statistical uncertainties of the measured rate become large. The PYTHIA simulation agrees well with the measurement. The systematic uncertainty of the simulation is given by uncertainties in the large- R JES and resolution, and the energy scale and resolution of the subjets. The relative systematic uncertainty decreases with p_T : it is 90% in the lowest measured p_T

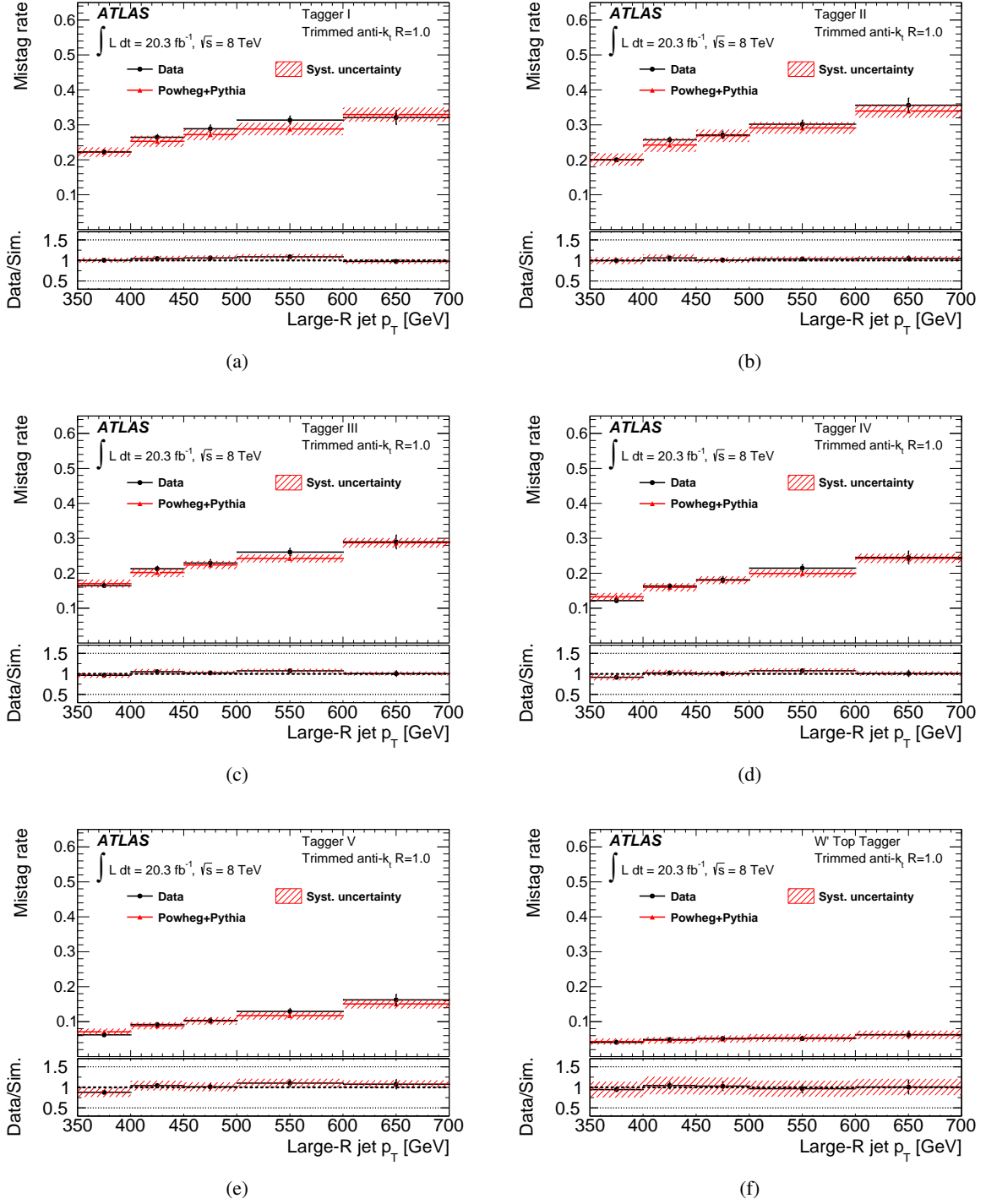


Figure 23: The mistag rate $f_{\text{data}}^{\text{mistag}}$, as defined in Eq. (8), for trimmed anti- k_t $R = 1.0$ jets as a function of the large- R jet p_T using the substructure-variable taggers I–V and the W' top tagger. The large- R jets are selected with the background selection and have pseudorapidities $|\eta| < 2.0$. The vertical error bar indicates the statistical uncertainty in the measurement of the mistag rate. Also shown is the predicted mistag rate $f_{\text{MC}}^{\text{mistag}}$, as defined in Eq. (9), from PYTHIA with systematic uncertainties included. The ratio of measured to predicted mistag rate is shown at the bottom of each subfigure and the error bar gives the statistical uncertainty of the measurement.

bin and 8% in the highest p_T bin. This behaviour is driven by the subject energy-resolution and energy-scale uncertainties, because at low large- R jet p_T a larger fraction of the HEPTopTagger subjects have momenta near the 20 GeV threshold. The mistag-rate uncertainty at low p_T is dominated by the subject energy-resolution uncertainty. The impact of the large- R jet uncertainties is significantly smaller.

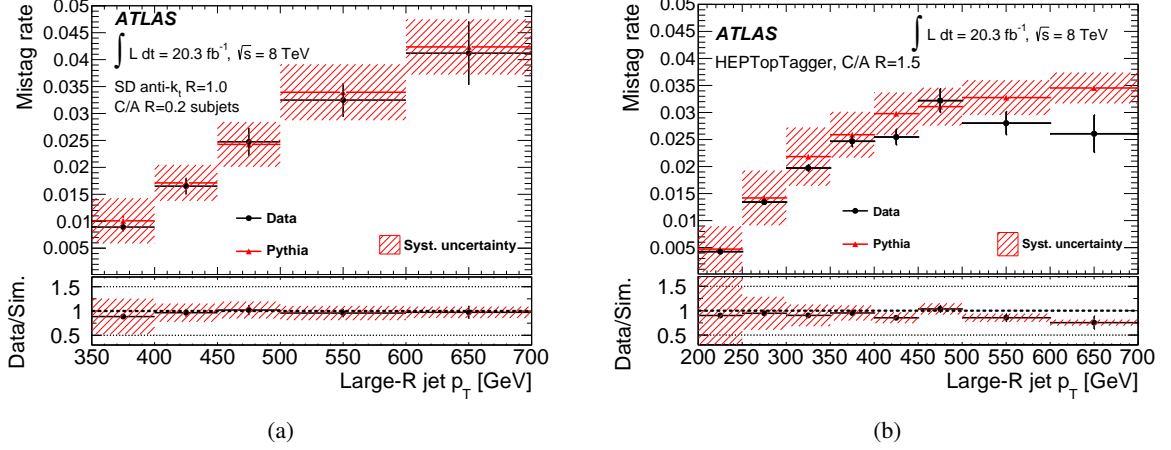


Figure 24: The mistag rate $f_{\text{data}}^{\text{mistag}}$, as defined in Eq. (8), for large- R jets with $|\eta| < 2.0$ selected with the background selection. (a) Mistag rate for anti- k_t $R = 1.0$ jets tagged with Shower Deconstruction using the requirement $\ln(\chi) > 2.5$ as a function of the trimmed jet p_T . (b) Mistag rate for C/A $R = 1.5$ jets tagged with the HEPTopTagger as a function of the jet p_T . The vertical error bar indicates the statistical uncertainty in the measurement of the mistag rate. Also shown is the predicted mistag rate $f_{\text{MC}}^{\text{mistag}}$, as defined in Eq. (9), from PYTHIA with systematic uncertainties included. The ratio of measured to predicted mistag rate is shown at the bottom of each subfigure and the error bar gives the statistical uncertainty of the measurement.

9. Summary and conclusions

Jet substructure techniques are used to identify high-transverse-momentum top quarks produced in proton–proton collisions at $\sqrt{s} = 8$ TeV at the LHC. The 2012 ATLAS dataset is used, corresponding to an integrated luminosity of $20.3 \pm 0.6 \text{ fb}^{-1}$.

Jets with a large radius parameter R are reconstructed and their substructure is analysed using a range of techniques that are sensitive to differences between hadronic top-quark decay and background processes. Jets are tagged as top jets by requirements imposed on the jet mass, splitting scales, and N -subjettiness, and by using the more elaborated algorithms of Shower Deconstruction (SD) and the original (not multivariate) HEPTopTagger. Six different combinations of requirements on substructure variables are investigated, five combinations denoted by taggers I–V and the W' top tagger. For these taggers and for Shower Deconstruction, trimmed anti- k_t $R = 1.0$ jets with $p_T > 350$ GeV are used. Cambridge/Aachen (C/A) $R = 0.2$ subjets with $p_T > 20$ GeV are used for SD. The HEPTopTagger was designed for, and is used with, ungroomed C/A $R = 1.5$ jets down to jet transverse momenta of 200 GeV. The difference in the jet algorithms, radii and grooming implies that the same top quark leads to a higher p_T for the C/A $R = 1.5$ jet. A variant of the HEPTopTagger algorithm is introduced, HEPTopTagger04, which operates on the constituents of a set of anti- k_t $R = 0.4$ jets instead of one C/A $R = 1.5$ jet. This technique is optimized to avoid energy overlap when different types of jets and jet radius parameters are used to reconstruct the full event final state. The advantage of this technique compared to a separation requirement applied to the C/A $R = 1.5$ jet is studied for simulated events with charged-Higgs-boson decays.

The performance of the various top-tagging techniques is compared using simulation by matching the different reconstructed jets to trimmed anti- k_t $R = 1.0$ jets formed at the particle level. The reciprocal of the mistag rate, the background rejection, is studied as a function of the efficiency in intervals of the particle-level jet transverse momentum, p_T^{true} , ranging from 350 to 1500 GeV, while the efficiency and rejection of the HEPTopTagger is also studied for $200 < p_T^{\text{true}} < 350$ GeV. For $350 < p_T^{\text{true}} < 1000$ GeV, SD offers the best rejection up to its maximum achievable efficiency. Top-tagging efficiencies above 70% can be achieved with cuts on substructure variables, for example, yielding rejections of approximately 3–6 for an efficiency of 80%. A rejection of ≈ 15 –20 at an efficiency of $\approx 50\%$ can be achieved with the W' top tagger over the range $450 < p_T^{\text{true}} < 1000$ GeV. For $1000 < p_T^{\text{true}} < 1500$ GeV, of all the top-tagging methods studied, the HEPTopTagger offers the best rejection (≈ 30) at an efficiency of $\approx 40\%$.

An event sample enriched in top-quark pairs is used to study the distributions of substructure variables. Simulations of Standard Model processes describe the relevant distributions well for the six substructure-variable taggers, SD, HEPTopTagger and HEPTopTagger04 within the uncertainties. The uncertainty in the energy scale of the subjets used by the HEPTopTagger is derived by comparing the mass of the top-quark candidate reconstructed in data and simulation. The relative subjet p_T uncertainty varies between 1% and 10%, depending on p_T and the functional form chosen to describe the p_T dependence.

The sample enriched in top-quark pairs is used to measure the efficiency to tag jets containing a hadronic top-quark decay. The efficiency is determined for jet p_T between 200 and 700 GeV for the C/A $R = 1.5$ jets and for 350–600 GeV for the trimmed anti- k_t $R = 1.0$ jets. The reach in p_T is limited by statistical and systematic uncertainties, which become large at high p_T . Jets not originating from hadronic top-quark decays are subtracted using simulation and the subtraction leads to systematic uncertainties in the measured efficiency. Integrated over the measured p_T range, the relative systematic uncertainty of the efficiency varies between $\approx 10\%$ and $\approx 20\%$ for the different substructure-variable-based taggers, and is $\approx 20\%$ for SD and $\approx 10\%$ for the HEPTopTagger. The dominant source of uncertainty is the modelling

of $t\bar{t}$ events, and increases with large- R jet p_T . The quoted p_T -integrated uncertainties are smaller for the HEPTopTagger efficiency, because the measurement extends to smaller large- R jet p_T . Simulated events generated with POWHEG+PYTHIA, with the h_{damp} parameter set to infinity and the $t\bar{t}$ and top-quark p_T spectra sequentially reweighted to describe the $t\bar{t}$ cross section measured at 7 TeV, describe the efficiency within the uncertainties of the measurement.

A sample enriched in multijet events is used to measure the mistag rate of the algorithms. The misidentification rate increases with the p_T of the large- R jet and, in the range of p_T studied, reaches values of 6–36% for the different substructure-variable taggers, $\approx 4\%$ for SD, and $\approx 3\%$ for the HEPTopTagger. The measured mistag rate is well described by simulations using PYTHIA within the modelling uncertainties and the statistical uncertainties of the measurement.

For top-tagging analyses with a low background level, e.g. $t\bar{t}$ resonance searches at top quark $p_T > 700$ GeV in the final state with one charged lepton, it is recommended to use a top tagger with high efficiency, such as the substructure-variable-based taggers I–IV studied in this paper. If high rejection is required, e.g. for an all-hadronic final state, then for $p_T > 1000$ GeV, one of the following taggers is likely to give the best sensitivity, depending on the details of the analysis: the W' top tagger, the HEPTopTagger, or SD. For p_T between 450 and 1000 GeV, SD is the tagger of choice if high rejection is required. Only the performance of the HEPTopTagger has been studied for p_T down to 200 GeV. In final states with high jet multiplicity where the full event needs to be reconstructed, the HEPTopTagger04 method is a useful approach to avoid energy sharing between small- R and large- R jets.

In analyses, the uncertainty in the top-tagging efficiency for Standard-Model and beyond-the-Standard-Model predictions comprises detector-related uncertainties and theoretical modelling uncertainties. The background in analyses should be determined by employing data-driven methods, as it was done for the ATLAS Run 1 analyses because the mistag rate was observed to depend strongly on the choice of trigger, and small deficiencies in the trigger simulation can have a large impact on the analysis.

The energy scale of the HEPTopTagger subjects should be determined using the in situ method pioneered in this paper. This method takes into account all subjects used by the HEPTopTagger, even those with radius parameter $R < 0.2$, for which the MC-based calibrations determined for $R = 0.2$ are used.

It is demonstrated in this paper that the substructure of top jets shows the expected features and that it is well modelled by simulations. Top tagging has been used in LHC Run 1 analyses and its importance will increase in Run 2 with more top quarks produced with high transverse momentum due to the higher centre-of-mass energy.

Acknowledgements

We thank CERN for the very successful operation of the LHC, as well as the support staff from our institutions without whom ATLAS could not be operated efficiently.

We acknowledge the support of ANPCyT, Argentina; YerPhI, Armenia; ARC, Australia; BMWFW and FWF, Austria; ANAS, Azerbaijan; SSTC, Belarus; CNPq and FAPESP, Brazil; NSERC, NRC and CFI, Canada; CERN; CONICYT, Chile; CAS, MOST and NSFC, China; COLCIENCIAS, Colombia; MSMT CR, MPO CR and VSC CR, Czech Republic; DNRF and DNSRC, Denmark; IN2P3-CNRS, CEA-DSM/IRFU, France; GNSF, Georgia; BMBF, HGF, and MPG, Germany; GSRT, Greece; RGC, Hong Kong SAR, China; ISF, I-CORE and Benoziyo Center, Israel; INFN, Italy; MEXT and JSPS, Japan;

CNRST, Morocco; FOM and NWO, Netherlands; RCN, Norway; MNiSW and NCN, Poland; FCT, Portugal; MNE/IFA, Romania; MES of Russia and NRC KI, Russian Federation; JINR; MESTD, Serbia; MSSR, Slovakia; ARRS and MIZŠ, Slovenia; DST/NRF, South Africa; MINECO, Spain; SRC and Wallenberg Foundation, Sweden; SERI, SNSF and Cantons of Bern and Geneva, Switzerland; MOST, Taiwan; TAEK, Turkey; STFC, United Kingdom; DOE and NSF, United States of America. In addition, individual groups and members have received support from BCKDF, the Canada Council, CANARIE, CRC, Compute Canada, FQRNT, and the Ontario Innovation Trust, Canada; EPLANET, ERC, FP7, Horizon 2020 and Marie Skłodowska-Curie Actions, European Union; Investissements d’Avenir Labex and Idex, ANR, Région Auvergne and Fondation Partager le Savoir, France; DFG and AvH Foundation, Germany; Herakleitos, Thales and Aristeia programmes co-financed by EU-ESF and the Greek NSRF; BSF, GIF and Minerva, Israel; BRF, Norway; Generalitat de Catalunya, Generalitat Valenciana, Spain; the Royal Society and Leverhulme Trust, United Kingdom.

The crucial computing support from all WLCG partners is acknowledged gratefully, in particular from CERN and the ATLAS Tier-1 facilities at TRIUMF (Canada), NDGF (Denmark, Norway, Sweden), CC-IN2P3 (France), KIT/GridKA (Germany), INFN-CNAF (Italy), NL-T1 (Netherlands), PIC (Spain), ASGC (Taiwan), RAL (UK) and BNL (USA) and in the Tier-2 facilities worldwide.

Appendix

A. Additional distributions for the signal-sample selection

In this appendix, additional event-level distributions after the signal-sample selections (Section 4.2.1) are shown, which complement Figures 1 and 2.

Distributions for the signal selection with at least one trimmed anti- k_t $R = 1.0$ jet with $p_T > 350$ GeV are shown in Figure 25. The lepton transverse momentum (Figure 25(a)) exhibits a falling spectrum for $p_T > 50$ GeV. The reduced number of entries in the bin from 25 to 45 GeV is due to the fact that the combination of the lepton triggers is not fully efficient below 50 GeV. The distribution is well described by simulations of SM processes within the uncertainties. The distribution of the distance ΔR between the highest- p_T trimmed anti- k_t $R = 1.0$ jet and the highest- p_T b -jet within $\Delta R = 1.5$ of the lepton is presented in Figure 25(b) and shows that the large- R jet and the b -jet are well separated.

The dominant systematic uncertainties in Figure 25 result from uncertainties in the large- R jet energy scale, the PDF, and the $t\bar{t}$ generator. The contributions from these sources are approximately equal in size and they affect mostly the normalization of the distributions.

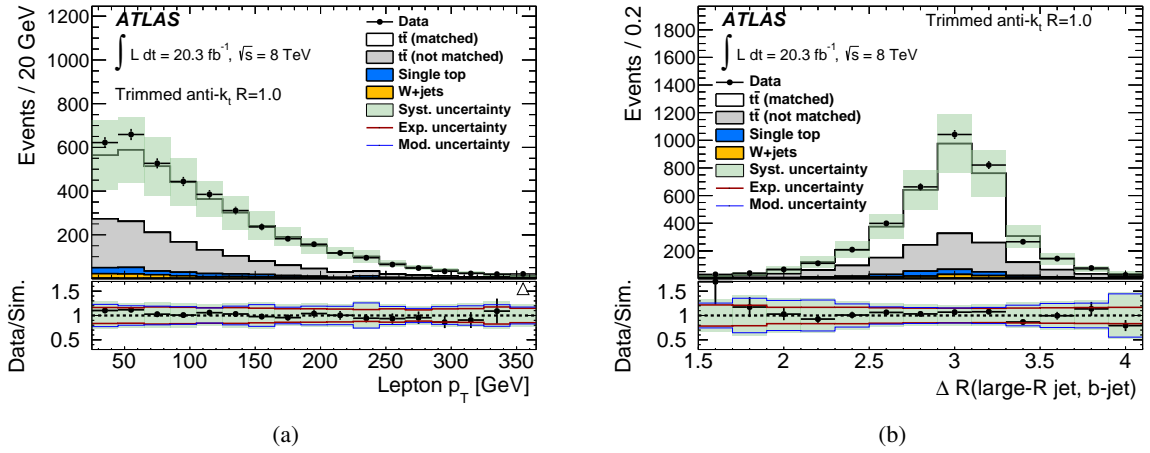


Figure 25: Detector-level distributions of variables reconstructed in events passing the signal-sample selection ($t\bar{t}$) with at least one trimmed anti- k_t $R = 1.0$ jet with $p_T > 350$ GeV. (a) The transverse momentum of the charged lepton and (b) the distance in (η, ϕ) between the highest- p_T b -jet within $\Delta R = 1.5$ of the lepton and the highest- p_T trimmed anti- k_t $R = 1.0$ jet. The vertical error bar indicates the statistical uncertainty of the measurement. Also shown are distributions for simulated SM contributions with systematic uncertainties (described in Section 6) indicated as a band. The $t\bar{t}$ prediction is split into a *matched* part for which the large- R jet axis is within $\Delta R = 0.75$ of the flight direction of a hadronically decaying top quark and a *not matched* part for which this criterion does not hold. The ratio of measurement to prediction is shown at the bottom of each subfigure and the error bar and band give the statistical and systematic uncertainties of the ratio, respectively. The impacts of experimental and $t\bar{t}$ modelling uncertainties are shown separately for the ratio.

Distributions for events fulfilling the signal selection with at least one C/A $R = 1.5$ jet with $p_T > 200$ GeV, as used in the HEPTopTagger studies, are shown in Figure 26. The distribution of the transverse mass m_T^W is shown in Figure 26(a). It exhibits a peak near the W -boson mass, which is expected if the

reconstructed charged lepton and the E_T^{miss} correspond to the charged lepton and neutrino from the W decay and the momenta of the two particles lie in the transverse plane. The missing-transverse-momentum distribution (Figure 26(b)) displays a peak around 55 GeV and a smoothly falling spectrum for larger values.

All distributions are described by the simulation within the uncertainties. Important sources of systematic uncertainty for the m_T^W and E_T^{miss} distributions are the large- R JES, the b -tagging efficiency, the prediction of the $t\bar{t}$ cross section, and $t\bar{t}$ modelling uncertainties from the choice of generator, parton shower, and PDF set. None of these uncertainties dominates.

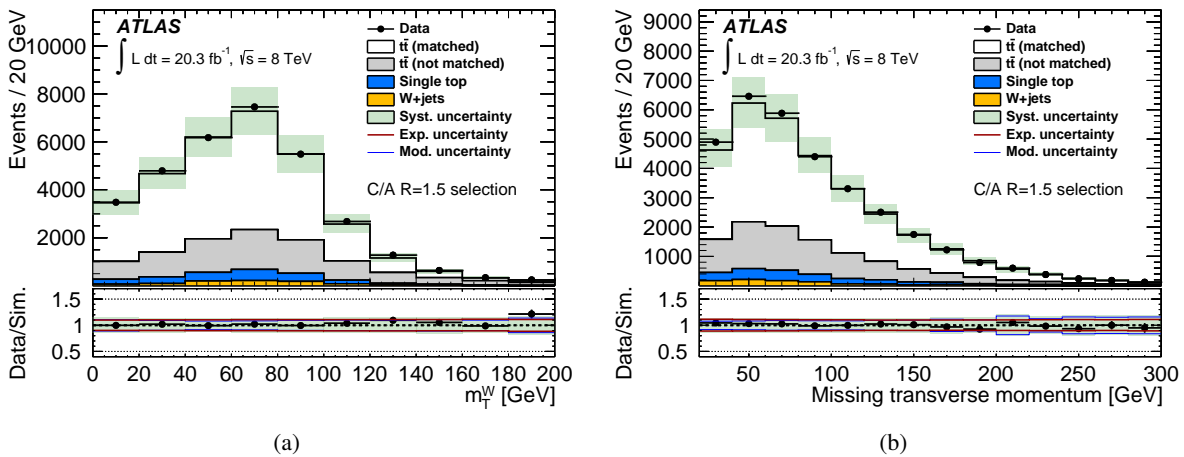


Figure 26: Detector-level distributions of (a) the transverse mass m_T^W and (b) the missing transverse momentum E_T^{miss} for events passing the signal selection with at least one $C/A R = 1.5$ jet with $p_T > 200$ GeV. The vertical error bar indicates the statistical uncertainty of the measurement. Also shown are distributions for simulated SM contributions with systematic uncertainties (described in Section 6) indicated as a band. The $t\bar{t}$ prediction is split into a *matched* part for which the large- R jet axis is within $\Delta R = 1.0$ of the flight direction of a hadronically decaying top quark and a *not matched* part for which this criterion does not hold. The ratio of measurement to prediction is shown at the bottom of each subfigure and the error bar and band give the statistical and systematic uncertainties of the ratio, respectively. The impacts of experimental and $t\bar{t}$ modelling uncertainties are shown separately for the ratio.

References

- [1] ATLAS Collaboration, *Search for resonances decaying into top-quark pairs using fully hadronic decays in pp collisions with ATLAS at $\sqrt{s} = 7$ TeV*, *JHEP* **1301** (2013) 116, arXiv:1211.2202 [hep-ex].
- [2] ATLAS Collaboration, *Search for $W' \rightarrow tb \rightarrow q\bar{q}b\bar{b}$ decays in pp collisions at $\sqrt{s} = 8$ TeV with the ATLAS detector*, *Eur. Phys. J.* **C75** (2015) 165, arXiv:1408.0886 [hep-ex].
- [3] ATLAS Collaboration, *A search for $t\bar{t}$ resonances using lepton-plus-jets events in proton-proton collisions at $\sqrt{s} = 8$ TeV with the ATLAS detector*, *JHEP* **1508** (2015) 148, arXiv:1505.07018 [hep-ex].

- [4] ATLAS Collaboration, *ATLAS Run 1 searches for direct pair production of third-generation squarks at the Large Hadron Collider*, *Eur. Phys. J.* **C75** (2015) 510, arXiv:1506.08616 [hep-ex].
- [5] ATLAS Collaboration, *Measurement of the differential cross-section of highly boosted top quarks as a function of their transverse momentum in $\sqrt{s} = 8$ TeV proton-proton collisions using the ATLAS detector*, *Phys. Rev.* **D93** (2016) 032009, arXiv:1510.03818 [hep-ex].
- [6] ATLAS Collaboration, *Measurement of the charge asymmetry in highly boosted top-quark pair production in $\sqrt{s} = 8$ TeV pp collision data collected by the ATLAS experiment*, *Phys. Lett.* **B756** (2016) 52–71, arXiv:1512.06092 [hep-ex].
- [7] CMS Collaboration, *Search for Top-Quark Partners with Charge 5/3 in the Same-Sign Dilepton Final State*, *Phys. Rev. Lett.* **112** (2014) 171801, arXiv:1312.2391 [hep-ex].
- [8] CMS Collaboration, *Searches for third generation squark production in fully hadronic final states in proton-proton collisions at $\sqrt{s} = 8$ TeV*, *JHEP* **1506** (2015) 116, arXiv:1503.08037 [hep-ex].
- [9] CMS Collaboration, *Search for resonant $t\bar{t}$ production in proton-proton collisions at $\sqrt{s} = 8$ TeV*, *Phys. Rev.* **D93** (2016) 012001, arXiv:1506.03062 [hep-ex].
- [10] CMS Collaboration, *Search for vector-like charge 2/3 T quarks in proton-proton collisions at $\sqrt{s} = 8$ TeV*, *Phys. Rev.* **D93** (2016) 012003, arXiv:1509.04177 [hep-ex].
- [11] CMS Collaboration, *Search for $W' \rightarrow tb$ in proton-proton collisions at $\sqrt{s} = 8$ TeV*, *JHEP* **1602** (2016) 122, arXiv:1509.06051 [hep-ex].
- [12] CMS Collaboration, *Search for the production of an excited bottom quark decaying to tW in proton-proton collisions at $\sqrt{s} = 8$ TeV*, *JHEP* **1601** (2016) 166, arXiv:1509.08141 [hep-ex].
- [13] CMS Collaboration, *Search for direct pair production of supersymmetric top quarks decaying to all-hadronic final states in pp collisions at $\sqrt{s} = 8$ TeV*, (2016), submitted to *Eur. Phys. J. C*, arXiv:1603.00765 [hep-ex].
- [14] J. M. Butterworth et al., *Jet Substructure as a New Higgs-Search Channel at the Large Hadron Collider*, *Phys. Rev. Lett.* **100** (2008) 242001, arXiv:0802.2470 [hep-ph].
- [15] S. D. Ellis, C. K. Vermilion and J. R. Walsh, *Techniques for improved heavy particle searches with jet substructure*, *Phys. Rev.* **D80** (2009) 051501, arXiv:0903.5081 [hep-ph].
- [16] D. Krohn, J. Thaler and L.-T. Wang, *Jet Trimming*, *JHEP* **1002** (2010) 084, arXiv:0912.1342 [hep-ph].
- [17] ATLAS Collaboration, *Search for $t\bar{t}$ resonances in the lepton plus jets final state with ATLAS using 4.7 fb^{-1} of pp collisions at $\sqrt{s} = 7$ TeV*, *Phys. Rev.* **D88** (2013) 012004, arXiv:1305.2756 [hep-ex].
- [18] ATLAS Collaboration, *Performance of jet substructure techniques for large-R jets in proton-proton collisions at $\sqrt{s} = 7$ TeV using the ATLAS detector*, *JHEP* **1309** (2013) 076, arXiv:1306.4945 [hep-ex].

- [19] D. E. Soper and M. Spannowsky, *Finding physics signals with shower deconstruction*, *Phys. Rev.* **D84** (2011) 074002, arXiv:1102.3480 [hep-ph].
- [20] D. E. Soper and M. Spannowsky, *Finding top quarks with shower deconstruction*, *Phys. Rev.* **D87** (2013) 054012, arXiv:1211.3140 [hep-ph].
- [21] T. Plehn, G. P. Salam and M. Spannowsky, *Fat Jets for a Light Higgs Boson*, *Phys. Rev. Lett.* **104** (2010) 111801, arXiv:0910.5472 [hep-ph].
- [22] T. Plehn et al., *Stop reconstruction with tagged tops*, *JHEP* **1010** (2010) 078, arXiv:1006.2833 [hep-ph].
- [23] ATLAS Collaboration, *Performance of the ATLAS Trigger System in 2010*, *Eur. Phys. J.* **C72** (2012) 1849, arXiv:1110.1530 [hep-ex].
- [24] ATLAS Collaboration, *The ATLAS Experiment at the CERN Large Hadron Collider*, *JINST* **3** (2008) S08003.
- [25] S. Frixione, P. Nason and G. Ridolfi, *A positive-weight next-to-leading-order Monte Carlo for heavy flavour hadroproduction*, *JHEP* **0709** (2007) 126, arXiv:0707.3088 [hep-ph].
- [26] P. Nason, *A new method for combining NLO QCD with shower Monte Carlo algorithms*, *JHEP* **0411** (2004) 040, arXiv:hep-ph/0409146 [hep-ph].
- [27] S. Frixione, P. Nason and C. Oleari, *Matching NLO QCD computations with parton shower simulations: the POWHEG method*, *JHEP* **0711** (2007) 070, arXiv:0709.2092 [hep-ph].
- [28] S. Alioli et al., *A general framework for implementing NLO calculations in shower Monte Carlo programs: the POWHEG BOX*, *JHEP* **1006** (2010) 043, arXiv:1002.2581 [hep-ph].
- [29] T. Sjöstrand, S. Mrenna and P. Z. Skands, *PYTHIA 6.4 physics and manual*, *JHEP* **0605** (2006) 026, arXiv:hep-ph/0603175 [hep-ph].
- [30] P. Z. Skands, *Tuning Monte Carlo generators: The Perugia tunes*, *Phys. Rev.* **D82** (2010) 074018, arXiv:1005.3457 [hep-ph].
- [31] H.-L. Lai et al., *New parton distributions for collider physics*, *Phys. Rev.* **D82** (2010) 074024, arXiv:1007.2241 [hep-ph].
- [32] S. Frixione and B. R. Webber, *Matching NLO QCD computations and parton shower simulations*, *JHEP* **0206** (2002) 029, arXiv:hep-ph/0204244 [hep-ph].
- [33] S. Frixione, P. Nason and B. R. Webber, *Matching NLO QCD and parton showers in heavy flavor production*, *JHEP* **0308** (2003) 007, arXiv:hep-ph/0305252 [hep-ph].
- [34] G. Corcella et al., *HERWIG 6: an event generator for hadron emission reactions with interfering gluons (including supersymmetric processes)*, *JHEP* **0101** (2001) 010, arXiv:hep-ph/0011363 [hep-ph].
- [35] J. M. Butterworth, J. R. Forshaw and M. H. Seymour, *Multiparton interactions in photoproduction at HERA*, *Z. Phys.* **C72** (1996) 637, arXiv:hep-ph/9601371 [hep-ph].
- [36] ATLAS Collaboration, *New ATLAS event generator tunes to 2010 data*, (2011), URL: <http://cds.cern.ch/record/1345343>.

- [37] B. P. Kersevan and E. Richter-Was, *The Monte Carlo event generator AcerMC versions 2.0 to 3.8 with interfaces to PYTHIA 6.4, HERWIG 6.5 and ARIADNE 4.1*, *Comput. Phys. Commun.* **184** (2013) 919, arXiv:[hep-ph/0405247](#) [[hep-ph](#)].
- [38] J. Pumplin et al., *New generation of parton distributions with uncertainties from global QCD analysis*, *JHEP* **0207** (2002) 012, arXiv:[hep-ph/0201195](#) [[hep-ph](#)].
- [39] ATLAS Collaboration, *Measurement of $t\bar{t}$ production with a veto on additional central jet activity in pp collisions at $\sqrt{s} = 7$ TeV using the ATLAS detector*, *Eur. Phys. J.* **C72** (2012) 2043, arXiv:[1203.5015](#) [[hep-ex](#)].
- [40] F. Aaron et al., *Combined measurement and QCD analysis of the inclusive $e^\pm p$ scattering cross sections at HERA*, *JHEP* **1001** (2010) 109, arXiv:[0911.0884](#) [[hep-ex](#)].
- [41] M. Cacciari et al., *Top-pair production at hadron colliders with next-to-next-to-leading logarithmic soft-gluon resummation*, *Phys. Lett.* **B710** (2012) 612, arXiv:[1111.5869](#) [[hep-ph](#)].
- [42] M. Beneke et al., *Hadronic top-quark pair production with NNLL threshold resummation*, *Nucl. Phys.* **B855** (2012) 695, arXiv:[1109.1536](#) [[hep-ph](#)].
- [43] P. Bärnreuther, M. Czakon and A. Mitov, *Percent-Level-Precision Physics at the Tevatron: Next-to-Next-to-Leading Order QCD Corrections to $q\bar{q} \rightarrow t\bar{t} + X$* , *Phys. Rev. Lett.* **109** (2012) 132001, arXiv:[1204.5201](#) [[hep-ph](#)].
- [44] M. Czakon and A. Mitov, *NNLO corrections to top-pair production at hadron colliders: the all-fermionic scattering channels*, *JHEP* **1212** (2012) 054, arXiv:[1207.0236](#) [[hep-ph](#)].
- [45] M. Czakon and A. Mitov, *NNLO corrections to top pair production at hadron colliders: the quark-gluon reaction*, *JHEP* **1301** (2013) 080, arXiv:[1210.6832](#) [[hep-ph](#)].
- [46] M. Czakon, P. Fiedler and A. Mitov, *Total Top-Quark Pair-Production Cross Section at Hadron Colliders Through $O(\alpha_s^4)$* , *Phys. Rev. Lett.* **110** (2013) 252004, arXiv:[1303.6254](#) [[hep-ph](#)].
- [47] M. Czakon and A. Mitov, *Top++: A program for the calculation of the top-pair cross-section at hadron colliders*, *Comput. Phys. Commun.* **185** (2014) 2930, arXiv:[1112.5675](#) [[hep-ph](#)].
- [48] M. Botje et al., *The PDF4LHC Working Group Interim Recommendations*, (2011), arXiv:[1101.0538](#) [[hep-ph](#)].
- [49] A. Martin et al., *Parton distributions for the LHC*, *Eur. Phys. J.* **C63** (2009) 189, arXiv:[0901.0002](#) [[hep-ph](#)].
- [50] A. Martin et al., *Uncertainties on α_s in global PDF analyses and implications for predicted hadronic cross sections*, *Eur. Phys. J.* **C64** (2009) 653, arXiv:[0905.3531](#) [[hep-ph](#)].
- [51] J. Gao et al., *CT10 next-to-next-to-leading order global analysis of QCD*, *Phys. Rev.* **D89** (2014) 033009, arXiv:[1302.6246](#) [[hep-ph](#)].
- [52] R. D. Ball et al., *Parton distributions with LHC data*, *Nucl. Phys.* **B867** (2013) 244, arXiv:[1207.1303](#) [[hep-ph](#)].
- [53] M. Aliev et al., *HATHOR: HAdronic Top and Heavy quarks crOss section calculatoR*, *Comput. Phys. Commun.* **182** (2011) 1034, arXiv:[1007.1327](#) [[hep-ph](#)].

- [54] ATLAS Collaboration, *Measurements of normalized differential cross sections for $t\bar{t}$ production in pp collisions at $\sqrt{s} = 7$ TeV using the ATLAS detector*, *Phys. Rev.* **D90** (2014) 072004, arXiv:1407.0371 [hep-ex].
- [55] ATLAS Collaboration, *Search for the Standard Model Higgs boson produced in association with top quarks and decaying into $b\bar{b}$ in pp collisions at $\sqrt{s} = 8$ TeV with the ATLAS detector*, *Eur. Phys. J.* **C75** (2015) 349, arXiv:1503.05066 [hep-ex].
- [56] S. Frixione et al., *Single-top hadroproduction in association with a W boson*, *JHEP* **0807** (2008) 029, arXiv:0805.3067 [hep-ph].
- [57] N. Kidonakis, *Next-to-next-to-leading logarithm resummation for s -channel single top quark production*, *Phys. Rev.* **D81** (2010) 054028, arXiv:1001.5034 [hep-ph].
- [58] N. Kidonakis, *Next-to-next-to-leading-order collinear and soft gluon corrections for t -channel single top quark production*, *Phys. Rev.* **D83** (2011) 091503, arXiv:1103.2792 [hep-ph].
- [59] N. Kidonakis, *Two-loop soft anomalous dimensions for single top quark associated production with a W^- or H^-* , *Phys. Rev.* **D82** (2010) 054018, arXiv:1005.4451 [hep-ph].
- [60] M. L. Mangano et al., *ALPGEN, a generator for hard multiparton processes in hadronic collisions*, *JHEP* **0307** (2003) 001, arXiv:hep-ph/0206293 [hep-ph].
- [61] ATLAS Collaboration, *Measurement of the charge asymmetry in top quark pair production in pp collisions at $\sqrt{s} = 7$ TeV using the ATLAS detector*, *Eur. Phys. J.* **C72** (2012) 2039, arXiv:1203.4211 [hep-ex].
- [62] ATLAS Collaboration, *Measurements of top quark pair relative differential cross-sections with ATLAS in pp collisions at $\sqrt{s} = 7$ TeV*, *Eur. Phys. J.* **C73** (2013) 2261, arXiv:1207.5644 [hep-ex].
- [63] R. Gavin et al., *W physics at the LHC with FEWZ 2.1*, *Comput. Phys. Commun.* **184** (2013) 208, arXiv:1201.5896 [hep-ph].
- [64] R. M. Harris, C. T. Hill and S. J. Parke, *Cross Section for Topcolor Z'_1 decaying to $t\bar{t}$: Version 2.6*, (1999), arXiv:hep-ph/9911288 [hep-ph].
- [65] G. Branco et al., *Theory and phenomenology of two-Higgs-doublet models*, *Phys. Rept.* **516** (2012) 1, arXiv:1106.0034 [hep-ph].
- [66] ATLAS Collaboration, *The ATLAS Simulation Infrastructure*, *Eur. Phys. J.* **C70** (2010) 823, arXiv:1005.4568 [physics.ins-det].
- [67] S. Agostinelli et al., *GEANT4—a simulation toolkit*, *Nucl. Instrum. Meth.* **A506** (2003) 250.
- [68] ATLAS Collaboration, *The simulation principle and performance of the ATLAS fast calorimeter simulation FastCaloSim*, (2010), URL: <http://cds.cern.ch/record/1300517>.
- [69] T. Sjöstrand, S. Mrenna and P. Z. Skands, *A brief introduction to PYTHIA 8.1*, *Comput. Phys. Commun.* **178** (2008) 852, arXiv:0710.3820 [hep-ph].
- [70] ATLAS Collaboration, *Electron reconstruction and identification efficiency measurements with the ATLAS detector using the 2011 LHC proton-proton collision data*, *Eur. Phys. J.* **C74** (2014) 2941, arXiv:1404.2240 [hep-ex].

- [71] ATLAS Collaboration, *Electron efficiency measurements with the ATLAS detector using the 2012 LHC proton–proton collision data*, (2014), URL: <http://cdsweb.cern.ch/record/1706245>.
- [72] ATLAS Collaboration, *Performance of primary vertex reconstruction in proton-proton collisions at $\sqrt{s} = 7$ TeV in the ATLAS experiment*, (2010), URL: <http://cds.cern.ch/record/1281344>.
- [73] K. Rehermann and B. Tweedie, *Efficient identification of boosted semileptonic top quarks at the LHC*, *JHEP* **1103** (2011) 059, arXiv:1007.2221 [hep-ph].
- [74] ATLAS Collaboration, *Measurement of the muon reconstruction performance of the ATLAS detector using 2011 and 2012 LHC proton–proton collision data*, *Eur. Phys. J.* **C74** (2014) 3130, arXiv:1407.3935 [hep-ex].
- [75] M. Cacciari, G. P. Salam and G. Soyez, *FastJet User Manual*, *Eur. Phys. J.* **C72** (2012) 1896, arXiv:1111.6097 [hep-ph].
- [76] ATLAS Collaboration, *Jet energy measurement with the ATLAS detector in proton-proton collisions at $\sqrt{s} = 7$ TeV*, *Eur. Phys. J.* **C73** (2013) 2304, arXiv:1112.6426 [hep-ex].
- [77] C. Issever, K. Borras and D. Wegener, *An improved weighting algorithm to achieve software compensation in a fine grained LAr calorimeter*, *Nucl. Instrum. Meth.* **A545** (2005) 803, arXiv:physics/0408129 [physics.ins-det].
- [78] ATLAS Collaboration, *Jet energy measurement and its systematic uncertainty in proton-proton collisions at $\sqrt{s} = 7$ TeV with the ATLAS detector*, *Eur. Phys. J.* **C75** (2015) 17, arXiv:1406.0076 [hep-ex].
- [79] M. Cacciari, G. P. Salam and G. Soyez, *The anti- k_t jet clustering algorithm*, *JHEP* **0804** (2008) 063, arXiv:0802.1189 [hep-ph].
- [80] ATLAS Collaboration, *Performance of pile-up mitigation techniques for jets in pp collisions with the ATLAS detector*, *Nucl. Instrum. Meth.* **A824** (2016) 367–370, arXiv:1510.03823 [hep-ex].
- [81] Y. L. Dokshitzer et al., *Better jet clustering algorithms*, *JHEP* **9708** (1997) 001, arXiv:hep-ph/9707323 [hep-ph].
- [82] S. Catani et al., *Longitudinally invariant k_{\perp} clustering algorithms for hadron hadron collisions*, *Nucl. Phys.* **B406** (1993) 187.
- [83] ATLAS Collaboration, *Jet mass and substructure of inclusive jets in $\sqrt{s} = 7$ TeV pp collisions with the ATLAS experiment*, *JHEP* **1205** (2012) 128, arXiv:1203.4606 [hep-ex].
- [84] ATLAS Collaboration, *Performance of Missing Transverse Momentum Reconstruction in ATLAS with 2011 Proton-Proton Collisions at $\sqrt{s} = 7$ TeV*, (2012), URL: <https://cds.cern.ch/record/1463915>.
- [85] ATLAS Collaboration, *Improved luminosity determination in pp collisions at $\sqrt{s} = 7$ TeV using the ATLAS detector at the LHC*, *Eur. Phys. J.* **C73** (2013) 2518, arXiv:1302.4393 [hep-ex].
- [86] ATLAS Collaboration, *Performance of b-Jet Identification in the ATLAS Experiment*, *JINST* **11** (2016) P04008, arXiv:1512.01094 [hep-ex].
- [87] J. M. Butterworth, B. E. Cox and J. R. Forshaw, *WW scattering at the CERN LHC*, *Phys. Rev.* **D65** (2002) 096014, arXiv:hep-ph/0201098 [hep-ph].

- [88] ATLAS Collaboration, *Identification of boosted, hadronically decaying W bosons and comparisons with ATLAS data taken at $\sqrt{s} = 8$ TeV*, *Eur. Phys. J.* **C76** (2016) 154, arXiv:1510.05821 [hep-ex].
- [89] J. Thaler and K. Van Tilburg, *Identifying boosted objects with N-subjettiness*, *JHEP* **1103** (2011) 015, arXiv:1011.2268 [hep-ph].
- [90] J. Thaler and K. Van Tilburg, *Maximizing boosted top identification by minimizing N-subjettiness*, *JHEP* **1202** (2012) 093, arXiv:1108.2701 [hep-ph].
- [91] CMS Collaboration, *Identification techniques for highly boosted W bosons that decay into hadrons*, *JHEP* **1412** (2014) 017, arXiv:1410.4227 [hep-ex].
- [92] ATLAS Collaboration, *A new method to distinguish hadronically decaying boosted Z bosons from W bosons using the ATLAS detector*, *Eur. Phys. J.* **C76** (2016) 238, arXiv:1509.04939 [hep-ex].
- [93] G. Kasieczka et al., *Resonance Searches with an Updated Top Tagger*, *JHEP* **06** (2015) 203, arXiv:1503.05921 [hep-ph].
- [94] ATLAS Collaboration, *Calibration of b-tagging using dileptonic top pair events in a combinatorial likelihood approach with the ATLAS experiment*, (2014), URL: <https://cds.cern.ch/record/1741020>.
- [95] ATLAS Collaboration, *Calibration of the performance of b-tagging for c and light-flavour jets in the 2012 ATLAS data*, (2014), URL: <https://cds.cern.ch/record/1741020>.
- [96] S. Schätzel and M. Spannowsky, *Tagging highly boosted top quarks*, *Phys. Rev.* **D89** (2014) 014007, arXiv:1308.0540 [hep-ph].

The ATLAS Collaboration

G. Aad⁸⁶, B. Abbott¹¹⁴, J. Abdallah¹⁵², O. Abdinov¹¹, R. Aben¹⁰⁸, M. Abolins⁹¹, O.S. AbouZeid¹⁵⁹, H. Abramowicz¹⁵⁴, H. Abreu¹⁵³, R. Abreu¹¹⁷, Y. Abulaiti^{147a,147b}, B.S. Acharya^{164a,164b,a}, L. Adamczyk^{39a}, D.L. Adams²⁶, J. Adelman¹⁰⁹, S. Adomeit¹⁰¹, T. Adye¹³², A.A. Affolder⁷⁵, T. Agatonovic-Jovin¹³, J. Agricola⁵⁵, J.A. Aguilar-Saavedra^{127a,127f}, S.P. Ahlen²³, F. Ahmadov^{66,b}, G. Aielli^{134a,134b}, H. Akerstedt^{147a,147b}, T.P.A. Åkesson⁸², A.V. Akimov⁹⁷, G.L. Alberghi^{21a,21b}, J. Albert¹⁶⁹, S. Albrand⁵⁶, M.J. Alconada Verzini⁷², M. Aleksa³¹, I.N. Aleksandrov⁶⁶, C. Alexa^{27b}, G. Alexander¹⁵⁴, T. Alexopoulos¹⁰, M. Alhroob¹¹⁴, G. Alimonti^{92a}, L. Alio⁸⁶, J. Alison³², S.P. Alkire³⁶, B.M.M. Allbrooke¹⁵⁰, P.P. Allport¹⁸, A. Aloisio^{105a,105b}, A. Alonso³⁷, F. Alonso⁷², C. Alpigiani¹³⁹, A. Altheimer³⁶, B. Alvarez Gonzalez³¹, D. Álvarez Piqueras¹⁶⁷, M.G. Alviggi^{105a,105b}, B.T. Amadio¹⁵, K. Amako⁶⁷, Y. Amaral Coutinho^{25a}, C. Amelung²⁴, D. Amidei⁹⁰, S.P. Amor Dos Santos^{127a,127c}, A. Amorim^{127a,127b}, S. Amoroso⁴⁹, N. Amram¹⁵⁴, G. Amundsen²⁴, C. Anastopoulos¹⁴⁰, L.S. Ancu⁵⁰, N. Andari¹⁰⁹, T. Andeen³⁶, C.F. Anders^{59b}, G. Anders³¹, J.K. Anders⁷⁵, K.J. Anderson³², A. Andreazza^{92a,92b}, V. Andrei^{59a}, S. Angelidakis⁹, I. Angelozzi¹⁰⁸, P. Anger⁴⁵, A. Angerami³⁶, F. Anghinolfi³¹, A.V. Anisenkov^{110,c}, N. Anjos¹², A. Annovi^{125a,125b}, M. Antonelli⁴⁸, A. Antonov⁹⁹, J. Antos^{145b}, F. Anulli^{133a}, M. Aoki⁶⁷, L. Aperio Bella¹⁸, G. Arabidze⁹¹, Y. Arai⁶⁷, J.P. Araque^{127a}, A.T.H. Arce⁴⁶, F.A. Arduh⁷², J-F. Arguin⁹⁶, S. Argyropoulos⁶⁴, M. Arik^{19a}, A.J. Armbruster³¹, O. Arnaez³¹, H. Arnold⁴⁹, M. Arratia²⁹, O. Arslan²², A. Artamonov⁹⁸, G. Artoni²⁴, S. Asai¹⁵⁶, N. Asbah⁴³, A. Ashkenazi¹⁵⁴, B. Åsman^{147a,147b}, L. Asquith¹⁵⁰, K. Assamagan²⁶, R. Astalos^{145a}, M. Atkinson¹⁶⁶, N.B. Atlay¹⁴², K. Augsten¹²⁹, M. Aurousseau^{146b}, G. Avolio³¹, B. Axen¹⁵, M.K. Ayoub¹¹⁸, G. Azuelos^{96,d}, M.A. Baak³¹, A.E. Baas^{59a}, M.J. Baca¹⁸, C. Bacci^{135a,135b}, H. Bachacou¹³⁷, K. Bachas¹⁵⁵, M. Backes³¹, M. Backhaus³¹, P. Bagiacchi^{133a,133b}, P. Bagnaia^{133a,133b}, Y. Bai^{34a}, T. Bain³⁶, J.T. Baines¹³², O.K. Baker¹⁷⁶, E.M. Baldin^{110,c}, P. Balek¹³⁰, T. Balestri¹⁴⁹, F. Balli⁸⁵, W.K. Balunas¹²³, E. Banas⁴⁰, Sw. Banerjee¹⁷³, A.A.E. Bannoura¹⁷⁵, L. Barak³¹, E.L. Barberio⁸⁹, D. Barberis^{51a,51b}, M. Barbero⁸⁶, T. Barillari¹⁰², M. Barisonzi^{164a,164b}, T. Barklow¹⁴⁴, N. Barlow²⁹, S.L. Barnes⁸⁵, B.M. Barnett¹³², R.M. Barnett¹⁵, Z. Barnovska⁵, A. Baroncelli^{135a}, G. Barone²⁴, A.J. Barr¹²¹, F. Barreiro⁸³, J. Barreiro Guimarães da Costa⁵⁸, R. Bartoldus¹⁴⁴, A.E. Barton⁷³, P. Bartos^{145a}, A. Basalae¹²⁴, A. Bassalat¹¹⁸, A. Basye¹⁶⁶, R.L. Bates⁵⁴, S.J. Batista¹⁵⁹, J.R. Batley²⁹, M. Battaglia¹³⁸, M. Bauce^{133a,133b}, F. Bauer¹³⁷, H.S. Bawa^{144,e}, J.B. Beacham¹¹², M.D. Beattie⁷³, T. Beau⁸¹, P.H. Beauchemin¹⁶², R. Beccherle^{125a,125b}, P. Bechtel²², H.P. Beck^{17,f}, K. Becker¹²¹, M. Becker⁸⁴, M. Beckingham¹⁷⁰, C. Becot¹¹⁸, A.J. Beddall^{19b}, A. Beddall^{19b}, V.A. Bednyakov⁶⁶, C.P. Bee¹⁴⁹, L.J. Beemster¹⁰⁸, T.A. Beermann³¹, M. Begel²⁶, J.K. Behr¹²¹, C. Belanger-Champagne⁸⁸, W.H. Bell⁵⁰, G. Bella¹⁵⁴, L. Bellagamba^{21a}, A. Bellerive³⁰, M. Bellomo⁸⁷, K. Belotskiy⁹⁹, O. Beltramello³¹, O. Benary¹⁵⁴, D. Benchebkroun^{136a}, M. Bender¹⁰¹, K. Bendtz^{147a,147b}, N. Benekos¹⁰, Y. Benhammou¹⁵⁴, E. Benhar Noccioli⁵⁰, J.A. Benitez Garcia^{160b}, D.P. Benjamin⁴⁶, J.R. Bensinger²⁴, S. Bentvelsen¹⁰⁸, L. Beresford¹²¹, M. Beretta⁴⁸, D. Berge¹⁰⁸, E. Bergeas Kuutmann¹⁶⁵, N. Berger⁵, F. Berghaus¹⁶⁹, J. Beringer¹⁵, C. Bernard²³, N.R. Bernard⁸⁷, C. Bernius¹¹¹, F.U. Bernlochner²², T. Berry⁷⁸, P. Berta¹³⁰, C. Bertella⁸⁴, G. Bertoli^{147a,147b}, F. Bertolucci^{125a,125b}, C. Bertsche¹¹⁴, D. Bertsche¹¹⁴, M.I. Besana^{92a}, G.J. Besjes³⁷, O. Bessidskaia Bylund^{147a,147b}, M. Bessner⁴³, N. Besson¹³⁷, C. Betancourt⁴⁹, S. Bethke¹⁰², A.J. Bevan⁷⁷, W. Bhimji¹⁵, R.M. Bianchi¹²⁶, L. Bianchini²⁴, M. Bianco³¹, O. Biebel¹⁰¹, D. Biedermann¹⁶, S.P. Bieniek⁷⁹, N.V. Biesuz^{125a,125b}, M. Biglietti^{135a}, J. Bilbao De Mendizabal⁵⁰, H. Bilokon⁴⁸, M. Bindi⁵⁵, S. Binet¹¹⁸, A. Bingul^{19b}, C. Bini^{133a,133b}, S. Biondi^{21a,21b}, D.M. Bjergaard⁴⁶, C.W. Black¹⁵¹, J.E. Black¹⁴⁴, K.M. Black²³, D. Blackburn¹³⁹, R.E. Blair⁶, J.-B. Blanchard¹³⁷, J.E. Blanco⁷⁸, T. Blazek^{145a}, I. Bloch⁴³, C. Blocker²⁴, W. Blum^{84,*}, U. Blumenschein⁵⁵, S. Blunier^{33a},

G.J. Bobbink¹⁰⁸, V.S. Bobrovnikov^{110,c}, S.S. Bocchetta⁸², A. Bocci⁴⁶, C. Bock¹⁰¹, M. Boehler⁴⁹, J.A. Bogaerts³¹, D. Bogavac¹³, A.G. Bogdanchikov¹¹⁰, C. Bohm^{147a}, V. Boisvert⁷⁸, T. Bold^{39a}, V. Boldea^{27b}, A.S. Boldyrev¹⁰⁰, M. Bomben⁸¹, M. Bona⁷⁷, M. Boonekamp¹³⁷, A. Borisov¹³¹, G. Borissov⁷³, S. Borroni⁴³, J. Bortfeldt¹⁰¹, V. Bortolotto^{61a,61b,61c}, K. Bos¹⁰⁸, D. Boscherini^{21a}, M. Bosman¹², J. Boudreau¹²⁶, J. Bouffard², E.V. Bouhova-Thacker⁷³, D. Boumediene³⁵, C. Bourdarios¹¹⁸, N. Bousson¹¹⁵, S.K. Boutle⁵⁴, A. Boveia³¹, J. Boyd³¹, I.R. Boyko⁶⁶, I. Bozic¹³, J. Bracinik¹⁸, A. Brandt⁸, G. Brandt⁵⁵, O. Brandt^{59a}, U. Bratzler¹⁵⁷, B. Brau⁸⁷, J.E. Brau¹¹⁷, H.M. Braun^{175,*}, W.D. Breaden Madden⁵⁴, K. Brendlinger¹²³, A.J. Brennan⁸⁹, L. Brenner¹⁰⁸, R. Brenner¹⁶⁵, S. Bressler¹⁷², T.M. Bristow⁴⁷, D. Britton⁵⁴, D. Britzger⁴³, F.M. Brochu²⁹, I. Brock²², R. Brock⁹¹, J. Bronner¹⁰², G. Brooijmans³⁶, T. Brooks⁷⁸, W.K. Brooks^{33b}, J. Brosamer¹⁵, E. Brost¹¹⁷, P.A. Bruckman de Renstrom⁴⁰, D. Bruncko^{145b}, R. Bruneliere⁴⁹, A. Bruni^{21a}, G. Bruni^{21a}, M. Bruschi^{21a}, N. Bruscinò²², L. Bryngemark⁸², T. Buanes¹⁴, Q. Buat¹⁴³, P. Buchholz¹⁴², A.G. Buckley⁵⁴, S.I. Buda^{27b}, I.A. Budagov⁶⁶, F. Buehrer⁴⁹, L. Bugge¹²⁰, M.K. Bugge¹²⁰, O. Bulekov⁹⁹, D. Bullock⁸, H. Burckhart³¹, S. Burdin⁷⁵, C.D. Burgard⁴⁹, B. Burghgrave¹⁰⁹, S. Burke¹³², I. Burmeister⁴⁴, E. Busato³⁵, D. Büscher⁴⁹, V. Büscher⁸⁴, P. Bussey⁵⁴, J.M. Butler²³, A.I. Butt³, C.M. Buttar⁵⁴, J.M. Butterworth⁷⁹, P. Butti¹⁰⁸, W. Buttinger²⁶, A. Buzatu⁵⁴, A.R. Buzykaev^{110,c}, S. Cabrera Urbán¹⁶⁷, D. Caforio¹²⁹, V.M. Cairo^{38a,38b}, O. Cakir^{4a}, N. Calace⁵⁰, P. Calafiura¹⁵, A. Calandri¹³⁷, G. Calderini⁸¹, P. Calfayan¹⁰¹, L.P. Caloba^{25a}, D. Calvet³⁵, S. Calvet³⁵, R. Camacho Toro³², S. Camarda⁴³, P. Camarri^{134a,134b}, D. Cameron¹²⁰, R. Caminal Armadans¹⁶⁶, S. Campana³¹, M. Campanelli⁷⁹, A. Campoverde¹⁴⁹, V. Canale^{105a,105b}, A. Canepa^{160a}, M. Cano Bret^{34e}, J. Cantero⁸³, R. Cantrill^{127a}, T. Cao⁴¹, M.D.M. Capeans Garrido³¹, I. Caprini^{27b}, M. Caprini^{27b}, M. Capua^{38a,38b}, R. Caputo⁸⁴, R.M. Carbone³⁶, R. Cardarelli^{134a}, F. Cardillo⁴⁹, T. Carli³¹, G. Carlino^{105a}, L. Carminati^{92a,92b}, S. Caron¹⁰⁷, E. Carquin^{33a}, G.D. Carrillo-Montoya³¹, J.R. Carter²⁹, J. Carvalho^{127a,127c}, D. Casadei⁷⁹, M.P. Casado^{12,g}, M. Casolino¹², E. Castaneda-Miranda^{146a}, A. Castelli¹⁰⁸, V. Castillo Gimenez¹⁶⁷, N.F. Castro^{127a,h}, P. Catastini⁵⁸, A. Catinaccio³¹, J.R. Catmore¹²⁰, A. Cattai³¹, J. Caudron⁸⁴, V. Cavaliere¹⁶⁶, D. Cavalli^{92a}, M. Cavalli-Sforza¹², V. Cavasinni^{125a,125b}, F. Ceradini^{135a,135b}, B.C. Cerio⁴⁶, K. Cerny¹³⁰, A.S. Cerqueira^{25b}, A. Cerri¹⁵⁰, L. Cerrito⁷⁷, F. Cerutti¹⁵, M. Cerv³¹, A. Cervelli¹⁷, S.A. Cetin^{19c}, A. Chafaq^{136a}, D. Chakraborty¹⁰⁹, I. Chalupkova¹³⁰, Y.L. Chan^{61a}, P. Chang¹⁶⁶, J.D. Chapman²⁹, D.G. Charlton¹⁸, C.C. Chau¹⁵⁹, C.A. Chavez Barajas¹⁵⁰, S. Cheatham¹⁵³, A. Chegwidden⁹¹, S. Chekanov⁶, S.V. Chekulaev^{160a}, G.A. Chelkov^{66,i}, M.A. Chelstowska⁹⁰, C. Chen⁶⁵, H. Chen²⁶, K. Chen¹⁴⁹, L. Chen^{34d,j}, S. Chen^{34c}, S. Chen¹⁵⁶, X. Chen^{34f}, Y. Chen⁶⁸, H.C. Cheng⁹⁰, Y. Cheng³², A. Cheplakov⁶⁶, E. Cheremushkina¹³¹, R. Cherkaoui El Moursli^{136e}, V. Chernyatin^{26,*}, E. Cheu⁷, L. Chevalier¹³⁷, V. Chiarella⁴⁸, G. Chiarelli^{125a,125b}, G. Chiodini^{74a}, A.S. Chisholm¹⁸, R.T. Chislett⁷⁹, A. Chitan^{27b}, M.V. Chizhov⁶⁶, K. Choi⁶², S. Chouridou⁹, B.K.B. Chow¹⁰¹, V. Christodoulou⁷⁹, D. Chromek-Burckhart³¹, J. Chudoba¹²⁸, A.J. Chuinard⁸⁸, J.J. Chwastowski⁴⁰, L. Chytka¹¹⁶, G. Ciapetti^{133a,133b}, A.K. Ciftci^{4a}, D. Cina⁵⁴, V. Cindro⁷⁶, I.A. Cioara²², A. Ciocio¹⁵, F. Ciotto^{105a,105b}, Z.H. Citron¹⁷², M. Ciubancan^{27b}, A. Clark⁵⁰, B.L. Clark⁵⁸, P.J. Clark⁴⁷, R.N. Clarke¹⁵, C. Clement^{147a,147b}, Y. Coadou⁸⁶, M. Cobal^{164a,164c}, A. Coccaro⁵⁰, J. Cochran⁶⁵, L. Coffey²⁴, J.G. Cogan¹⁴⁴, L. Colasurdo¹⁰⁷, B. Cole³⁶, S. Cole¹⁰⁹, A.P. Colijn¹⁰⁸, J. Collot⁵⁶, T. Colombo^{59c}, G. Compostella¹⁰², P. Conde Muiño^{127a,127b}, E. Coniavitis⁴⁹, S.H. Connell^{146b}, I.A. Connelly⁷⁸, V. Consorti⁴⁹, S. Constantinescu^{27b}, C. Conta^{122a,122b}, G. Conti³¹, F. Conventi^{105a,k}, M. Cooke¹⁵, B.D. Cooper⁷⁹, A.M. Cooper-Sarkar¹²¹, T. Cornelissen¹⁷⁵, M. Corradi^{133a,133b}, F. Corriveau^{88,l}, A. Corso-Radu¹⁶³, A. Cortes-Gonzalez¹², G. Cortiana¹⁰², G. Costa^{92a}, M.J. Costa¹⁶⁷, D. Costanzo¹⁴⁰, D. Côté⁸, G. Cottin²⁹, G. Cowan⁷⁸, B.E. Cox⁸⁵, K. Cranmer¹¹¹, G. Cree³⁰, S. Crépe-Renaudin⁵⁶, F. Crescioli⁸¹, W.A. Cribbs^{147a,147b}, M. Crispin Ortuzar¹²¹, M. Cristinziani²², V. Croft¹⁰⁷, G. Crosetti^{38a,38b}, T. Cuhadar Donszelmann¹⁴⁰, J. Cummings¹⁷⁶, M. Curatolo⁴⁸, J. Cúth⁸⁴, C. Cuthbert¹⁵¹, H. Czirr¹⁴², P. Czodrowski³, S. D'Auria⁵⁴,

M. D'Onofrio⁷⁵, M.J. Da Cunha Sargedas De Sousa^{127a,127b}, C. Da Via⁸⁵, W. Dabrowski^{39a},
A. Dafinca¹²¹, T. Dai⁹⁰, O. Dale¹⁴, F. Dallaire⁹⁶, C. Dallapiccola⁸⁷, M. Dam³⁷, J.R. Dandoy³²,
N.P. Dang⁴⁹, A.C. Daniells¹⁸, M. Danninger¹⁶⁸, M. Dano Hoffmann¹³⁷, V. Dao⁴⁹, G. Darbo^{51a},
S. Darmora⁸, J. Dassoulas³, A. Dattagupta⁶², W. Davey²², C. David¹⁶⁹, T. Davidek¹³⁰, E. Davies^{121,m},
M. Davies¹⁵⁴, P. Davison⁷⁹, Y. Davygora^{59a}, E. Dawe⁸⁹, I. Dawson¹⁴⁰, R.K. Daya-Ishmukhametova⁸⁷,
K. De⁸, R. de Asmundis^{105a}, A. De Benedetti¹¹⁴, S. De Castro^{21a,21b}, S. De Cecco⁸¹, N. De Groot¹⁰⁷,
P. de Jong¹⁰⁸, H. De la Torre⁸³, F. De Lorenzi⁶⁵, D. De Pedis^{133a}, A. De Salvo^{133a}, U. De Sanctis¹⁵⁰,
A. De Santo¹⁵⁰, J.B. De Vivie De Regie¹¹⁸, W.J. Dearnaley⁷³, R. Debbe²⁶, C. Debenedetti¹³⁸,
D.V. Dedovich⁶⁶, I. Deigaard¹⁰⁸, J. Del Peso⁸³, T. Del Prete^{125a,125b}, D. Delgove¹¹⁸, F. Deliot¹³⁷,
C.M. Delitzsch⁵⁰, M. Deliyergiyev⁷⁶, A. Dell'Acqua³¹, L. Dell'Asta²³, M. Dell'Orso^{125a,125b},
M. Della Pietra^{105a,k}, D. della Volpe⁵⁰, M. Delmastro⁵, P.A. Delsart⁵⁶, C. Deluca¹⁰⁸, D.A. DeMarco¹⁵⁹,
S. Demers¹⁷⁶, M. Demichev⁶⁶, A. Demilly⁸¹, S.P. Denisov¹³¹, D. Derendarz⁴⁰, J.E. Derkaoui^{136d},
F. Derue⁸¹, P. Dervan⁷⁵, K. Desch²², C. Deterre⁴³, K. Dette⁴⁴, P.O. Deviveiros³¹, A. Dewhurst¹³²,
S. Dhaliwal²⁴, A. Di Ciaccio^{134a,134b}, L. Di Ciaccio⁵, A. Di Domenico^{133a,133b}, C. Di Donato^{133a,133b},
A. Di Girolamo³¹, B. Di Girolamo³¹, A. Di Mattia¹⁵³, B. Di Micco^{135a,135b}, R. Di Nardo⁴⁸,
A. Di Simone⁴⁹, R. Di Sipio¹⁵⁹, D. Di Valentino³⁰, C. Diaconu⁸⁶, M. Diamond¹⁵⁹, F.A. Dias⁴⁷,
M.A. Diaz^{33a}, E.B. Diehl⁹⁰, J. Dietrich¹⁶, S. Diglio⁸⁶, A. Dimitrievska¹³, J. Dingfelder²², P. Dita^{27b},
S. Dita^{27b}, F. Dittus³¹, F. Djama⁸⁶, T. Djobava^{52b}, J.I. Djuvsland^{59a}, M.A.B. do Vale^{25c}, D. Dobos³¹,
M. Dobre^{27b}, C. Doglioni⁸², T. Dohmae¹⁵⁶, J. Dolejsi¹³⁰, Z. Dolezal¹³⁰, B.A. Dolgoshein^{99,*},
M. Donadelli^{25d}, S. Donati^{125a,125b}, P. Dondero^{122a,122b}, J. Donini³⁵, J. Dopke¹³², A. Doria^{105a},
M.T. Dova⁷², A.T. Doyle⁵⁴, E. Drechsler⁵⁵, M. Dris¹⁰, E. Dubreuil³⁵, E. Duchovni¹⁷², G. Duckeck¹⁰¹,
O.A. Ducu^{27b}, D. Duda¹⁰⁸, A. Dudarev³¹, L. Dufflot¹¹⁸, L. Duguid⁷⁸, M. Dührssen³¹, M. Dunford^{59a},
H. Duran Yildiz^{4a}, M. Düren⁵³, A. Durglishvili^{52b}, D. Duschinger⁴⁵, B. Dutta⁴³, M. Dyndal^{39a},
C. Eckardt⁴³, K.M. Ecker¹⁰², R.C. Edgar⁹⁰, W. Edson², N.C. Edwards⁴⁷, W. Ehrenfeld²², T. Eifert³¹,
G. Eigen¹⁴, K. Einsweiler¹⁵, T. Ekelof¹⁶⁵, M. El Kacimi^{136c}, M. Ellert¹⁶⁵, S. Elles⁵, F. Ellinghaus¹⁷⁵,
A.A. Elliot¹⁶⁹, N. Ellis³¹, J. Elmsheuser¹⁰¹, M. Elsing³¹, D. Emelianov¹³², Y. Enari¹⁵⁶, O.C. Endner⁸⁴,
M. Endo¹¹⁹, J. Erdmann⁴⁴, A. Ereditato¹⁷, G. Ernis¹⁷⁵, J. Ernst², M. Ernst²⁶, S. Errede¹⁶⁶, E. Ertel⁸⁴,
M. Escalier¹¹⁸, H. Esch⁴⁴, C. Escobar¹²⁶, B. Esposito⁴⁸, A.I. Etienvre¹³⁷, E. Etzion¹⁵⁴, H. Evans⁶²,
A. Ezhilov¹²⁴, L. Fabbri^{21a,21b}, G. Facini³², R.M. Fakhrutdinov¹³¹, S. Falciano^{133a}, R.J. Falla⁷⁹,
J. Faltova¹³⁰, Y. Fang^{34a}, M. Fanti^{92a,92b}, A. Farbin⁸, A. Farilla^{135a}, T. Farooque¹², S. Farrell¹⁵,
S.M. Farrington¹⁷⁰, P. Farthouat³¹, F. Fassi^{136e}, P. Fassnacht³¹, D. Fassouliotis⁹, M. Faucci Giannelli⁷⁸,
A. Favareto^{51a,51b}, L. Fayard¹¹⁸, O.L. Fedin^{124,n}, W. Fedorko¹⁶⁸, S. Feigl³¹, L. Feligioni⁸⁶, C. Feng^{34d},
E.J. Feng³¹, H. Feng⁹⁰, A.B. Fenyuk¹³¹, L. Feremenga⁸, P. Fernandez Martinez¹⁶⁷,
S. Fernandez Perez³¹, J. Ferrando⁵⁴, A. Ferrari¹⁶⁵, P. Ferrari¹⁰⁸, R. Ferrari^{122a}, D.E. Ferreira de Lima⁵⁴,
A. Ferrer¹⁶⁷, D. Ferrere⁵⁰, C. Ferretti⁹⁰, A. Ferretto Parodi^{51a,51b}, M. Fiascaris³², F. Fiedler⁸⁴,
A. Filipčić⁷⁶, M. Filipuzzi⁴³, F. Filthaut¹⁰⁷, M. Fincke-Keeler¹⁶⁹, K.D. Finelli¹⁵¹,
M.C.N. Fiolhais^{127a,127c}, L. Fiorini¹⁶⁷, A. Firan⁴¹, A. Fischer², C. Fischer¹², J. Fischer¹⁷⁵, W.C. Fisher⁹¹,
N. Flaschel⁴³, I. Fleck¹⁴², P. Fleischmann⁹⁰, G.T. Fletcher¹⁴⁰, G. Fletcher⁷⁷, R.R.M. Fletcher¹²³,
T. Flick¹⁷⁵, A. Floderus⁸², L.R. Flores Castillo^{61a}, M.J. Flowerdew¹⁰², A. Formica¹³⁷, A. Forti⁸⁵,
D. Fournier¹¹⁸, H. Fox⁷³, S. Fracchia¹², P. Francavilla⁸¹, M. Franchini^{21a,21b}, D. Francis³¹,
L. Franconi¹²⁰, M. Franklin⁵⁸, M. Frate¹⁶³, M. Fraternali^{122a,122b}, D. Freeborn⁷⁹, S.T. French²⁹,
F. Friedrich⁴⁵, D. Froidevaux³¹, J.A. Frost¹²¹, C. Fukunaga¹⁵⁷, E. Fullana Torregrosa⁸⁴, B.G. Fulsom¹⁴⁴,
T. Fusayasu¹⁰³, J. Fuster¹⁶⁷, C. Gabaldon⁵⁶, O. Gabizon¹⁷⁵, A. Gabrielli^{21a,21b}, A. Gabrielli¹⁵,
G.P. Gach¹⁸, S. Gadatsch³¹, S. Gadomski⁵⁰, G. Gagliardi^{51a,51b}, P. Gagnon⁶², C. Galea¹⁰⁷,
B. Galhardo^{127a,127c}, E.J. Gallas¹²¹, B.J. Gallop¹³², P. Gallus¹²⁹, G. Galster³⁷, K.K. Gan¹¹², J. Gao^{34b,86},
Y. Gao⁴⁷, Y.S. Gao^{144,e}, F.M. Garay Walls⁴⁷, F. Garberon¹⁷⁶, C. García¹⁶⁷, J.E. García Navarro¹⁶⁷,
M. Garcia-Sciveres¹⁵, R.W. Gardner³², N. Garelli¹⁴⁴, V. Garonne¹²⁰, C. Gatti⁴⁸, A. Gaudiello^{51a,51b},

G. Gaudio^{122a}, B. Gaur¹⁴², L. Gauthier⁹⁶, P. Gauzzi^{133a,133b}, I.L. Gavrilenko⁹⁷, C. Gay¹⁶⁸, G. Gaycken²², E.N. Gazis¹⁰, P. Ge^{34d}, Z. Gecse¹⁶⁸, C.N.P. Gee¹³², Ch. Geich-Gimbel²², M.P. Geisler^{59a}, C. Gemme^{51a}, M.H. Genest⁵⁶, S. Gentile^{133a,133b}, M. George⁵⁵, S. George⁷⁸, D. Gerbaudo¹⁶³, A. Gershon¹⁵⁴, S. Ghasemi¹⁴², H. Ghazlane^{136b}, B. Giacobbe^{21a}, S. Giagu^{133a,133b}, V. Giangiobbe¹², P. Giannetti^{125a,125b}, B. Gibbard²⁶, S.M. Gibson⁷⁸, M. Gignac¹⁶⁸, M. Gilchriese¹⁵, T.P.S. Gillam²⁹, D. Gillberg³¹, G. Gilles³⁵, D.M. Gingrich^{3,d}, N. Giokaris⁹, M.P. Giordani^{164a,164c}, F.M. Giorgi^{21a}, F.M. Giorgi¹⁶, P.F. Giraud¹³⁷, P. Giromini⁴⁸, D. Giugni^{92a}, C. Giuliani¹⁰², M. Giulini^{59b}, B.K. Gjelsten¹²⁰, S. Gkaitatzis¹⁵⁵, I. Gkialas¹⁵⁵, E.L. Gkoukousis¹¹⁸, L.K. Gladilin¹⁰⁰, C. Glasman⁸³, J. Glatzer³¹, P.C.F. Glaysher⁴⁷, A. Glazov⁴³, M. Goblirsch-Kolb¹⁰², J.R. Goddard⁷⁷, J. Godlewski⁴⁰, S. Goldfarb⁹⁰, T. Golling⁵⁰, D. Golubkov¹³¹, A. Gomes^{127a,127b,127d}, R. Gonçalo^{127a}, J. Goncalves Pinto Firmino Da Costa¹³⁷, L. Gonella²², S. González de la Hoz¹⁶⁷, G. Gonzalez Parra¹², S. Gonzalez-Sevilla⁵⁰, L. Goossens³¹, P.A. Gorbounov⁹⁸, H.A. Gordon²⁶, I. Gorelov¹⁰⁶, B. Gorini³¹, E. Gorini^{74a,74b}, A. Gorišek⁷⁶, E. Gornicki⁴⁰, A.T. Goshaw⁴⁶, C. Gössling⁴⁴, M.I. Gostkin⁶⁶, D. Goujdami^{136c}, A.G. Goussiou¹³⁹, N. Govender^{146b}, E. Gozani¹⁵³, H.M.X. Grabas¹³⁸, L. Graber⁵⁵, I. Grabowska-Bold^{39a}, P.O.J. Gradin¹⁶⁵, P. Grafström^{21a,21b}, K-J. Grahn⁴³, J. Gramling⁵⁰, E. Gramstad¹²⁰, S. Grancagnolo¹⁶, V. Gratchev¹²⁴, H.M. Gray³¹, E. Graziani^{135a}, Z.D. Greenwood^{80,o}, C. Grefe²², K. Gregersen⁷⁹, I.M. Gregor⁴³, P. Grenier¹⁴⁴, J. Griffiths⁸, A.A. Grillo¹³⁸, K. Grimm⁷³, S. Grinstein^{12,p}, Ph. Gris³⁵, J.-F. Grivaz¹¹⁸, J.P. Grohs⁴⁵, A. Grohsjean⁴³, E. Gross¹⁷², J. Grosse-Knetter⁵⁵, G.C. Grossi⁸⁰, Z.J. Grout¹⁵⁰, L. Guan⁹⁰, J. Guenther¹²⁹, F. Guescini⁵⁰, D. Guest¹⁶³, O. Gueta¹⁵⁴, E. Guido^{51a,51b}, T. Guillemain¹¹⁸, S. Guindon², U. Gul⁵⁴, C. Gumpert⁴⁵, J. Guo^{34e}, Y. Guo^{34b,q}, S. Gupta¹²¹, G. Gustavino^{133a,133b}, P. Gutierrez¹¹⁴, N.G. Gutierrez Ortiz⁷⁹, C. Gutschow⁴⁵, C. Guyot¹³⁷, C. Gwenlan¹²¹, C.B. Gwilliam⁷⁵, A. Haas¹¹¹, C. Haber¹⁵, H.K. Hadavand⁸, N. Haddad^{136e}, P. Haefner²², S. Hageböck²², Z. Hajduk⁴⁰, H. Hakobyan¹⁷⁷, M. Haleem⁴³, J. Haley¹¹⁵, D. Hall¹²¹, G. Halladjian⁹¹, G.D. Hallewell⁸⁶, K. Hamacher¹⁷⁵, P. Hamal¹¹⁶, K. Hamano¹⁶⁹, A. Hamilton^{146a}, G.N. Hamity¹⁴⁰, P.G. Hamnett⁴³, L. Han^{34b}, K. Hanagaki^{67,r}, K. Hanawa¹⁵⁶, M. Hance¹³⁸, B. Haney¹²³, P. Hanke^{59a}, R. Hanna¹³⁷, J.B. Hansen³⁷, J.D. Hansen³⁷, M.C. Hansen²², P.H. Hansen³⁷, K. Hara¹⁶¹, A.S. Hard¹⁷³, T. Harenberg¹⁷⁵, F. Hariri¹¹⁸, S. Harkusha⁹³, R.D. Harrington⁴⁷, P.F. Harrison¹⁷⁰, F. Hartjes¹⁰⁸, M. Hasegawa⁶⁸, Y. Hasegawa¹⁴¹, A. Hasib¹¹⁴, S. Hassani¹³⁷, S. Haug¹⁷, R. Hauser⁹¹, L. Hauswald⁴⁵, M. Havranek¹²⁸, C.M. Hawkes¹⁸, R.J. Hawkins³¹, A.D. Hawkins⁸², T. Hayashi¹⁶¹, D. Hayden⁹¹, C.P. Hays¹²¹, J.M. Hays⁷⁷, H.S. Hayward⁷⁵, S.J. Haywood¹³², S.J. Head¹⁸, T. Heck⁸⁴, V. Hedberg⁸², L. Heelan⁸, S. Heim¹²³, T. Heim¹⁷⁵, B. Heinemann¹⁵, L. Heinrich¹¹¹, J. Hejbal¹²⁸, L. Helary²³, S. Hellman^{147a,147b}, D. Hellmich²², C. Hensens¹², J. Henderson¹²¹, R.C.W. Henderson⁷³, Y. Heng¹⁷³, C. Hengler⁴³, S. Henkelmann¹⁶⁸, A. Henrichs¹⁷⁶, A.M. Henriques Correia³¹, S. Henrot-Versille¹¹⁸, G.H. Herbert¹⁶, Y. Hernández Jiménez¹⁶⁷, G. Herten⁴⁹, R. Hertenberger¹⁰¹, L. Hervas³¹, G.G. Hesketh⁷⁹, N.P. Hessey¹⁰⁸, J.W. Hetherly⁴¹, R. Hickling⁷⁷, E. Higón-Rodríguez¹⁶⁷, E. Hill¹⁶⁹, J.C. Hill²⁹, K.H. Hiller⁴³, S.J. Hillier¹⁸, I. Hinchliffe¹⁵, E. Hines¹²³, R.R. Hinman¹⁵, M. Hirose¹⁵⁸, D. Hirschbuehl¹⁷⁵, J. Hobbs¹⁴⁹, N. Hod¹⁰⁸, M.C. Hodgkinson¹⁴⁰, P. Hodgson¹⁴⁰, A. Hoecker³¹, M.R. Hoferkamp¹⁰⁶, F. Hoenig¹⁰¹, M. Hohlfeld⁸⁴, D. Hohn²², T.R. Holmes¹⁵, M. Homann⁴⁴, T.M. Hong¹²⁶, W.H. Hopkins¹¹⁷, Y. Horii¹⁰⁴, A.J. Horton¹⁴³, J.-Y. Hostachy⁵⁶, S. Hou¹⁵², A. Hoummada^{136a}, J. Howard¹²¹, J. Howarth⁴³, M. Hrabovsky¹¹⁶, I. Hristova¹⁶, J. Hrivnac¹¹⁸, T. Hryn'ova⁵, A. Hrynevich⁹⁴, C. Hsu^{146c}, P.J. Hsu^{152,s}, S.-C. Hsu¹³⁹, D. Hu³⁶, Q. Hu^{34b}, X. Hu⁹⁰, Y. Huang⁴³, Z. Hubacek¹²⁹, F. Hubaut⁸⁶, F. Huegging²², T.B. Huffman¹²¹, E.W. Hughes³⁶, G. Hughes⁷³, M. Huhtinen³¹, T.A. Hülsing⁸⁴, N. Huseynov^{66,b}, J. Huston⁹¹, J. Huth⁵⁸, G. Iacobucci⁵⁰, G. Iakovidis²⁶, I. Ibragimov¹⁴², L. Iconomidou-Fayard¹¹⁸, E. Ideal¹⁷⁶, Z. Idrissi^{136e}, P. Iengo³¹, O. Igonkina¹⁰⁸, T. Iizawa¹⁷¹, Y. Ikegami⁶⁷, M. Ikeno⁶⁷, Y. Ilchenko^{32,t}, D. Iliadis¹⁵⁵, N. Ilic¹⁴⁴, T. Ince¹⁰², G. Introzzi^{122a,122b}, P. Ioannou^{9,*}, M. Iodice^{135a}, K. Iordanidou³⁶, V. Ippolito⁵⁸, A. Irlés Quiles¹⁶⁷, C. Isaksson¹⁶⁵, M. Ishino⁶⁹, M. Ishitsuka¹⁵⁸, R. Ishmukhametov¹¹², C. Issever¹²¹, S. Istin^{19a},

J.M. Iturbe Ponce⁸⁵, R. Iuppa^{134a,134b}, J. Ivarsson⁸², W. Iwanski⁴⁰, H. Iwasaki⁶⁷, J.M. Izen⁴², V. Izzo^{105a}, S. Jabbar³, B. Jackson¹²³, M. Jackson⁷⁵, P. Jackson¹, M.R. Jaekel³¹, V. Jain², K. Jakobs⁴⁹, S. Jakobsen³¹, T. Jakoubek¹²⁸, J. Jakubek¹²⁹, D.O. Jamin¹¹⁵, D.K. Jana⁸⁰, E. Jansen⁷⁹, R. Jansky⁶³, J. Janssen²², M. Janus⁵⁵, G. Jarlskog⁸², N. Javadov^{66,b}, T. Javůrek⁴⁹, L. Jeanty¹⁵, J. Jejelava^{52a,u}, G.-Y. Jeng¹⁵¹, D. Jennens⁸⁹, P. Jenni^{49,v}, J. Jentzsch⁴⁴, C. Jeske¹⁷⁰, S. Jézéquel⁵, H. Ji¹⁷³, J. Jia¹⁴⁹, Y. Jiang^{34b}, S. Jiggins⁷⁹, J. Jimenez Pena¹⁶⁷, S. Jin^{34a}, A. Jinaru^{27b}, O. Jinnouchi¹⁵⁸, M.D. Joergensen³⁷, P. Johansson¹⁴⁰, K.A. Johns⁷, W.J. Johnson¹³⁹, K. Jon-And^{147a,147b}, G. Jones¹⁷⁰, R.W.L. Jones⁷³, T.J. Jones⁷⁵, J. Jongmanns^{59a}, P.M. Jorge^{127a,127b}, K.D. Joshi⁸⁵, J. Jovicevic^{160a}, X. Ju¹⁷³, P. Jussel⁶³, A. Juste Rozas^{12,p}, M. Kaci¹⁶⁷, A. Kaczmarek⁴⁰, M. Kado¹¹⁸, H. Kagan¹¹², M. Kagan¹⁴⁴, S.J. Kahn⁸⁶, E. Kajomovitz⁴⁶, C.W. Kalderon¹²¹, S. Kama⁴¹, A. Kamenshchikov¹³¹, N. Kanaya¹⁵⁶, S. Kaneti²⁹, V.A. Kantserov⁹⁹, J. Kanzaki⁶⁷, B. Kaplan¹¹¹, L.S. Kaplan¹⁷³, A. Kapliy³², D. Kar^{146c}, K. Karakostas¹⁰, A. Karamaoun³, N. Karastathis¹⁰, M.J. Kareem⁵⁵, E. Karentzos¹⁰, M. Karneviskiy⁸⁴, S.N. Karpov⁶⁶, Z.M. Karpova⁶⁶, K. Karthik¹¹¹, V. Kartvelishvili⁷³, A.N. Karyukhin¹³¹, K. Kasahara¹⁶¹, L. Kashif¹⁷³, R.D. Kass¹¹², A. Kastanas¹⁴, Y. Kataoka¹⁵⁶, C. Kato¹⁵⁶, A. Katre⁵⁰, J. Katzy⁴³, K. Kawade¹⁰⁴, K. Kawagoe⁷¹, T. Kawamoto¹⁵⁶, G. Kawamura⁵⁵, S. Kazama¹⁵⁶, V.F. Kazanin^{110,c}, R. Keeler¹⁶⁹, R. Kehoe⁴¹, J.S. Keller⁴³, J.J. Kempster⁷⁸, H. Keoshkerian⁸⁵, O. Kepka¹²⁸, B.P. Kerševan⁷⁶, S. Kersten¹⁷⁵, R.A. Keyes⁸⁸, F. Khalil-zada¹¹, H. Khandanyan^{147a,147b}, A. Khanov¹¹⁵, A.G. Kharlamov^{110,c}, T.J. Khoo²⁹, V. Khovanskiy⁹⁸, E. Khramov⁶⁶, J. Khubua^{52b,w}, S. Kido⁶⁸, H.Y. Kim⁸, S.H. Kim¹⁶¹, Y.K. Kim³², N. Kimura¹⁵⁵, O.M. Kind¹⁶, B.T. King⁷⁵, M. King¹⁶⁷, S.B. King¹⁶⁸, J. Kirk¹³², A.E. Kiryunin¹⁰², T. Kishimoto⁶⁸, D. Kisielewska^{39a}, F. Kiss⁴⁹, K. Kiuchi¹⁶¹, O. Kivernyk¹³⁷, E. Kladiva^{145b}, M.H. Klein³⁶, M. Klein⁷⁵, U. Klein⁷⁵, K. Kleinknecht⁸⁴, P. Klimek^{147a,147b}, A. Klimentov²⁶, R. Klingenberg⁴⁴, J.A. Klinger¹⁴⁰, T. Klioutchnikova³¹, E.-E. Kluge^{59a}, P. Kluit¹⁰⁸, S. Kluth¹⁰², J. Knapik⁴⁰, E. Kneringer⁶³, E.B.F.G. Knoop⁸⁶, A. Knue⁵⁴, A. Kobayashi¹⁵⁶, D. Kobayashi¹⁵⁸, T. Kobayashi¹⁵⁶, M. Kobel⁴⁵, M. Kocian¹⁴⁴, P. Kodys¹³⁰, T. Koffas³⁰, E. Koffeman¹⁰⁸, L.A. Kogan¹²¹, S. Kohlmann¹⁷⁵, Z. Kohout¹²⁹, T. Kohriki⁶⁷, T. Koi¹⁴⁴, H. Kolanoski¹⁶, M. Kolb^{59b}, I. Koletsou⁵, A.A. Komar^{97,*}, Y. Komori¹⁵⁶, T. Kondo⁶⁷, N. Kondrashova⁴³, K. Köneke⁴⁹, A.C. König¹⁰⁷, T. Kono^{67,x}, R. Konoplich^{111,y}, N. Konstantinidis⁷⁹, R. Kopeliansky¹⁵³, S. Koperny^{39a}, L. Köpke⁸⁴, A.K. Kopp⁴⁹, K. Korcyl⁴⁰, K. Kordas¹⁵⁵, A. Korn⁷⁹, A.A. Korol^{110,c}, I. Korolkov¹², E.V. Korolkova¹⁴⁰, O. Kortner¹⁰², S. Kortner¹⁰², T. Kosek¹³⁰, V.V. Kostyukhin²², V.M. Kotov⁶⁶, A. Kotwal⁴⁶, A. Kourkoumeli-Charalampidi¹⁵⁵, C. Kourkoumelis⁹, V. Kouskoura²⁶, A. Koutsman^{160a}, R. Kowalewski¹⁶⁹, T.Z. Kowalski^{39a}, W. Kozanecki¹³⁷, A.S. Kozhin¹³¹, V.A. Kramarenko¹⁰⁰, G. Kramberger⁷⁶, D. Krasnopevtsev⁹⁹, M.W. Krasny⁸¹, A. Krasznahorkay³¹, J.K. Kraus²², A. Kravchenko²⁶, S. Kreiss¹¹¹, M. Kretz^{59c}, J. Kretzschmar⁷⁵, K. Kreutzfeldt⁵³, P. Krieger¹⁵⁹, K. Krizka³², K. Kroeninger⁴⁴, H. Kroha¹⁰², J. Kroll¹²³, J. Kroseberg²², J. Krstic¹³, U. Kruchonak⁶⁶, H. Krüger²², N. Krumnack⁶⁵, A. Kruse¹⁷³, M.C. Kruse⁴⁶, M. Kruskal²³, T. Kubota⁸⁹, H. Kucuk⁷⁹, S. Kuday^{4b}, S. Kuehn⁴⁹, A. Kugel^{59c}, F. Kuger¹⁷⁴, A. Kuhl¹³⁸, T. Kuhl⁴³, V. Kukhtin⁶⁶, R. Kukla¹³⁷, Y. Kulchitsky⁹³, S. Kuleshov^{33b}, M. Kuna^{133a,133b}, T. Kunigo⁶⁹, A. Kupco¹²⁸, H. Kurashige⁶⁸, Y.A. Kurochkin⁹³, V. Kus¹²⁸, E.S. Kuwertz¹⁶⁹, M. Kuze¹⁵⁸, J. Kvita¹¹⁶, T. Kwan¹⁶⁹, D. Kyriazopoulos¹⁴⁰, A. La Rosa¹³⁸, J.L. La Rosa Navarro^{25d}, L. La Rotonda^{38a,38b}, C. Lacasta¹⁶⁷, F. Lacava^{133a,133b}, J. Lacey³⁰, H. Lacker¹⁶, D. Lacour⁸¹, V.R. Lacuesta¹⁶⁷, E. Ladygin⁶⁶, R. Lafaye⁵, B. Laforge⁸¹, T. Lagouri¹⁷⁶, S. Lai⁵⁵, L. Lambourne⁷⁹, S. Lammers⁶², C.L. Lampen⁷, W. Lampl⁷, E. Lançon¹³⁷, U. Landgraf⁴⁹, M.P.J. Landon⁷⁷, V.S. Lang^{59a}, J.C. Lange¹², A.J. Lankford¹⁶³, F. Lanni²⁶, K. Lantzsck²², A. Lanza^{122a}, S. Laplace⁸¹, C. Lapoire³¹, J.F. Laporte¹³⁷, T. Lari^{92a}, F. Lasagni Manghi^{21a,21b}, M. Lassnig³¹, P. Laurelli⁴⁸, W. Lavrijsen¹⁵, A.T. Law¹³⁸, P. Laycock⁷⁵, T. Lazovich⁵⁸, O. Le Dortz⁸¹, E. Le Guirriec⁸⁶, E. Le Menedeu¹², M. LeBlanc¹⁶⁹, T. LeCompte⁶, F. Ledroit-Guillon⁵⁶, C.A. Lee^{146a}, S.C. Lee¹⁵², L. Lee¹, G. Lefebvre⁸¹, M. Lefebvre¹⁶⁹, F. Legger¹⁰¹, C. Leggett¹⁵, A. Lehan⁷⁵, G. Lehmann Miotto³¹, X. Lei⁷, W.A. Leight³⁰, A. Leisos^{155,z}, A.G. Leister¹⁷⁶,

M.A.L. Leite^{25d}, R. Leitner¹³⁰, D. Lellouch¹⁷², B. Lemmer⁵⁵, K.J.C. Leney⁷⁹, T. Lenz²², B. Lenzi³¹,
R. Leone⁷, S. Leone^{125a,125b}, C. Leonidopoulos⁴⁷, S. Leontsinis¹⁰, C. Leroy⁹⁶, C.G. Lester²⁹,
M. Levchenko¹²⁴, J. Levêque⁵, D. Levin⁹⁰, L.J. Levinson¹⁷², M. Levy¹⁸, A. Lewis¹²¹, A.M. Leyko²²,
M. Leyton⁴², B. Li^{34b,aa}, H. Li¹⁴⁹, H.L. Li³², L. Li⁴⁶, L. Li^{34e}, S. Li⁴⁶, X. Li⁸⁵, Y. Li^{34c,ab}, Z. Liang¹³⁸,
H. Liao³⁵, B. Liberti^{134a}, A. Liblong¹⁵⁹, P. Lichard³¹, K. Lie¹⁶⁶, J. Liebal²², W. Liebig¹⁴, C. Limbach²²,
A. Limosani¹⁵¹, S.C. Lin^{152,ac}, T.H. Lin⁸⁴, F. Linde¹⁰⁸, B.E. Lindquist¹⁴⁹, J.T. Linnemann⁹¹,
E. Lipeles¹²³, A. Lipniacka¹⁴, M. Lisovyi^{59b}, T.M. Liss¹⁶⁶, D. Lissauer²⁶, A. Lister¹⁶⁸, A.M. Litke¹³⁸,
B. Liu^{152,ad}, D. Liu¹⁵², H. Liu⁹⁰, J. Liu⁸⁶, J.B. Liu^{34b}, K. Liu⁸⁶, L. Liu¹⁶⁶, M. Liu⁴⁶, M. Liu^{34b}, Y. Liu^{34b},
M. Livan^{122a,122b}, A. Lleres⁵⁶, J. Llorente Merino⁸³, S.L. Lloyd⁷⁷, F. Lo Sterzo¹⁵², E. Lobodzinska⁴³,
P. Loch⁷, W.S. Lockman¹³⁸, F.K. Loebinger⁸⁵, A.E. Loevschall-Jensen³⁷, K.M. Loew²⁴, A. Loginov¹⁷⁶,
T. Lohse¹⁶, K. Lohwasser⁴³, M. Lokajicek¹²⁸, B.A. Long²³, J.D. Long¹⁶⁶, R.E. Long⁷³, K.A. Looper¹¹²,
L. Lopes^{127a}, D. Lopez Mateos⁵⁸, B. Lopez Paredes¹⁴⁰, I. Lopez Paz¹², J. Lorenz¹⁰¹,
N. Lorenzo Martinez⁶², M. Losada²⁰, P.J. Lösel¹⁰¹, X. Lou^{34a}, A. Lounis¹¹⁸, J. Love⁶, P.A. Love⁷³,
H. Lu^{61a}, N. Lu⁹⁰, H.J. Lubatti¹³⁹, C. Luci^{133a,133b}, A. Lucotte⁵⁶, C. Luedtke⁴⁹, F. Luehring⁶²,
W. Lukas⁶³, L. Luminari^{133a}, O. Lundberg^{147a,147b}, B. Lund-Jensen¹⁴⁸, D. Lynn²⁶, R. Lysak¹²⁸,
E. Lytken⁸², H. Ma²⁶, L.L. Ma^{34d}, G. Maccarrone⁴⁸, A. Macchiolo¹⁰², C.M. Macdonald¹⁴⁰, B. Maček⁷⁶,
J. Machado Miguens^{123,127b}, D. Macina³¹, D. Madaffari⁸⁶, R. Madar³⁵, H.J. Maddocks⁷³, W.F. Mader⁴⁵,
A. Madsen¹⁶⁵, J. Maeda⁶⁸, S. Maeland¹⁴, T. Maeno²⁶, A. Maeviskiy¹⁰⁰, E. Magradze⁵⁵, K. Mahboubi⁴⁹,
J. Mahlstedt¹⁰⁸, C. Maiani¹³⁷, C. Maidantchik^{25a}, A.A. Maier¹⁰², T. Maier¹⁰¹, A. Maio^{127a,127b,127d},
S. Majewski¹¹⁷, Y. Makida⁶⁷, N. Makovec¹¹⁸, B. Malaescu⁸¹, Pa. Malecki⁴⁰, V.P. Maleev¹²⁴, F. Malek⁵⁶,
U. Mallik⁶⁴, D. Malon⁶, C. Malone¹⁴⁴, S. Maltezos¹⁰, V.M. Malyshev¹¹⁰, S. Malyukov³¹, J. Mamuzic⁴³,
G. Mancini⁴⁸, B. Mandelli³¹, L. Mandelli^{92a}, I. Mandić⁷⁶, R. Mandrysch⁶⁴, J. Maneira^{127a,127b},
A. Manfredini¹⁰², L. Manhaes de Andrade Filho^{25b}, J. Manjarres Ramos^{160b}, A. Mann¹⁰¹,
A. Manousakis-Katsikakis⁹, B. Mansoulie¹³⁷, R. Mantifel⁸⁸, M. Mantoani⁵⁵, L. Mapelli³¹, L. March^{146c},
G. Marchiori⁸¹, M. Marcisovsky¹²⁸, C.P. Marino¹⁶⁹, M. Marjanovic¹³, D.E. Marley⁹⁰, F. Marroquim^{25a},
S.P. Marsden⁸⁵, Z. Marshall¹⁵, L.F. Marti¹⁷, S. Marti-Garcia¹⁶⁷, B. Martin⁹¹, T.A. Martin¹⁷⁰,
V.J. Martin⁴⁷, B. Martin dit Latour¹⁴, M. Martinez^{12,p}, S. Martin-Haugh¹³², V.S. Martoiu^{27b},
A.C. Martyniuk⁷⁹, M. Marx¹³⁹, F. Marzano^{133a}, A. Marzin³¹, L. Masetti⁸⁴, T. Mashimo¹⁵⁶,
R. Mashinistov⁹⁷, J. Masik⁸⁵, A.L. Maslennikov^{110,c}, I. Massa^{21a,21b}, L. Massa^{21a,21b}, P. Mastrandrea⁵,
A. Mastroberardino^{38a,38b}, T. Masubuchi¹⁵⁶, P. Mättig¹⁷⁵, J. Mattmann⁸⁴, J. Maurer^{27b}, S.J. Maxfield⁷⁵,
D.A. Maximov^{110,c}, R. Mazini¹⁵², S.M. Mazza^{92a,92b}, G. Mc Goldrick¹⁵⁹, S.P. Mc Kee⁹⁰, A. McCarn⁹⁰,
R.L. McCarthy¹⁴⁹, T.G. McCarthy³⁰, N.A. McCubbin¹³², K.W. McFarlane^{57,*}, J.A. McFayden⁷⁹,
G. Mchedlidze⁵⁵, S.J. McMahon¹³², R.A. McPherson^{169,l}, M. Medinnis⁴³, S. Meehan^{146a},
S. Mehlhase¹⁰¹, A. Mehta⁷⁵, K. Meier^{59a}, C. Meineck¹⁰¹, B. Meirose⁴², B.R. Mellado Garcia^{146c},
F. Meloni¹⁷, A. Mengarelli^{21a,21b}, S. Menke¹⁰², E. Meoni¹⁶², K.M. Mercurio⁵⁸, S. Mergelmeyer²²,
P. Mermod⁵⁰, L. Merola^{105a,105b}, C. Meroni^{92a}, F.S. Merritt³², A. Messina^{133a,133b}, J. Metcalfe²⁶,
A.S. Mete¹⁶³, C. Meyer⁸⁴, C. Meyer¹²³, J-P. Meyer¹³⁷, J. Meyer¹⁰⁸, H. Meyer Zu Theenhausen^{59a},
R.P. Middleton¹³², S. Miglioranzi^{164a,164c}, L. Mijović²², G. Mikenberg¹⁷², M. Mikestikova¹²⁸,
M. Mikuž⁷⁶, M. Milesi⁸⁹, A. Milic³¹, D.W. Miller³², C. Mills⁴⁷, A. Milov¹⁷², D.A. Milstead^{147a,147b},
A.A. Minaenko¹³¹, Y. Minami¹⁵⁶, I.A. Minashvili⁶⁶, A.I. Mincer¹¹¹, B. Mindur^{39a}, M. Mineev⁶⁶,
Y. Ming¹⁷³, L.M. Mir¹², K.P. Mistry¹²³, T. Mitani¹⁷¹, J. Mitrevski¹⁰¹, V.A. Mitsou¹⁶⁷, A. Miucci⁵⁰,
P.S. Miyagawa¹⁴⁰, J.U. Mjörnmark⁸², T. Moa^{147a,147b}, K. Mochizuki⁸⁶, S. Mohapatra³⁶, W. Mohr⁴⁹,
S. Molander^{147a,147b}, R. Moles-Valls²², R. Monden⁶⁹, K. Mönig⁴³, C. Monini⁵⁶, J. Monk³⁷,
E. Monnier⁸⁶, A. Montalbano¹⁴⁹, J. Montejo Berlingen¹², F. Monticelli⁷², S. Monzani^{133a,133b},
R.W. Moore³, N. Morange¹¹⁸, D. Moreno²⁰, M. Moreno Llácer⁵⁵, P. Morettini^{51a}, D. Mori¹⁴³,
T. Mori¹⁵⁶, M. Morii⁵⁸, M. Morinaga¹⁵⁶, V. Morisbak¹²⁰, S. Moritz⁸⁴, A.K. Morley¹⁵¹, G. Mornacchi³¹,
J.D. Morris⁷⁷, S.S. Mortensen³⁷, A. Morton⁵⁴, L. Morvaj¹⁰⁴, M. Mosidze^{52b}, J. Moss¹⁴⁴,

K. Motohashi¹⁵⁸, R. Mount¹⁴⁴, E. Mountricha²⁶, S.V. Mouraviev^{97,*}, E.J.W. Moyse⁸⁷, S. Muanza⁸⁶,
 R.D. Mudd¹⁸, F. Mueller¹⁰², J. Mueller¹²⁶, R.S.P. Mueller¹⁰¹, T. Mueller²⁹, D. Muenstermann⁵⁰,
 P. Mullen⁵⁴, G.A. Mullier¹⁷, J.A. Murillo Quijada¹⁸, W.J. Murray^{170,132}, H. Musheghyan⁵⁵, E. Musto¹⁵³,
 A.G. Myagkov^{131,ae}, M. Myska¹²⁹, B.P. Nachman¹⁴⁴, O. Nackenhorst⁵⁵, J. Nadal⁵⁵, K. Nagai¹²¹,
 R. Nagai¹⁵⁸, Y. Nagai⁸⁶, K. Nagano⁶⁷, A. Nagarkar¹¹², Y. Nagasaka⁶⁰, K. Nagata¹⁶¹, M. Nagel¹⁰²,
 E. Nagy⁸⁶, A.M. Nairz³¹, Y. Nakahama³¹, K. Nakamura⁶⁷, T. Nakamura¹⁵⁶, I. Nakano¹¹³,
 H. Namasivayam⁴², R.F. Naranjo Garcia⁴³, R. Narayan³², D.I. Narrias Villar^{59a}, T. Naumann⁴³,
 G. Navarro²⁰, R. Nayyar⁷, H.A. Neal⁹⁰, P.Yu. Nechaeva⁹⁷, T.J. Neep⁸⁵, P.D. Nef¹⁴⁴, A. Negri^{122a,122b},
 M. Negrini^{21a}, S. Nektarijevic¹⁰⁷, C. Nellist¹¹⁸, A. Nelson¹⁶³, S. Nemecek¹²⁸, P. Nemethy¹¹¹,
 A.A. Nepomuceno^{25a}, M. Nessi^{31,af}, M.S. Neubauer¹⁶⁶, M. Neumann¹⁷⁵, R.M. Neves¹¹¹, P. Nevski²⁶,
 P.R. Newman¹⁸, D.H. Nguyen⁶, R.B. Nickerson¹²¹, R. Nicolaidou¹³⁷, B. Nicquevert³¹, J. Nielsen¹³⁸,
 N. Nikiforou³⁶, A. Nikiforov¹⁶, V. Nikolaenko^{131,ae}, I. Nikolic-Audit⁸¹, K. Nikolopoulos¹⁸,
 J.K. Nilsen¹²⁰, P. Nilsson²⁶, Y. Ninomiya¹⁵⁶, A. Nisati^{133a}, R. Nisius¹⁰², T. Nobe¹⁵⁶, L. Nodulman⁶,
 M. Nomachi¹¹⁹, I. Nomidis³⁰, T. Nooney⁷⁷, S. Norberg¹¹⁴, M. Nordberg³¹, O. Novgorodova⁴⁵,
 S. Nowak¹⁰², M. Nozaki⁶⁷, L. Nozka¹¹⁶, K. Ntekas¹⁰, G. Nunes Hanninger⁸⁹, T. Nunnemann¹⁰¹,
 E. Nurse⁷⁹, F. Nuti⁸⁹, B.J. O'Brien⁴⁷, F. O'grady⁷, D.C. O'Neil¹⁴³, V. O'Shea⁵⁴, F.G. Oakham^{30,d},
 H. Oberlack¹⁰², T. Obermann²², J. Ocariz⁸¹, A. Ochi⁶⁸, I. Ochoa³⁶, J.P. Ochoa-Ricoux^{33a}, S. Oda⁷¹,
 S. Odaka⁶⁷, H. Ogren⁶², A. Oh⁸⁵, S.H. Oh⁴⁶, C.C. Ohm¹⁵, H. Ohman¹⁶⁵, H. Oide³¹, W. Okamura¹¹⁹,
 H. Okawa¹⁶¹, Y. Okumura³², T. Okuyama⁶⁷, A. Olariu^{27b}, S.A. Olivares Pino⁴⁷, D. Oliveira Damazio²⁶,
 A. Olszewski⁴⁰, J. Olszowska⁴⁰, A. Onofre^{127a,127e}, K. Onogi¹⁰⁴, P.U.E. Onyisi^{32,t}, C.J. Oram^{160a},
 M.J. Oreglia³², Y. Oren¹⁵⁴, D. Orestano^{135a,135b}, N. Orlando¹⁵⁵, C. Oropeza Barrera⁵⁴, R.S. Orr¹⁵⁹,
 B. Osculati^{51a,51b}, R. Ospanov⁸⁵, G. Otero y Garzon²⁸, H. Otono⁷¹, M. Ouchrif^{136d}, F. Ould-Saada¹²⁰,
 A. Ouraou¹³⁷, K.P. Oussoren¹⁰⁸, Q. Ouyang^{34a}, A. Ovcharova¹⁵, M. Owen⁵⁴, R.E. Owen¹⁸,
 V.E. Ozcan^{19a}, N. Ozturk⁸, K. Pachal¹⁴³, A. Pacheco Pages¹², C. Padilla Aranda¹², M. Pagáčová⁴⁹,
 S. Pagan Griso¹⁵, E. Paganis¹⁴⁰, F. Paige²⁶, P. Pais⁸⁷, K. Pajchel¹²⁰, G. Palacino^{160b}, S. Palestini³¹,
 M. Palka^{39b}, D. Pallin³⁵, A. Palma^{127a,127b}, Y.B. Pan¹⁷³, E.St. Panagiotopoulou¹⁰, C.E. Pandini⁸¹,
 J.G. Panduro Vazquez⁷⁸, P. Pani^{147a,147b}, S. Panitkin²⁶, D. Pantea^{27b}, L. Paolozzi⁵⁰,
 Th.D. Papadopoulou¹⁰, K. Papageorgiou¹⁵⁵, A. Paramonov⁶, D. Paredes Hernandez¹⁵⁵, M.A. Parker²⁹,
 K.A. Parker¹⁴⁰, F. Parodi^{51a,51b}, J.A. Parsons³⁶, U. Parzefall⁴⁹, E. Pasqualucci^{133a}, S. Passaggio^{51a},
 F. Pastore^{135a,135b,*}, Fr. Pastore⁷⁸, G. Pásztor³⁰, S. Pataraiia¹⁷⁵, N.D. Patel¹⁵¹, J.R. Pater⁸⁵, T. Pauly³¹,
 J. Pearce¹⁶⁹, B. Pearson¹¹⁴, L.E. Pedersen³⁷, M. Pedersen¹²⁰, S. Pedraza Lopez¹⁶⁷, R. Pedro^{127a,127b},
 S.V. Peleganchuk^{110,c}, D. Pelikan¹⁶⁵, O. Penc¹²⁸, C. Peng^{34a}, H. Peng^{34b}, B. Penning³², J. Penwell⁶²,
 D.V. Perepelitsa²⁶, E. Perez Codina^{160a}, M.T. Pérez García-Estañ¹⁶⁷, L. Perini^{92a,92b}, H. Pernegger³¹,
 S. Perrella^{105a,105b}, R. Peschke⁴³, V.D. Peshekhonov⁶⁶, K. Peters³¹, R.F.Y. Peters⁸⁵, B.A. Petersen³¹,
 T.C. Petersen³⁷, E. Petit⁴³, A. Petridis¹, C. Petridou¹⁵⁵, P. Petroff¹¹⁸, E. Petrolu^{133a}, F. Petrucci^{135a,135b},
 N.E. Pettersson¹⁵⁸, R. Pezoa^{33b}, P.W. Phillips¹³², G. Piacquadio¹⁴⁴, E. Pianori¹⁷⁰, A. Picazio⁵⁰,
 E. Piccaro⁷⁷, M. Piccinini^{21a,21b}, M.A. Pickering¹²¹, R. Piegaia²⁸, D.T. Pignotti¹¹², J.E. Pilcher³²,
 A.D. Pilkington⁸⁵, A.W.J. Pin⁸⁵, J. Pina^{127a,127b,127d}, M. Pinamonti^{164a,164c,ag}, J.L. Pinfold³, A. Pingel³⁷,
 S. Pires⁸¹, H. Pirumov⁴³, M. Pitt¹⁷², C. Pizio^{92a,92b}, L. Plazak^{145a}, M.-A. Pleier²⁶, V. Pleskot¹³⁰,
 E. Plotnikova⁶⁶, P. Plucinski^{147a,147b}, D. Pluth⁶⁵, R. Poettgen^{147a,147b}, L. Poggioli¹¹⁸, D. Pohl²²,
 G. Polesello^{122a}, A. Poley⁴³, A. Policicchio^{38a,38b}, R. Polifka¹⁵⁹, A. Polini^{21a}, C.S. Pollard⁵⁴,
 V. Polychronakos²⁶, K. Pommès³¹, L. Pontecorvo^{133a}, B.G. Pope⁹¹, G.A. Popeneciu^{27c}, D.S. Popovic¹³,
 A. Poppleton³¹, S. Pospisil¹²⁹, K. Potamianos¹⁵, I.N. Potrap⁶⁶, C.J. Potter¹⁵⁰, C.T. Potter¹¹⁷,
 G. Poulard³¹, J. Poveda³¹, V. Pozdnyakov⁶⁶, P. Pralavorio⁸⁶, A. Pranko¹⁵, S. Prasad³¹, S. Prell⁶⁵,
 D. Price⁸⁵, L.E. Price⁶, M. Primavera^{74a}, S. Prince⁸⁸, M. Proissl⁴⁷, K. Prokofiev^{61c}, F. Prokoshin^{33b},
 E. Protopapadaki¹³⁷, S. Protopopescu²⁶, J. Proudfoot⁶, M. Przybycien^{39a}, E. Ptacek¹¹⁷,
 D. Puddu^{135a,135b}, E. Pueschel⁸⁷, D. Poldon¹⁴⁹, M. Purohit^{26,ah}, P. Puzo¹¹⁸, J. Qian⁹⁰, G. Qin⁵⁴, Y. Qin⁸⁵,

A. Quadt⁵⁵, D.R. Quarrie¹⁵, W.B. Quayle^{164a,164b}, M. Queitsch-Maitland⁸⁵, D. Quilty⁵⁴, S. Raddum¹²⁰,
 V. Radeka²⁶, V. Radescu⁴³, S.K. Radhakrishnan¹⁴⁹, P. Radloff¹¹⁷, P. Rados⁸⁹, F. Ragusa^{92a,92b},
 G. Rahal¹⁷⁸, S. Rajagopalan²⁶, M. Rammensee³¹, C. Rangel-Smith¹⁶⁵, F. Rauscher¹⁰¹, S. Rave⁸⁴,
 T. Ravenscroft⁵⁴, M. Raymond³¹, A.L. Read¹²⁰, N.P. Readioff⁷⁵, D.M. Rebutzi^{122a,122b},
 A. Redelbach¹⁷⁴, G. Redlinger²⁶, R. Reece¹³⁸, K. Reeves⁴², L. Rehnisch¹⁶, J. Reichert¹²³, H. Reisin²⁸,
 C. Rembser³¹, H. Ren^{34a}, A. Renaud¹¹⁸, M. Rescigno^{133a}, S. Resconi^{92a}, O.L. Rezanova^{110,c},
 P. Reznicek¹³⁰, R. Rezvani⁹⁶, R. Richter¹⁰², S. Richter⁷⁹, E. Richter-Was^{39b}, O. Ricken²², M. Ridel⁸¹,
 P. Rieck¹⁶, C.J. Riegel¹⁷⁵, J. Rieger⁵⁵, O. Rifki¹¹⁴, M. Rijssenbeek¹⁴⁹, A. Rimoldi^{122a,122b}, L. Rinaldi^{21a},
 B. Ristić⁵⁰, E. Ritsch³¹, I. Riu¹², F. Rizatdinova¹¹⁵, E. Rizvi⁷⁷, S.H. Robertson^{88,l},
 A. Robichaud-Veronneau⁸⁸, D. Robinson²⁹, J.E.M. Robinson⁴³, A. Robson⁵⁴, C. Roda^{125a,125b}, S. Roe³¹,
 O. Røhne¹²⁰, S. Rolli¹⁶², A. Romaniouk⁹⁹, M. Romano^{21a,21b}, S.M. Romano Saez³⁵,
 E. Romero Adam¹⁶⁷, N. Rompotis¹³⁹, M. Ronzani⁴⁹, L. Roos⁸¹, E. Ros¹⁶⁷, S. Rosati^{133a}, K. Rosbach⁴⁹,
 P. Rose¹³⁸, P.L. Rosendahl¹⁴, O. Rosenthal¹⁴², V. Rossetti^{147a,147b}, E. Rossi^{105a,105b}, L.P. Rossi^{51a},
 J.H.N. Rosten²⁹, R. Rosten¹³⁹, M. Rotaru^{27b}, I. Roth¹⁷², J. Rothberg¹³⁹, D. Rousseau¹¹⁸, C.R. Royon¹³⁷,
 A. Rozanov⁸⁶, Y. Rozen¹⁵³, X. Ruan^{146c}, F. Rubbo¹⁴⁴, I. Rubinskiy⁴³, V.I. Rud¹⁰⁰, C. Rudolph⁴⁵,
 M.S. Rudolph¹⁵⁹, F. Rühr⁴⁹, A. Ruiz-Martinez³¹, Z. Rurikova⁴⁹, N.A. Rusakovich⁶⁶, A. Ruschke¹⁰¹,
 H.L. Russell¹³⁹, J.P. Rutherford⁷, N. Ruthmann³¹, Y.F. Ryabov¹²⁴, M. Rybar¹⁶⁶, G. Rybkin¹¹⁸,
 N.C. Ryder¹²¹, A. Ryzhov¹³¹, A.F. Saavedra¹⁵¹, G. Sabato¹⁰⁸, S. Sacerdoti²⁸, A. Saddique³,
 H.F.W. Sadrozinski¹³⁸, R. Sadykov⁶⁶, F. Safai Tehrani^{133a}, P. Saha¹⁰⁹, M. Sahinsoy^{59a}, M. Saimpert¹³⁷,
 T. Saito¹⁵⁶, H. Sakamoto¹⁵⁶, Y. Sakurai¹⁷¹, G. Salamanna^{135a,135b}, A. Salamon^{134a},
 J.E. Salazar Loyola^{33b}, M. Saleem¹¹⁴, D. Salek¹⁰⁸, P.H. Sales De Bruin¹³⁹, D. Salihagic¹⁰²,
 A. Salnikov¹⁴⁴, J. Salt¹⁶⁷, D. Salvatore^{38a,38b}, F. Salvatore¹⁵⁰, A. Salvucci^{61a}, A. Salzburger³¹,
 D. Sammel⁴⁹, D. Sampsonidis¹⁵⁵, A. Sanchez^{105a,105b}, J. Sánchez¹⁶⁷, V. Sanchez Martinez¹⁶⁷,
 H. Sandaker¹²⁰, R.L. Sandbach⁷⁷, H.G. Sander⁸⁴, M.P. Sanders¹⁰¹, M. Sandhoff¹⁷⁵, C. Sandoval²⁰,
 R. Sandstroem¹⁰², D.P.C. Sankey¹³², M. Sannino^{51a,51b}, A. Sansoni⁴⁸, C. Santoni³⁵,
 R. Santonico^{134a,134b}, H. Santos^{127a}, I. Santoyo Castillo¹⁵⁰, K. Sapp¹²⁶, A. Saponov⁶⁶,
 J.G. Saraiva^{127a,127d}, B. Sarrazin²², O. Sasaki⁶⁷, Y. Sasaki¹⁵⁶, K. Sato¹⁶¹, G. Sauvage^{5,*}, E. Sauvan⁵,
 G. Savage⁷⁸, P. Savard^{159,d}, C. Sawyer¹³², L. Sawyer^{80,o}, J. Saxon³², C. Sbarra^{21a}, A. Sbrizzi^{21a,21b},
 T. Scanlon⁷⁹, D.A. Scannicchio¹⁶³, M. Scarcella¹⁵¹, V. Scarfone^{38a,38b}, J. Schaarschmidt¹⁷²,
 P. Schacht¹⁰², D. Schaefer³¹, R. Schaefer⁴³, J. Schaeffer⁸⁴, S. Schaepe²², S. Schaezel^{59b}, U. Schäfer⁸⁴,
 A.C. Schaffer¹¹⁸, D. Schaile¹⁰¹, R.D. Schamberger¹⁴⁹, V. Scharf^{59a}, V.A. Schegelsky¹²⁴, D. Scheirich¹³⁰,
 M. Schernau¹⁶³, C. Schiavi^{51a,51b}, C. Schillo⁴⁹, M. Schioppa^{38a,38b}, S. Schlenker³¹, K. Schmieden³¹,
 C. Schmitt⁸⁴, S. Schmitt^{59b}, S. Schmitt⁴³, B. Schneider^{160a}, Y.J. Schnellbach⁷⁵, U. Schnoor⁴⁵,
 L. Schoeffel¹³⁷, A. Schoening^{59b}, B.D. Schoenrock⁹¹, E. Schopf²², A.L.S. Schorlemmer⁵⁵, M. Schott⁸⁴,
 D. Schouten^{160a}, J. Schovancova⁸, S. Schramm⁵⁰, M. Schreyer¹⁷⁴, N. Schuh⁸⁴, M.J. Schultens²²,
 H.-C. Schultz-Coulon^{59a}, H. Schulz¹⁶, M. Schumacher⁴⁹, B.A. Schumm¹³⁸, Ph. Schune¹³⁷,
 C. Schwanenberger⁸⁵, A. Schwartzman¹⁴⁴, T.A. Schwarz⁹⁰, Ph. Schwegler¹⁰², H. Schweiger⁸⁵,
 Ph. Schwemling¹³⁷, R. Schwienhorst⁹¹, J. Schwindling¹³⁷, T. Schwindt²², F.G. Sciacca¹⁷, E. Scifo¹¹⁸,
 G. Sciolla²⁴, F. Scuri^{125a,125b}, F. Scutti²², J. Searcy⁹⁰, G. Sedov⁴³, E. Sedykh¹²⁴, P. Seema²²,
 S.C. Seidel¹⁰⁶, A. Seiden¹³⁸, F. Seifert¹²⁹, J.M. Seixas^{25a}, G. Sekhniaidze^{105a}, K. Sekhon⁹⁰,
 S.J. Sekula⁴¹, D.M. Seliverstov^{124,*}, N. Semprini-Cesari^{21a,21b}, C. Serfon³¹, L. Serin¹¹⁸,
 L. Serkin^{164a,164b}, T. Serre⁸⁶, M. Sessa^{135a,135b}, R. Seuster^{160a}, H. Severini¹¹⁴, T. Sfiligoj⁷⁶, F. Sforza³¹,
 A. Sfyrila³¹, E. Shabalina⁵⁵, M. Shamim¹¹⁷, L.Y. Shan^{34a}, R. Shang¹⁶⁶, J.T. Shank²³, M. Shapiro¹⁵,
 P.B. Shatalov⁹⁸, K. Shaw^{164a,164b}, S.M. Shaw⁸⁵, A. Shcherbakova^{147a,147b}, C.Y. Shehu¹⁵⁰, P. Sherwood⁷⁹,
 L. Shi^{152,ai}, S. Shimizu⁶⁸, C.O. Shimmin¹⁶³, M. Shimojima¹⁰³, M. Shiyakova^{66,aj}, A. Shmeleva⁹⁷,
 D. Shoaleh Saadi⁹⁶, M.J. Shochet³², S. Shojaii^{92a,92b}, S. Shrestha¹¹², E. Shulga⁹⁹, M.A. Shupe⁷,
 S. Shushkevich⁴³, P. Sicho¹²⁸, P.E. Sidebo¹⁴⁸, O. Sidiropoulou¹⁷⁴, D. Sidorov¹¹⁵, A. Sidoti^{21a,21b},

F. Siegert⁴⁵, Dj. Sijacki¹³, J. Silva^{127a,127d}, Y. Silver¹⁵⁴, S.B. Silverstein^{147a}, V. Simak¹²⁹, O. Simard⁵, Lj. Simic¹³, S. Simion¹¹⁸, E. Simioni⁸⁴, B. Simmons⁷⁹, D. Simon³⁵, P. Sinervo¹⁵⁹, N.B. Sinev¹¹⁷, M. Sioli^{21a,21b}, G. Siragusa¹⁷⁴, A.N. Sisakyan^{66,*}, S.Yu. Sivoklov¹⁰⁰, J. Sjölin^{147a,147b}, T.B. Sjurjen¹⁴, M.B. Skinner⁷³, H.P. Skottowe⁵⁸, P. Skubic¹¹⁴, M. Slater¹⁸, T. Slavicek¹²⁹, M. Slawinska¹⁰⁸, K. Sliwa¹⁶², V. Smakhtin¹⁷², B.H. Smart⁴⁷, L. Smestad¹⁴, S.Yu. Smirnov⁹⁹, Y. Smirnov⁹⁹, L.N. Smirnova^{100.ak}, O. Smirnova⁸², M.N.K. Smith³⁶, R.W. Smith³⁶, M. Smizanska⁷³, K. Smolek¹²⁹, A.A. Snesarev⁹⁷, G. Snidero⁷⁷, S. Snyder²⁶, R. Sobie^{169.l}, F. Socher⁴⁵, A. Soffer¹⁵⁴, D.A. Soh^{152.ai}, G. Sokhranyi⁷⁶, C.A. Solans Sanchez³¹, M. Solar¹²⁹, J. Solc¹²⁹, E. Yu. Soldatov⁹⁹, U. Soldevila¹⁶⁷, A.A. Solodkov¹³¹, A. Soloshenko⁶⁶, O.V. Solovyanov¹³¹, V. Solovyev¹²⁴, P. Sommer⁴⁹, H.Y. Song^{34b,aa}, N. Soni¹, A. Sood¹⁵, A. Sopczak¹²⁹, B. Sopko¹²⁹, V. Sopko¹²⁹, V. Sorin¹², D. Sosa^{59b}, M. Sosebee⁸, C.L. Sotiropoulou^{125a,125b}, R. Soualah^{164a,164c}, A.M. Soukharev^{110.c}, D. South⁴³, B.C. Sowden⁷⁸, S. Spagnolo^{74a,74b}, M. Spalla^{125a,125b}, M. Spangenberg¹⁷⁰, M. Spannowsky^{al}, F. Spanò⁷⁸, W.R. Spearman⁵⁸, D. Sperlich¹⁶, F. Spettel¹⁰², R. Spighi^{21a}, G. Spigo³¹, L.A. Spiller⁸⁹, M. Spousta¹³⁰, R.D. St. Denis^{54,*}, A. Stabile^{92a}, S. Staerz⁴⁵, J. Stahlman¹²³, R. Stamen^{59a}, S. Stamm¹⁶, E. Stanecka⁴⁰, R.W. Stanek⁶, C. Stanescu^{135a}, M. Stanescu-Bellu⁴³, M.M. Stanitzki⁴³, S. Stapnes¹²⁰, E.A. Starchenko¹³¹, J. Stark⁵⁶, P. Staroba¹²⁸, P. Starovoitov^{59a}, R. Staszewski⁴⁰, P. Steinberg²⁶, B. Stelzer¹⁴³, H.J. Stelzer³¹, O. Stelzer-Chilton^{160a}, H. Stenzel⁵³, G.A. Stewart⁵⁴, J.A. Stillings²², M.C. Stockton⁸⁸, M. Stoebe⁸⁸, G. Stoica^{27b}, P. Stolte⁵⁵, S. Stonjek¹⁰², A.R. Stradling⁸, A. Straessner⁴⁵, M.E. Stramaglia¹⁷, J. Strandberg¹⁴⁸, S. Strandberg^{147a,147b}, A. Strandlie¹²⁰, E. Strauss¹⁴⁴, M. Strauss¹¹⁴, P. Strizenc^{145b}, R. Ströhmer¹⁷⁴, D.M. Strom¹¹⁷, R. Stroynowski⁴¹, A. Strubig¹⁰⁷, S.A. Stucci¹⁷, B. Stugu¹⁴, N.A. Styles⁴³, D. Su¹⁴⁴, J. Su¹²⁶, R. Subramaniam⁸⁰, A. Succurro¹², S. Suchek^{59a}, Y. Sugaya¹¹⁹, M. Suk¹²⁹, V.V. Sulin⁹⁷, S. Sultansoy^{4c}, T. Sumida⁶⁹, S. Sun⁵⁸, X. Sun^{34a}, J.E. Sundermann⁴⁹, K. Suruliz¹⁵⁰, G. Susinno^{38a,38b}, M.R. Sutton¹⁵⁰, S. Suzuki⁶⁷, M. Svatos¹²⁸, M. Swiatlowski¹⁴⁴, I. Sykora^{145a}, T. Sykora¹³⁰, D. Ta⁴⁹, C. Taccini^{135a,135b}, K. Tackmann⁴³, J. Taenzer¹⁵⁹, A. Taffard¹⁶³, R. Tafirout^{160a}, N. Taiblum¹⁵⁴, H. Takai²⁶, R. Takashima⁷⁰, H. Takeda⁶⁸, T. Takeshita¹⁴¹, Y. Takubo⁶⁷, M. Talby⁸⁶, A.A. Talyshev^{110.c}, J.Y.C. Tam¹⁷⁴, K.G. Tan⁸⁹, J. Tanaka¹⁵⁶, R. Tanaka¹¹⁸, S. Tanaka⁶⁷, B.B. Tannenwald¹¹², N. Tannoury²², S. Tapia Araya^{33b}, S. Tapprogge⁸⁴, S. Tarem¹⁵³, F. Tarrade³⁰, G.F. Tartarelli^{92a}, P. Tas¹³⁰, M. Tasevsky¹²⁸, T. Tashiro⁶⁹, E. Tassi^{38a,38b}, A. Tavares Delgado^{127a,127b}, Y. Tayalati^{136d}, F.E. Taylor⁹⁵, G.N. Taylor⁸⁹, P.T.E. Taylor⁸⁹, W. Taylor^{160b}, F.A. Teischinger³¹, P. Teixeira-Dias⁷⁸, K.K. Temming⁴⁹, D. Temple¹⁴³, H. Ten Kate³¹, P.K. Teng¹⁵², J.J. Teoh¹¹⁹, F. Tepel¹⁷⁵, S. Terada⁶⁷, K. Terashi¹⁵⁶, J. Terron⁸³, S. Terzo¹⁰², M. Testa⁴⁸, R.J. Teuscher^{159.l}, T. Theveneaux-Pelzer³⁵, J.P. Thomas¹⁸, J. Thomas-Wilsker⁷⁸, E.N. Thompson³⁶, P.D. Thompson¹⁸, R.J. Thompson⁸⁵, A.S. Thompson⁵⁴, L.A. Thomsen¹⁷⁶, E. Thomson¹²³, M. Thomson²⁹, R.P. Thun^{90,*}, M.J. Tibbetts¹⁵, R.E. Tisce Torres⁸⁶, V.O. Tikhomirov^{97.am}, Yu.A. Tikhonov^{110.c}, S. Timoshenko⁹⁹, E. Tiouchichine⁸⁶, P. Tipton¹⁷⁶, S. Tisserant⁸⁶, K. Todome¹⁵⁸, T. Todorov^{5,*}, S. Todorova-Nova¹³⁰, J. Tojo⁷¹, S. Tokár^{145a}, K. Tokushuku⁶⁷, K. Tollefson⁹¹, E. Tolley⁵⁸, L. Tomlinson⁸⁵, M. Tomoto¹⁰⁴, L. Tompkins^{144.an}, K. Toms¹⁰⁶, E. Torrence¹¹⁷, H. Torres¹⁴³, E. Torró Pastor¹³⁹, J. Toth^{86.ao}, F. Touchard⁸⁶, D.R. Tovey¹⁴⁰, T. Trefzger¹⁷⁴, L. Tremblet³¹, A. Tricoli³¹, I.M. Trigger^{160a}, S. Trincas-Duvoid⁸¹, M.F. Tripiana¹², W. Trischuk¹⁵⁹, B. Trocme⁵⁶, C. Troncon^{92a}, M. Trottier-McDonald¹⁵, M. Trovatelli¹⁶⁹, L. Truong^{164a,164c}, M. Trzebinski⁴⁰, A. Trzupek⁴⁰, C. Tsarouchas³¹, J.C.-L. Tseng¹²¹, P.V. Tsiarshka⁹³, D. Tsionou¹⁵⁵, G. Tsipolitis¹⁰, N. Tsirintanis⁹, S. Tsiskaridze¹², V. Tsiskaridze⁴⁹, E.G. Tskhadadze^{52a}, K.M. Tsui^{61a}, I.I. Tsukerman⁹⁸, V. Tsulaia¹⁵, S. Tsuno⁶⁷, D. Tsybychev¹⁴⁹, A. Tudorache^{27b}, V. Tudorache^{27b}, A.N. Tuna⁵⁸, S.A. Tupputi^{21a,21b}, S. Turchikhin^{100.ak}, D. Turecek¹²⁹, R. Turra^{92a,92b}, A.J. Turvey⁴¹, P.M. Tuts³⁶, A. Tykhonov⁵⁰, M. Tylmad^{147a,147b}, M. Tyndel¹³², I. Ueda¹⁵⁶, R. Ueno³⁰, M. Ughetto^{147a,147b}, M. Ugland¹⁴, F. Ukegawa¹⁶¹, G. Unal³¹, A. Undrus²⁶, G. Unel¹⁶³, F.C. Ungaro⁴⁹, Y. Unno⁶⁷, C. Unverdorben¹⁰¹, J. Urban^{145b}, P. Urquijo⁸⁹, P. Urrejola⁸⁴, G. Usai⁸, A. Usanova⁶³, L. Vacavant⁸⁶, V. Vacek¹²⁹,

B. Vachon⁸⁸, C. Valderanis⁸⁴, N. Valencic¹⁰⁸, S. Valentinetti^{21a,21b}, A. Valero¹⁶⁷, L. Valery¹², S. Valkar¹³⁰, S. Vallecorsa⁵⁰, J.A. Valls Ferrer¹⁶⁷, W. Van Den Wollenberg¹⁰⁸, P.C. Van Der Deijl¹⁰⁸, R. van der Geer¹⁰⁸, H. van der Graaf¹⁰⁸, N. van Eldik¹⁵³, P. van Gemmeren⁶, J. Van Nieuwkoop¹⁴³, I. van Vulpen¹⁰⁸, M.C. van Woerden³¹, M. Vanadia^{133a,133b}, W. Vandelli³¹, R. Vanguri¹²³, A. Vaniachine⁶, F. Vannucci⁸¹, G. Vardanyan¹⁷⁷, R. Vari^{133a}, E.W. Varnes⁷, T. Varol⁴¹, D. Varouchas⁸¹, A. Vartapetian⁸, K.E. Varvell¹⁵¹, F. Vazeille³⁵, T. Vazquez Schroeder⁸⁸, J. Veatch⁷, L.M. Veloce¹⁵⁹, F. Veloso^{127a,127c}, T. Velz²², S. Veneziano^{133a}, A. Ventura^{74a,74b}, D. Ventura⁸⁷, M. Venturi¹⁶⁹, N. Venturi¹⁵⁹, A. Venturini²⁴, V. Vercesi^{122a}, M. Verducci^{133a,133b}, W. Verkerke¹⁰⁸, J.C. Vermeulen¹⁰⁸, A. Vest^{45,ap}, M.C. Vetterli^{143,d}, O. Viazlo⁸², I. Vichou¹⁶⁶, T. Vickey¹⁴⁰, O.E. Vickey Boeriu¹⁴⁰, G.H.A. Viehhauser¹²¹, S. Viel¹⁵, R. Vigne⁶³, M. Villa^{21a,21b}, M. Villaplana Perez^{92a,92b}, E. Vilucchi⁴⁸, M.G. Vincter³⁰, V.B. Vinogradov⁶⁶, I. Vivarelli¹⁵⁰, F. Vives Vaque³, S. Vlachos¹⁰, D. Vladoiu¹⁰¹, M. Vlasak¹²⁹, M. Vogel^{33a}, P. Vokac¹²⁹, G. Volpi^{125a,125b}, M. Volpi⁸⁹, H. von der Schmitt¹⁰², H. von Radziewski⁴⁹, E. von Toerne²², V. Vorobel¹³⁰, K. Vorobev⁹⁹, M. Vos¹⁶⁷, R. Voss³¹, J.H. Vossebeld⁷⁵, N. Vranjes¹³, M. Vranjes Milosavljevic¹³, V. Vrba¹²⁸, M. Vreeswijk¹⁰⁸, R. Vuillermet³¹, I. Vukotic³², Z. Vykydal¹²⁹, P. Wagner²², W. Wagner¹⁷⁵, H. Wahlberg⁷², S. Wahrmund⁴⁵, J. Wakabayashi¹⁰⁴, J. Walder⁷³, R. Walker¹⁰¹, W. Walkowiak¹⁴², C. Wang¹⁵², F. Wang¹⁷³, H. Wang¹⁵, H. Wang⁴¹, J. Wang⁴³, J. Wang¹⁵¹, K. Wang⁸⁸, R. Wang⁶, S.M. Wang¹⁵², T. Wang²², T. Wang³⁶, X. Wang¹⁷⁶, C. Wanotayaroj¹¹⁷, A. Warburton⁸⁸, C.P. Ward²⁹, D.R. Wardrope⁷⁹, A. Washbrook⁴⁷, C. Wasicki⁴³, P.M. Watkins¹⁸, A.T. Watson¹⁸, I.J. Watson¹⁵¹, M.F. Watson¹⁸, G. Watts¹³⁹, S. Watts⁸⁵, B.M. Waugh⁷⁹, S. Webb⁸⁵, M.S. Weber¹⁷, S.W. Weber¹⁷⁴, J.S. Webster³², A.R. Weidberg¹²¹, B. Weinert⁶², J. Weingarten⁵⁵, C. Weiser⁴⁹, H. Weits¹⁰⁸, P.S. Wells³¹, T. Wenaus²⁶, T. Wengler³¹, S. Wenig³¹, N. Wermes²², M. Werner⁴⁹, P. Werner³¹, M. Wessels^{59a}, J. Wetter¹⁶², K. Whalen¹¹⁷, A.M. Wharton⁷³, A. White⁸, M.J. White¹, R. White^{33b}, S. White^{125a,125b}, D. Whiteson¹⁶³, F.J. Wickens¹³², W. Wiedenmann¹⁷³, M. Wielers¹³², P. Wienemann²², C. Wiglesworth³⁷, L.A.M. Wiik-Fuchs²², A. Wildauer¹⁰², H.G. Wilkens³¹, H.H. Williams¹²³, S. Williams¹⁰⁸, C. Willis⁹¹, S. Willocq⁸⁷, A. Wilson⁹⁰, J.A. Wilson¹⁸, I. Wingerter-Seez⁵, F. Winklmeier¹¹⁷, B.T. Winter²², M. Wittgen¹⁴⁴, J. Wittkowski¹⁰¹, S.J. Wollstadt⁸⁴, M.W. Wolter⁴⁰, H. Wolters^{127a,127c}, B.K. Wosiek⁴⁰, J. Wotschack³¹, M.J. Woudstra⁸⁵, K.W. Wozniak⁴⁰, M. Wu⁵⁶, M. Wu³², S.L. Wu¹⁷³, X. Wu⁵⁰, Y. Wu⁹⁰, T.R. Wyatt⁸⁵, B.M. Wynne⁴⁷, S. Xella³⁷, D. Xu^{34a}, L. Xu²⁶, B. Yabsley¹⁵¹, S. Yacoub^{146a}, R. Yakabe⁶⁸, M. Yamada⁶⁷, D. Yamaguchi¹⁵⁸, Y. Yamaguchi¹¹⁹, A. Yamamoto⁶⁷, S. Yamamoto¹⁵⁶, T. Yamanaka¹⁵⁶, K. Yamauchi¹⁰⁴, Y. Yamazaki⁶⁸, Z. Yan²³, H. Yang^{34e}, H. Yang¹⁷³, Y. Yang¹⁵², W-M. Yao¹⁵, Y.C. Yap⁸¹, Y. Yasu⁶⁷, E. Yatsenko⁵, K.H. Yau Wong²², J. Ye⁴¹, S. Ye²⁶, I. Yeletsikh⁶⁶, A.L. Yen⁵⁸, E. Yildirim⁴³, K. Yorita¹⁷¹, R. Yoshida⁶, K. Yoshihara¹²³, C. Young¹⁴⁴, C.J.S. Young³¹, S. Youssef²³, D.R. Yu¹⁵, J. Yu⁸, J.M. Yu⁹⁰, J. Yu¹¹⁵, L. Yuan⁶⁸, S.P.Y. Yuen²², A. Yurkewicz¹⁰⁹, I. Yusuf^{29,aa}, B. Zabinski⁴⁰, R. Zaidan⁶⁴, A.M. Zaitsev^{131,ae}, J. Zalieckas¹⁴, A. Zaman¹⁴⁹, S. Zambito⁵⁸, L. Zanello^{133a,133b}, D. Zanzi⁸⁹, C. Zeitnitz¹⁷⁵, M. Zeman¹²⁹, A. Zemla^{39a}, Q. Zeng¹⁴⁴, K. Zengel²⁴, O. Zenin¹³¹, T. Ženiš^{145a}, D. Zerwas¹¹⁸, D. Zhang⁹⁰, F. Zhang¹⁷³, G. Zhang^{34b}, H. Zhang^{34c}, J. Zhang⁶, L. Zhang⁴⁹, R. Zhang^{34b,j}, X. Zhang^{34d}, Z. Zhang¹¹⁸, X. Zhao⁴¹, Y. Zhao^{34d,118}, Z. Zhao^{34b}, A. Zhemchugov⁶⁶, J. Zhong¹²¹, B. Zhou⁹⁰, C. Zhou⁴⁶, L. Zhou³⁶, L. Zhou⁴¹, M. Zhou¹⁴⁹, N. Zhou^{34f}, C.G. Zhu^{34d}, H. Zhu^{34a}, J. Zhu⁹⁰, Y. Zhu^{34b}, X. Zhuang^{34a}, K. Zhukov⁹⁷, A. Zibell¹⁷⁴, D. Zieminska⁶², N.I. Zimine⁶⁶, C. Zimmermann⁸⁴, S. Zimmermann⁴⁹, Z. Zinonos⁵⁵, M. Zinser⁸⁴, M. Ziolkowski¹⁴², L. Živković¹³, G. Zobernig¹⁷³, A. Zoccoli^{21a,21b}, M. zur Nedden¹⁶, G. Zurzolo^{105a,105b}, L. Zwalinski³¹.

¹ Department of Physics, University of Adelaide, Adelaide, Australia

² Physics Department, SUNY Albany, Albany NY, United States of America

³ Department of Physics, University of Alberta, Edmonton AB, Canada

⁴ (a) Department of Physics, Ankara University, Ankara; (b) Istanbul Aydin University, Istanbul; (c)

Division of Physics, TOBB University of Economics and Technology, Ankara, Turkey

⁵ LAPP, CNRS/IN2P3 and Université Savoie Mont Blanc, Annecy-le-Vieux, France

⁶ High Energy Physics Division, Argonne National Laboratory, Argonne IL, United States of America

⁷ Department of Physics, University of Arizona, Tucson AZ, United States of America

⁸ Department of Physics, The University of Texas at Arlington, Arlington TX, United States of America

⁹ Physics Department, University of Athens, Athens, Greece

¹⁰ Physics Department, National Technical University of Athens, Zografou, Greece

¹¹ Institute of Physics, Azerbaijan Academy of Sciences, Baku, Azerbaijan

¹² Institut de Física d'Altes Energies (IFAE), The Barcelona Institute of Science and Technology, Barcelona, Spain, Spain

¹³ Institute of Physics, University of Belgrade, Belgrade, Serbia

¹⁴ Department for Physics and Technology, University of Bergen, Bergen, Norway

¹⁵ Physics Division, Lawrence Berkeley National Laboratory and University of California, Berkeley CA, United States of America

¹⁶ Department of Physics, Humboldt University, Berlin, Germany

¹⁷ Albert Einstein Center for Fundamental Physics and Laboratory for High Energy Physics, University of Bern, Bern, Switzerland

¹⁸ School of Physics and Astronomy, University of Birmingham, Birmingham, United Kingdom

¹⁹ ^(a) Department of Physics, Bogazici University, Istanbul; ^(b) Department of Physics Engineering, Gaziantep University, Gaziantep; ^(c) Department of Physics, Dogus University, Istanbul, Turkey

²⁰ Centro de Investigaciones, Universidad Antonio Narino, Bogota, Colombia

²¹ ^(a) INFN Sezione di Bologna; ^(b) Dipartimento di Fisica e Astronomia, Università di Bologna, Bologna, Italy

²² Physikalisches Institut, University of Bonn, Bonn, Germany

²³ Department of Physics, Boston University, Boston MA, United States of America

²⁴ Department of Physics, Brandeis University, Waltham MA, United States of America

²⁵ ^(a) Universidade Federal do Rio De Janeiro COPPE/EE/IF, Rio de Janeiro; ^(b) Electrical Circuits Department, Federal University of Juiz de Fora (UFJF), Juiz de Fora; ^(c) Federal University of Sao Joao del Rei (UFSJ), Sao Joao del Rei; ^(d) Instituto de Física, Universidade de Sao Paulo, Sao Paulo, Brazil

²⁶ Physics Department, Brookhaven National Laboratory, Upton NY, United States of America

²⁷ ^(a) Transilvania University of Brasov, Brasov, Romania; ^(b) National Institute of Physics and Nuclear Engineering, Bucharest; ^(c) National Institute for Research and Development of Isotopic and Molecular Technologies, Physics Department, Cluj Napoca; ^(d) University Politehnica Bucharest, Bucharest; ^(e) West University in Timisoara, Timisoara, Romania

²⁸ Departamento de Física, Universidad de Buenos Aires, Buenos Aires, Argentina

²⁹ Cavendish Laboratory, University of Cambridge, Cambridge, United Kingdom

³⁰ Department of Physics, Carleton University, Ottawa ON, Canada

³¹ CERN, Geneva, Switzerland

³² Enrico Fermi Institute, University of Chicago, Chicago IL, United States of America

³³ ^(a) Departamento de Física, Pontificia Universidad Católica de Chile, Santiago; ^(b) Departamento de Física, Universidad Técnica Federico Santa María, Valparaíso, Chile

³⁴ ^(a) Institute of High Energy Physics, Chinese Academy of Sciences, Beijing; ^(b) Department of Modern Physics, University of Science and Technology of China, Anhui; ^(c) Department of Physics, Nanjing University, Jiangsu; ^(d) School of Physics, Shandong University, Shandong; ^(e) Department of Physics and Astronomy, Shanghai Key Laboratory for Particle Physics and Cosmology, Shanghai Jiao Tong University, Shanghai; (also affiliated with PKU-CHEP); ^(f) Physics Department, Tsinghua University, Beijing 100084, China

- 35 Laboratoire de Physique Corpusculaire, Clermont Université and Université Blaise Pascal and CNRS/IN2P3, Clermont-Ferrand, France
- 36 Nevis Laboratory, Columbia University, Irvington NY, United States of America
- 37 Niels Bohr Institute, University of Copenhagen, Kobenhavn, Denmark
- 38 ^(a) INFN Gruppo Collegato di Cosenza, Laboratori Nazionali di Frascati; ^(b) Dipartimento di Fisica, Università della Calabria, Rende, Italy
- 39 ^(a) AGH University of Science and Technology, Faculty of Physics and Applied Computer Science, Krakow; ^(b) Marian Smoluchowski Institute of Physics, Jagiellonian University, Krakow, Poland
- 40 Institute of Nuclear Physics Polish Academy of Sciences, Krakow, Poland
- 41 Physics Department, Southern Methodist University, Dallas TX, United States of America
- 42 Physics Department, University of Texas at Dallas, Richardson TX, United States of America
- 43 DESY, Hamburg and Zeuthen, Germany
- 44 Institut für Experimentelle Physik IV, Technische Universität Dortmund, Dortmund, Germany
- 45 Institut für Kern- und Teilchenphysik, Technische Universität Dresden, Dresden, Germany
- 46 Department of Physics, Duke University, Durham NC, United States of America
- 47 SUPA - School of Physics and Astronomy, University of Edinburgh, Edinburgh, United Kingdom
- 48 INFN Laboratori Nazionali di Frascati, Frascati, Italy
- 49 Fakultät für Mathematik und Physik, Albert-Ludwigs-Universität, Freiburg, Germany
- 50 Section de Physique, Université de Genève, Geneva, Switzerland
- 51 ^(a) INFN Sezione di Genova; ^(b) Dipartimento di Fisica, Università di Genova, Genova, Italy
- 52 ^(a) E. Andronikashvili Institute of Physics, Iv. Javakhishvili Tbilisi State University, Tbilisi; ^(b) High Energy Physics Institute, Tbilisi State University, Tbilisi, Georgia
- 53 II Physikalisches Institut, Justus-Liebig-Universität Giessen, Giessen, Germany
- 54 SUPA - School of Physics and Astronomy, University of Glasgow, Glasgow, United Kingdom
- 55 II Physikalisches Institut, Georg-August-Universität, Göttingen, Germany
- 56 Laboratoire de Physique Subatomique et de Cosmologie, Université Grenoble-Alpes, CNRS/IN2P3, Grenoble, France
- 57 Department of Physics, Hampton University, Hampton VA, United States of America
- 58 Laboratory for Particle Physics and Cosmology, Harvard University, Cambridge MA, United States of America
- 59 ^(a) Kirchhoff-Institut für Physik, Ruprecht-Karls-Universität Heidelberg, Heidelberg; ^(b) Physikalisches Institut, Ruprecht-Karls-Universität Heidelberg, Heidelberg; ^(c) ZITI Institut für technische Informatik, Ruprecht-Karls-Universität Heidelberg, Mannheim, Germany
- 60 Faculty of Applied Information Science, Hiroshima Institute of Technology, Hiroshima, Japan
- 61 ^(a) Department of Physics, The Chinese University of Hong Kong, Shatin, N.T., Hong Kong; ^(b) Department of Physics, The University of Hong Kong, Hong Kong; ^(c) Department of Physics, The Hong Kong University of Science and Technology, Clear Water Bay, Kowloon, Hong Kong, China
- 62 Department of Physics, Indiana University, Bloomington IN, United States of America
- 63 Institut für Astro- und Teilchenphysik, Leopold-Franzens-Universität, Innsbruck, Austria
- 64 University of Iowa, Iowa City IA, United States of America
- 65 Department of Physics and Astronomy, Iowa State University, Ames IA, United States of America
- 66 Joint Institute for Nuclear Research, JINR Dubna, Dubna, Russia
- 67 KEK, High Energy Accelerator Research Organization, Tsukuba, Japan
- 68 Graduate School of Science, Kobe University, Kobe, Japan
- 69 Faculty of Science, Kyoto University, Kyoto, Japan
- 70 Kyoto University of Education, Kyoto, Japan
- 71 Department of Physics, Kyushu University, Fukuoka, Japan

- ⁷² Instituto de Física La Plata, Universidad Nacional de La Plata and CONICET, La Plata, Argentina
- ⁷³ Physics Department, Lancaster University, Lancaster, United Kingdom
- ⁷⁴ ^(a) INFN Sezione di Lecce; ^(b) Dipartimento di Matematica e Fisica, Università del Salento, Lecce, Italy
- ⁷⁵ Oliver Lodge Laboratory, University of Liverpool, Liverpool, United Kingdom
- ⁷⁶ Department of Physics, Jožef Stefan Institute and University of Ljubljana, Ljubljana, Slovenia
- ⁷⁷ School of Physics and Astronomy, Queen Mary University of London, London, United Kingdom
- ⁷⁸ Department of Physics, Royal Holloway University of London, Surrey, United Kingdom
- ⁷⁹ Department of Physics and Astronomy, University College London, London, United Kingdom
- ⁸⁰ Louisiana Tech University, Ruston LA, United States of America
- ⁸¹ Laboratoire de Physique Nucléaire et de Hautes Energies, UPMC and Université Paris-Diderot and CNRS/IN2P3, Paris, France
- ⁸² Fysiska institutionen, Lunds universitet, Lund, Sweden
- ⁸³ Departamento de Física Teórica C-15, Universidad Autónoma de Madrid, Madrid, Spain
- ⁸⁴ Institut für Physik, Universität Mainz, Mainz, Germany
- ⁸⁵ School of Physics and Astronomy, University of Manchester, Manchester, United Kingdom
- ⁸⁶ CPPM, Aix-Marseille Université and CNRS/IN2P3, Marseille, France
- ⁸⁷ Department of Physics, University of Massachusetts, Amherst MA, United States of America
- ⁸⁸ Department of Physics, McGill University, Montreal QC, Canada
- ⁸⁹ School of Physics, University of Melbourne, Victoria, Australia
- ⁹⁰ Department of Physics, The University of Michigan, Ann Arbor MI, United States of America
- ⁹¹ Department of Physics and Astronomy, Michigan State University, East Lansing MI, United States of America
- ⁹² ^(a) INFN Sezione di Milano; ^(b) Dipartimento di Fisica, Università di Milano, Milano, Italy
- ⁹³ B.I. Stepanov Institute of Physics, National Academy of Sciences of Belarus, Minsk, Republic of Belarus
- ⁹⁴ National Scientific and Educational Centre for Particle and High Energy Physics, Minsk, Republic of Belarus
- ⁹⁵ Department of Physics, Massachusetts Institute of Technology, Cambridge MA, United States of America
- ⁹⁶ Group of Particle Physics, University of Montreal, Montreal QC, Canada
- ⁹⁷ P.N. Lebedev Physical Institute of the Russian Academy of Sciences, Moscow, Russia
- ⁹⁸ Institute for Theoretical and Experimental Physics (ITEP), Moscow, Russia
- ⁹⁹ National Research Nuclear University MEPhI, Moscow, Russia
- ¹⁰⁰ D.V. Skobeltsyn Institute of Nuclear Physics, M.V. Lomonosov Moscow State University, Moscow, Russia
- ¹⁰¹ Fakultät für Physik, Ludwig-Maximilians-Universität München, München, Germany
- ¹⁰² Max-Planck-Institut für Physik (Werner-Heisenberg-Institut), München, Germany
- ¹⁰³ Nagasaki Institute of Applied Science, Nagasaki, Japan
- ¹⁰⁴ Graduate School of Science and Kobayashi-Maskawa Institute, Nagoya University, Nagoya, Japan
- ¹⁰⁵ ^(a) INFN Sezione di Napoli; ^(b) Dipartimento di Fisica, Università di Napoli, Napoli, Italy
- ¹⁰⁶ Department of Physics and Astronomy, University of New Mexico, Albuquerque NM, United States of America
- ¹⁰⁷ Institute for Mathematics, Astrophysics and Particle Physics, Radboud University Nijmegen/Nikhef, Nijmegen, Netherlands
- ¹⁰⁸ Nikhef National Institute for Subatomic Physics and University of Amsterdam, Amsterdam, Netherlands

- ¹⁰⁹ Department of Physics, Northern Illinois University, DeKalb IL, United States of America
- ¹¹⁰ Budker Institute of Nuclear Physics, SB RAS, Novosibirsk, Russia
- ¹¹¹ Department of Physics, New York University, New York NY, United States of America
- ¹¹² Ohio State University, Columbus OH, United States of America
- ¹¹³ Faculty of Science, Okayama University, Okayama, Japan
- ¹¹⁴ Homer L. Dodge Department of Physics and Astronomy, University of Oklahoma, Norman OK, United States of America
- ¹¹⁵ Department of Physics, Oklahoma State University, Stillwater OK, United States of America
- ¹¹⁶ Palacký University, RCPTM, Olomouc, Czech Republic
- ¹¹⁷ Center for High Energy Physics, University of Oregon, Eugene OR, United States of America
- ¹¹⁸ LAL, Univ. Paris-Sud, CNRS/IN2P3, Université Paris-Saclay, Orsay, France
- ¹¹⁹ Graduate School of Science, Osaka University, Osaka, Japan
- ¹²⁰ Department of Physics, University of Oslo, Oslo, Norway
- ¹²¹ Department of Physics, Oxford University, Oxford, United Kingdom
- ¹²² ^(a) INFN Sezione di Pavia; ^(b) Dipartimento di Fisica, Università di Pavia, Pavia, Italy
- ¹²³ Department of Physics, University of Pennsylvania, Philadelphia PA, United States of America
- ¹²⁴ National Research Centre "Kurchatov Institute" B.P.Konstantinov Petersburg Nuclear Physics Institute, St. Petersburg, Russia
- ¹²⁵ ^(a) INFN Sezione di Pisa; ^(b) Dipartimento di Fisica E. Fermi, Università di Pisa, Pisa, Italy
- ¹²⁶ Department of Physics and Astronomy, University of Pittsburgh, Pittsburgh PA, United States of America
- ¹²⁷ ^(a) Laboratório de Instrumentação e Física Experimental de Partículas - LIP, Lisboa; ^(b) Faculdade de Ciências, Universidade de Lisboa, Lisboa; ^(c) Department of Physics, University of Coimbra, Coimbra; ^(d) Centro de Física Nuclear da Universidade de Lisboa, Lisboa; ^(e) Departamento de Física, Universidade do Minho, Braga; ^(f) Departamento de Física Teórica y del Cosmos and CAFPE, Universidad de Granada, Granada (Spain); ^(g) Dep Física and CEFITEC of Faculdade de Ciências e Tecnologia, Universidade Nova de Lisboa, Caparica, Portugal
- ¹²⁸ Institute of Physics, Academy of Sciences of the Czech Republic, Praha, Czech Republic
- ¹²⁹ Czech Technical University in Prague, Praha, Czech Republic
- ¹³⁰ Faculty of Mathematics and Physics, Charles University in Prague, Praha, Czech Republic
- ¹³¹ State Research Center Institute for High Energy Physics (Protvino), NRC KI, Russia
- ¹³² Particle Physics Department, Rutherford Appleton Laboratory, Didcot, United Kingdom
- ¹³³ ^(a) INFN Sezione di Roma; ^(b) Dipartimento di Fisica, Sapienza Università di Roma, Roma, Italy
- ¹³⁴ ^(a) INFN Sezione di Roma Tor Vergata; ^(b) Dipartimento di Fisica, Università di Roma Tor Vergata, Roma, Italy
- ¹³⁵ ^(a) INFN Sezione di Roma Tre; ^(b) Dipartimento di Matematica e Fisica, Università Roma Tre, Roma, Italy
- ¹³⁶ ^(a) Faculté des Sciences Ain Chock, Réseau Universitaire de Physique des Hautes Energies - Université Hassan II, Casablanca; ^(b) Centre National de l'Énergie des Sciences Techniques Nucleaires, Rabat; ^(c) Faculté des Sciences Semlalia, Université Cadi Ayyad, LPHEA-Marrakech; ^(d) Faculté des Sciences, Université Mohamed Premier and LTPM, Oujda; ^(e) Faculté des sciences, Université Mohammed V, Rabat, Morocco
- ¹³⁷ DSM/IRFU (Institut de Recherches sur les Lois Fondamentales de l'Univers), CEA Saclay (Commissariat à l'Énergie Atomique et aux Énergies Alternatives), Gif-sur-Yvette, France
- ¹³⁸ Santa Cruz Institute for Particle Physics, University of California Santa Cruz, Santa Cruz CA, United States of America
- ¹³⁹ Department of Physics, University of Washington, Seattle WA, United States of America

- ¹⁴⁰ Department of Physics and Astronomy, University of Sheffield, Sheffield, United Kingdom
- ¹⁴¹ Department of Physics, Shinshu University, Nagano, Japan
- ¹⁴² Fachbereich Physik, Universität Siegen, Siegen, Germany
- ¹⁴³ Department of Physics, Simon Fraser University, Burnaby BC, Canada
- ¹⁴⁴ SLAC National Accelerator Laboratory, Stanford CA, United States of America
- ¹⁴⁵ ^(a) Faculty of Mathematics, Physics & Informatics, Comenius University, Bratislava; ^(b) Department of Subnuclear Physics, Institute of Experimental Physics of the Slovak Academy of Sciences, Kosice, Slovak Republic
- ¹⁴⁶ ^(a) Department of Physics, University of Cape Town, Cape Town; ^(b) Department of Physics, University of Johannesburg, Johannesburg; ^(c) School of Physics, University of the Witwatersrand, Johannesburg, South Africa
- ¹⁴⁷ ^(a) Department of Physics, Stockholm University; ^(b) The Oskar Klein Centre, Stockholm, Sweden
- ¹⁴⁸ Physics Department, Royal Institute of Technology, Stockholm, Sweden
- ¹⁴⁹ Departments of Physics & Astronomy and Chemistry, Stony Brook University, Stony Brook NY, United States of America
- ¹⁵⁰ Department of Physics and Astronomy, University of Sussex, Brighton, United Kingdom
- ¹⁵¹ School of Physics, University of Sydney, Sydney, Australia
- ¹⁵² Institute of Physics, Academia Sinica, Taipei, Taiwan
- ¹⁵³ Department of Physics, Technion: Israel Institute of Technology, Haifa, Israel
- ¹⁵⁴ Raymond and Beverly Sackler School of Physics and Astronomy, Tel Aviv University, Tel Aviv, Israel
- ¹⁵⁵ Department of Physics, Aristotle University of Thessaloniki, Thessaloniki, Greece
- ¹⁵⁶ International Center for Elementary Particle Physics and Department of Physics, The University of Tokyo, Tokyo, Japan
- ¹⁵⁷ Graduate School of Science and Technology, Tokyo Metropolitan University, Tokyo, Japan
- ¹⁵⁸ Department of Physics, Tokyo Institute of Technology, Tokyo, Japan
- ¹⁵⁹ Department of Physics, University of Toronto, Toronto ON, Canada
- ¹⁶⁰ ^(a) TRIUMF, Vancouver BC; ^(b) Department of Physics and Astronomy, York University, Toronto ON, Canada
- ¹⁶¹ Faculty of Pure and Applied Sciences, and Center for Integrated Research in Fundamental Science and Engineering, University of Tsukuba, Tsukuba, Japan
- ¹⁶² Department of Physics and Astronomy, Tufts University, Medford MA, United States of America
- ¹⁶³ Department of Physics and Astronomy, University of California Irvine, Irvine CA, United States of America
- ¹⁶⁴ ^(a) INFN Gruppo Collegato di Udine, Sezione di Trieste, Udine; ^(b) ICTP, Trieste; ^(c) Dipartimento di Chimica, Fisica e Ambiente, Università di Udine, Udine, Italy
- ¹⁶⁵ Department of Physics and Astronomy, University of Uppsala, Uppsala, Sweden
- ¹⁶⁶ Department of Physics, University of Illinois, Urbana IL, United States of America
- ¹⁶⁷ Instituto de Física Corpuscular (IFIC) and Departamento de Física Atómica, Molecular y Nuclear and Departamento de Ingeniería Electrónica and Instituto de Microelectrónica de Barcelona (IMB-CNM), University of Valencia and CSIC, Valencia, Spain
- ¹⁶⁸ Department of Physics, University of British Columbia, Vancouver BC, Canada
- ¹⁶⁹ Department of Physics and Astronomy, University of Victoria, Victoria BC, Canada
- ¹⁷⁰ Department of Physics, University of Warwick, Coventry, United Kingdom
- ¹⁷¹ Waseda University, Tokyo, Japan
- ¹⁷² Department of Particle Physics, The Weizmann Institute of Science, Rehovot, Israel
- ¹⁷³ Department of Physics, University of Wisconsin, Madison WI, United States of America

- ¹⁷⁴ Fakultät für Physik und Astronomie, Julius-Maximilians-Universität, Würzburg, Germany
- ¹⁷⁵ Fakultät für Mathematik und Naturwissenschaften, Fachgruppe Physik, Bergische Universität Wuppertal, Wuppertal, Germany
- ¹⁷⁶ Department of Physics, Yale University, New Haven CT, United States of America
- ¹⁷⁷ Yerevan Physics Institute, Yerevan, Armenia
- ¹⁷⁸ Centre de Calcul de l'Institut National de Physique Nucléaire et de Physique des Particules (IN2P3), Villeurbanne, France
- ^a Also at Department of Physics, King's College London, London, United Kingdom
- ^b Also at Institute of Physics, Azerbaijan Academy of Sciences, Baku, Azerbaijan
- ^c Also at Novosibirsk State University, Novosibirsk, Russia
- ^d Also at TRIUMF, Vancouver BC, Canada
- ^e Also at Department of Physics, California State University, Fresno CA, United States of America
- ^f Also at Department of Physics, University of Fribourg, Fribourg, Switzerland
- ^g Also at Departament de Física de la Universitat Autònoma de Barcelona, Barcelona, Spain
- ^h Also at Departamento de Física e Astronomia, Faculdade de Ciências, Universidade do Porto, Portugal
- ⁱ Also at Tomsk State University, Tomsk, Russia
- ^j Also at CPPM, Aix-Marseille Université and CNRS/IN2P3, Marseille, France
- ^k Also at Università di Napoli Parthenope, Napoli, Italy
- ^l Also at Institute of Particle Physics (IPP), Canada
- ^m Also at Particle Physics Department, Rutherford Appleton Laboratory, Didcot, United Kingdom
- ⁿ Also at Department of Physics, St. Petersburg State Polytechnical University, St. Petersburg, Russia
- ^o Also at Louisiana Tech University, Ruston LA, United States of America
- ^p Also at Institutio Catalana de Recerca i Estudis Avancats, ICREA, Barcelona, Spain
- ^q Also at Department of Physics, The University of Michigan, Ann Arbor MI, United States of America
- ^r Also at Graduate School of Science, Osaka University, Osaka, Japan
- ^s Also at Department of Physics, National Tsing Hua University, Taiwan
- ^t Also at Department of Physics, The University of Texas at Austin, Austin TX, United States of America
- ^u Also at Institute of Theoretical Physics, Ilia State University, Tbilisi, Georgia
- ^v Also at CERN, Geneva, Switzerland
- ^w Also at Georgian Technical University (GTU), Tbilisi, Georgia
- ^x Also at O Chadai Academic Production, Ochanomizu University, Tokyo, Japan
- ^y Also at Manhattan College, New York NY, United States of America
- ^z Also at Hellenic Open University, Patras, Greece
- ^{aa} Also at Institute of Physics, Academia Sinica, Taipei, Taiwan
- ^{ab} Also at LAL, Univ. Paris-Sud, CNRS/IN2P3, Université Paris-Saclay, Orsay, France
- ^{ac} Also at Academia Sinica Grid Computing, Institute of Physics, Academia Sinica, Taipei, Taiwan
- ^{ad} Also at School of Physics, Shandong University, Shandong, China
- ^{ae} Also at Moscow Institute of Physics and Technology State University, Dolgoprudny, Russia
- ^{af} Also at Section de Physique, Université de Genève, Geneva, Switzerland
- ^{ag} Also at International School for Advanced Studies (SISSA), Trieste, Italy
- ^{ah} Also at Department of Physics and Astronomy, University of South Carolina, Columbia SC, United States of America
- ^{ai} Also at School of Physics and Engineering, Sun Yat-sen University, Guangzhou, China
- ^{aj} Also at Institute for Nuclear Research and Nuclear Energy (INRNE) of the Bulgarian Academy of Sciences, Sofia, Bulgaria
- ^{ak} Also at Faculty of Physics, M.V.Lomonosov Moscow State University, Moscow, Russia
- ^{al} Associated at Durham University, IPPP, Durham, United Kingdom, United Kingdom

am Also at National Research Nuclear University MEPhI, Moscow, Russia

an Also at Department of Physics, Stanford University, Stanford CA, United States of America

ao Also at Institute for Particle and Nuclear Physics, Wigner Research Centre for Physics, Budapest, Hungary

ap Also at Flensburg University of Applied Sciences, Flensburg, Germany

aq Also at University of Malaya, Department of Physics, Kuala Lumpur, Malaysia

* Deceased